3-9-2018 2:10 PM

Analysis of Subchondral Bone and Microvessels Using a Novel Vascular Perfusion Contrast Agent and Optimized Dual-Energy Computed Tomography

Justin J. Tse
The University of Western Ontario

Supervisor
Holdsworth, David W
The University of Western Ontario

Graduate Program in Medical Biophysics
A thesis submitted in partial fulfillment of the requirements for the degree in Doctor of Philosophy

Abstract

Osteoarthritis (OA), is a chronic debilitating disease that affects millions of individuals and is characterized by the degeneration of joint subchondral bone and cartilage. These tissue degenerations manifest as joint pain, limited range of joint motion, and overall diminished quality of life. Currently, the exact mechanism(s) and cause(s) by which OA initiates and progresses remain unknown. The multi-factorial complex nature of OA (*i.e.* age, diabetes, obesity, and prior injuries have all been shown to play a role in OA) contributes to the current lack of a cure or effective long-term treatment for OA.

One re-emerging and interesting hypothesis revolves around the delicate homeostatic microvascular environment around the cartilage – an avascular tissue. The absence of blood vessels within cartilage stresses the importance of nutrient and oxygen delivery from the neighbouring synovium and subchondral bone. Currently, the effects of changes in the subchondral bone microvessel density on cartilage health remain unknown due to the difficulties in simultaneously studying dense bone and the associated small microvessels.

Computed tomography (CT) is widely used in the diagnosis of OA, as the use of x-rays provide detailed images of the bone degeneration associated with OA. However, the study of microvessels using CT has been exceptionally difficult due to their small (< 10 μm) size, lack of contrast from neighbouring soft tissues, and proximity to dense bone. The purpose of this thesis was to develop a novel dual-energy micro-computed tomography (DECT) compatible vascular perfusion contrast agent and the associated instrumentation to optimize DECT on pre-clinical, cone-beam micro-CT scanners. The combination of these two techniques would facilitate the simultaneous visualization and quantification of subchondral bone and microvessels within the bone underlining the cartilage (*i.e*. distal femoral epiphysis and proximal tibial epiphysis) of rats that have undergone an OA-induced surgery. Results gained from this study will further provide information into the role that microvessels may play in OA.

Keywords

Dual-energy, micro-computed tomography, osteoarthritis, vasculature, bone, erbium, contrast agent, rat hindlimb, x-ray filtration, anterior cruciate ligament transection, partial meniscectomy

Co-Authorship Statement

The following thesis contains three manuscripts ranging from accepted, submitted, and in preparation for scientific journals. Chapter 2 is an original research article entitled “Erbium-based perfusion contrast agent for small-animal microvessel imaging” and published within the *Development and Application of Nanoparticles in Biomedical Imaging*, a special issue of *Contrast Media and Molecular Imaging*, in November 2017. This manuscript was co-authored by Justin J. Tse, Joy Dunmore-Buyze, Maria Drangova, and David W. Holdsworth. In my role as a PhD candidate, I was responsible for the experimental design, sample preparation, micro-CT scanning and reconstruction, statistical and data analysis, data interpretation, and finally manuscript preparation. Joy Dunmore-Buyze aided in data acquisition and input during manuscript preparation. Maria Drangova contributed to data analysis and editorial input. David W. Holdsworth, as the principal investigator and supervisor, was responsible for the project’s conception, provided guidance on the experimental design, and contributed editorial input.

Chapter 3 is an original research article entitled “A method for the production of customized epoxy resin x-ray filters for use within the bore of gantry-based micro-CT scanners” and has been submitted to *The Journal of Medical Imaging* in December 2017 and is currently under revision. This manuscript was co-authored by Justin J. Tse, Joy Dunmore-Buyze, Maria Drangova, and David W. Holdsworth. In my role as a PhD candidate, I was responsible for the experimental design, fabrication of customized x-ray filters, contrast agent preparation, perfusion of rat hindlimbs, micro-CT scanning and reconstruction, statistical and data analysis, data interpretation, and finally manuscript preparation. Joy Dunmore-Buyze aided in the perfusion procedures, data acquisition and input during manuscript preparation. Maria Drangova contributed to data analysis and editorial input. David W. Holdsworth, as the principal investigator and supervisor, was responsible for the project’s conception, provided guidance on the experimental design, and contributed editorial input.

Chapter 4 is an original research article entitled “Studying femoral- and tibial-subchondral bone and microvessel changes using dual-energy micro-computed tomography in a surgically-induced rat hindlimb model of osteoarthritis” and is in preparation for submission

to *Osteoarthritis and Cartilage* in 2018. This manuscript was co-authored by Justin J. Tse, Vasek Pitelka, Joy Dunmore-Buyze, Maria Drangova, and David W. Holdsworth. In my role as a PhD candidate, I was responsible for the experimental design, administration of antibiotics and analgesics post-surgery, contrast agent preparation, perfusion of rat hindlimbs, micro-CT scanning and reconstruction, statistical and data analysis, data interpretation, and finally manuscript preparation. Vasek Pitelka was responsible for performing all sham and OA rat surgeries, aiding in the perfusion of all rat hindlimbs, and preparation of rat hindlimbs for micro-CT analysis. Joy Dunmore-Buyze aided in dual-energy micro-CT data acquisition and input during manuscript preparation. Maria Drangova contributed to data analysis and editorial input. David W. Holdsworth, as the principal investigator and supervisor, was responsible for the project's conception, provided guidance on the experimental design, and contributed editorial input.

Acknowledgments

I would like to first start off by thanking and acknowledging my supervisor Dr. David W. Holdsworth. In addition to the boundless insight and knowledge he has provided throughout my PhD, his patience and teachings have been greatly appreciated in developing myself as a researcher with better project management, problem solving, and communication skills. I would also like to acknowledge my advisory committee (Drs. Maria Drangova and Frank Beier) for always being available to discuss current projects and future directions.

Members of the Holdsworth group have provided endless support, insight, supportive criticisms, and fostered a fantastic working environment. I would like to specifically acknowledge the technicians, Chris Norley, Hristo Nikolov, Steve Pollmann, and Jaques Milner, who have always made themselves available to answer every question and tackle any challenge brought forward. Special thanks must also be given to Joy Dunmore-Buyze and Vasek Pitelka for their availability to always discuss ideas, constant critiquing, and being a joy to work. I must also thank all the students (Matthew Lowerison, Jake Bedore, Mike Pest, and Charmainne Cruje) and principal investigators (Drs. James Lacefield, Frank Beier, Cheryle Séguin, and Maria Drangova) I have met and collaborated with over the tenure of my PhD.

I would like to acknowledge all the financial support that I received over the duration of my PhD candidacy. Financial support has been provided by The University of Western Ontario (Schulich Graduate Scholarship), Ontario Graduate Scholarship, Joint Motion Program, Natural Sciences and Engineering Research Council of Canada, and Alexander Graham Bell Canada Graduate Scholarship.

Finally, and most importantly, I would like to thank my family and friends for all their support and encouragement over my PhD. Especially my wife (Vi), parents (Eileen and John Sr.), and brothers (Timothy and John Jr.) for their continual drive and support during all the challenging times.

Table of Contents

List of Tables

List of Figures

List of Appendices

List of Abbreviations

2D	two-dimensional
3D	three-dimensional
ACLX	anterior cruciate ligament transection
CT	computed tomography
DECT	dual-energy computed tomography
Er	erbium
Er_2O_3	erbium oxide
HU	Hounsfield unit
keV	kilo-electron volt
kVp	kilo-electron volt potential
Micro-CT	micro-computed tomography
MIP	maximum intensity projection
mm	millimeter
OA	osteoarthritis
PMM	partial medial mucosectomy
ROI	region-of-interest
µm	micrometer or micron
VOI	volume-of-interest

Chapter 1

1 INTRODUCTION

1.1 The Importance of Microvessels

The health and maintenance of the humans' body vascular supply is essential for the well-being of every single tissue and organ. The vast blood vessel network, specifically the microvessels (*i.e.* capillaries, < 10 μm) are responsible for the transportation of oxygen, nutrients, and inflammatory molecules to tissues, as well as the removal of CO_2 and waste products.[1,2] Thus, adverse changes to the vascular supply (*i.e.* reduced blood flow or increased inflammatory response) may affect local tissues before cascading into larger and more detrimental effects on the body.

Alterations to the blood circulatory system have been linked to a variety of diseases: diabetes,[3] avascular necrosis,[4] cancer,[5-7] osteoporosis,[8-10] and osteoarthritis.[11,12] Among these diseases, osteoarthritis – a chronic degenerative joint disease that affects both the growing and aging populations – is noteworthy. Despite the connection between microvessels and osteoarthritis, the administration of anti-angiogenic[13] or possible angiogenic drugs[14] has yielded limited success. Presently, with no available cure and limited treatment success, the concern among the affected populations is ever-increasing.

It is apparent that knowledge gaps surrounding the mechanisms by which changes in the vascular supply may promote the development of osteoarthritis remain. Thus, research into the role and mechanism(s) which microvessels play in the initiation and progression of osteoarthritis may provide new insight and identify targets for treatments and preventative measures.

1.2 Osteoarthritis

Osteoarthritis (OA) is a chronic debilitating joint disease and is the most common form of arthritis (*i.e.* rheumatoid, osteoarthritis, psoriatic, *etc*).[16-19] Osteoarthritis affects millions of individuals;[20-23] in Canada alone, ~ 10% over the age of 15 are affected[24] and by 2030, it is projected that a total of 25% (~9 million) of the Canadian population will have OA.[25] Clinically, OA is diagnosed through the examination of x-ray images for the presence of cartilage loss, joint space narrowing, bone degeneration and spurs on x-ray images (Figure 1.1).[26-29] This joint disease commonly affects the hand, hip, knee, back, and neck.[20,24,26,30,31] Symptomatically, OA manifests as painful and stiff joints, which limit mobility and prevent the ability to perform simple tasks (*i.e.* sit-to-stand motion, fine motor skills to hold utensils, *etc*.), resulting in an overall decrease in quality of life for patients.[32]

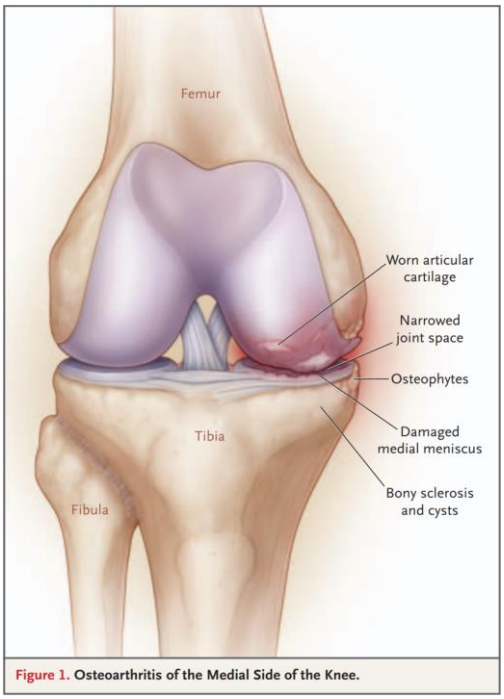

Figure 1.1: Overview of the physiological effects of osteoarthritis on the knee joint. The right side (medial) side of the figure demonstrates the bone and cartilage degeneration associated with OA, while the left (lateral) side demonstrates a healthy knee joint. Reproduced with permission from Felson *et al.*, 2006.[15] Copyright Massachusetts Medical Society.

In addition to the physical burdens imposed by OA, the costs associated with its management are extremely high. In Canada, the health care costs of OA are projected to increase from $2.9 billion to $7.6 billion by 2031.[33] The largest contributions (> 40%) to health care costs are hospital inpatient costs, elective surgeries, and revision joint replacement surgeries (Figure 1.2).[34] The total cost of OA management is further increased with the addition of work loss costs;[35] in Canada, these costs alone exceed $17.5 billion.[33,35]

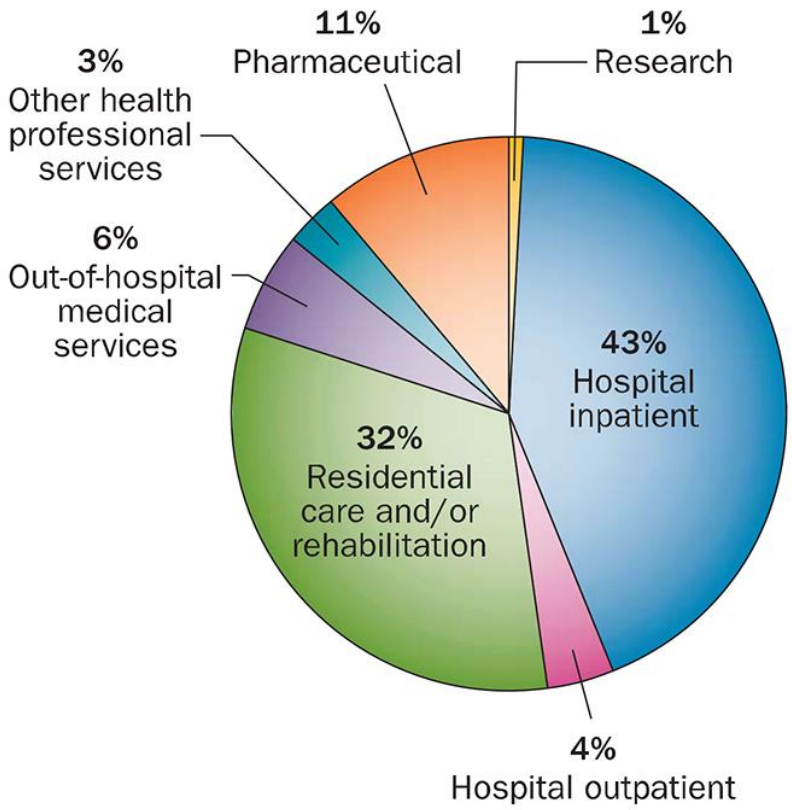

Figure 1.2: Pie chart demonstrating the relative cost breakdown for individuals affected with OA. Reproduced with permission from Hunter *et al.*, 2014.[34] Copyright Springer Nature.

The extensive physical and economic burden imposed by OA has provided the motivation for research into developing treatments for OA. Unfortunately, there does not yet exist an effective disease modifying osteoarthritis drug (DMOAD) that can reverse the cartilage and bone degeneration caused by OA, with current prescribed medications

alleviating only the OA-associated pain.[36,37] At the moment, total joint replacements (TJRs) are presented as the only effective long-term solution to OA.[38,39] However, these metal and plastic implants eventually fail due to poor bone integration, implant loosening, wear, and stress shielding.[33 40,41] Thus, TJRs are not a permanent solution and require a replacement every 15 – 20 years.[42-45] Replacing an implant requires revision surgeries, which can increase the risk of complications (*i.e.* infections) and subsequently, costs to the healthcare system and patient. The absence of a permanent solution to treat and reverse the course of OA emphasizes the need for further research into understanding the cause(s) and mechanism(s) of OA. Information garnered from these studies may result in a better understanding of OA and lead to improvements of current methodologies, or alternative targets for DMOADs, treatments, and preventative measures.

1.2.1 Microvascular Environment of Joints

In humans, the exact cause(s) by which OA is initiated remains unknown. However, research has shown that individuals may be more susceptible to developing OA depending on pre-existing injuries,[46-48] age,[49,50] gender,[50,51] obesity,[50,52,53] genetic pre-disposition,[54,55] or diabetes.[53,56,57] The wide variety of OA-associated factors (as listed above) emphasizes the multifactorial nature of OA and the difficulty in formulating an effective strategy for OA's treatment and prevention.

A re-emerging hypothesis on the initiation of OA revolves around the microvascular supply of the joint;[12,58] where the previously mentioned factors may share a common association through changes in vessel architectures and densities. The role of microvessels in OA has been demonstrated through their ability to invade avascular cartilage and release inflammatory factors that facilitate the degeneration and calcification of cartilage.[59]

The microvessel hypothesis speculates that changes to the delicate homeostatic nature of the microvessels results in subchondral bone changes that facilitate the vascular invasion into cartilage (Figure 1.3, right).[12,60] Responsible for nutrients, inflammatory response, and waste removal (Figure 1.3, left), the microvascular environment is important for the healthy maintenance of the joint. However, disturbances to the microvessel architecture

and density may weaken the joint.[12,61-65] It is not yet known whether the subchondral bone changes, cartilaginous vascular invasion, and eventual OA are the result of a decrease or increase in vascular density. Note that throughout this thesis, subchondral bone will refer to the region of trabecular and cortical bone between physis and the articular cartilage.

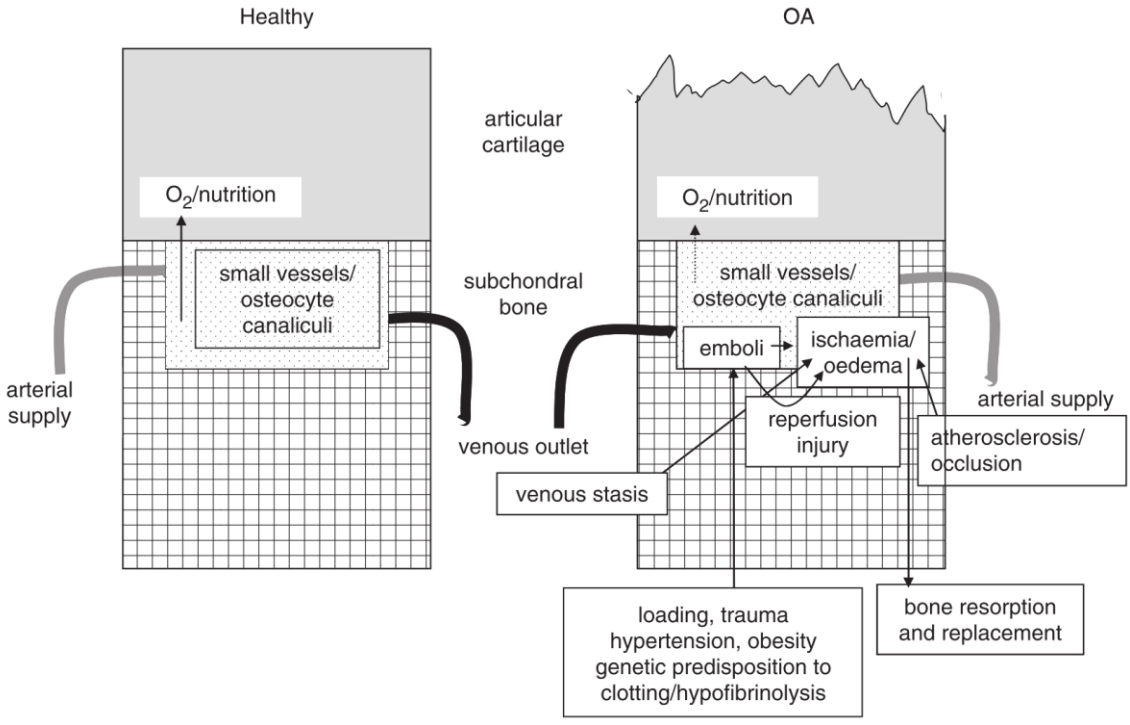

Figure 1.3: Diagram depicting healthy (left) and OA (right) subchondral bone and cartilage. This figured shows the effect that vasculature and subchondral bone may have in the initiation and progression of OA, leading to the degeneration of bone and cartilage observed with OA. Reproduced with permission from Findlay *et al.*[12] Copyright Oxford University Press.

Decreases in blood vessel density may lead to a diminished oxygen and nutrient flow to the joint in conjunction with reduced waste removal.[12,66-69] Combined these effects may lead to the cartilage and bone degeneration observed within OA-affected joints. Alternatively, an increase in vasculature may result in subchondral bone remodeling and microvessel invasion into the cartilage. The subsequent release of inflammatory molecules within the cartilage (normally an avascular tissue) triggers its self-

degradation.[70-73] With the renewed interest in vasculature becoming a target for OA treatments, differentiating between increases and decreases of vascular density is required for the proper administration of vessel suppressing or promoting drugs, respectively. Therefore, studying the subtle vascular density changes within an animal model of OA is crucial to understand the role of microvessels during the initiation and progression of OA.

1.2.2 Animal Models of Osteoarthritis

Animal research has been crucial in the study of how previously mentioned factors (*i.e.* pre-existing injuries, age, obesity, *etc*.) play a role in OA.[74-78] Results of animal studies have led to the successful management of OA-induced symptoms within specific animal models. Unfortunately, translation of treatments (derived from animal studies) to humans has not shown the same level of success.[79-84] The lack of an effective treatment may be attributed to multiple factors: differences in the manifestation of OA between animals and humans,[85] genetic differences,[86] differential joint loading,[87] and possible yet-to-be discovered factors. Regardless, animal models of OA are required to expand our knowledge regarding the human pathogenesis of OA.

Induction of OA within animals can be achieved through naturally occurring,[88,89] surgically-,[74,90,91] or drug-induced models.[77,92,93] While no current animal model perfectly mimics the etiology of OA found in humans, each animal OA model reflects specific portions of OA's pathogenesis within humans.[94]

The anterior cruciate ligament transection (ACLX) and partial media meniscectomy (PMM) surgically-induced animal model of OA[95,96] is of interest. Within rats, the combination of ACLX + PMM results in subchondral bone changes that closely resemble the subchondral bone changes observed within early onset OA in humans.[95] Therefore, studying changes to the microvessel densities during the initiation and progression of this surgically-induced animal model of OA may reveal whether an initial increase or decrease in vascular density precedes or results from the observed subchondral bone changes.

1.2.2.1 Difficulties in Studying the Micro-Vasculature

Unfortunately, the visualization, characterization, and quantification of microvessels of the joint is difficult due to multiple factors: (1) microvessels can be as small as 5-10 μm (*i.e.* capillaries); (2) lack of inherent vascular contrast; and (3) their proximity to dense tissues such as bone. Combined, these three challenges have proven difficult for any single imaging technique.

The ideal imaging technique would be non-destructive (allowing for further sample characterizations *via* other methodologies) and it would provide routine 3D visualization, characterization and quantification of the microvascular environment and associated skeletal structures in response to the surgical induction of OA (ACLX + PMM surgeries). Information gained from such an imaging technique would provide insight into the role of the microvasculature within subchondral bone during the initiation and progression of OA.

1.3 Imaging Modalities for Micro-Vasculature and Bone Analysis

Histology and light microscopy are considered the gold standard imaging techniques.[5,97] Using a multitude of microscopic magnifications and stains, histology allows for the visualization, characterization, and quantification of microvasculature.[98,99] However, the histological examination of bone is difficult due to bone's highly compact mineralized nature, which inhibits the blade from uniformly cutting through the sample. Thus, samples containing bone are typically demineralized or decalcified prior to histologically sectioning and staining. Due to the inherently destructive histological process, obtaining 3D representations of an entire sample requires laborious scanning and reconstruction of serial sections.[100-102] This process limits the applicability of histology with studies that require high throughput (*i.e.* large numbers of specimens) or large samples (*i.e.* whole limbs). However, pre-clinical imaging techniques such as micro-magnetic resonance imaging, contrast-enhanced ultrasound, and micro-computed tomography can provide images that would allow the visualization, characterization, and quantification of microvessels and bone within *in vitro* and *ex vivo* intact specimens.

Micro-magnetic resonance imaging (micro-MRI) is a non-destructive imaging technique that can facilitate the visualization and characterization of microvessels and bones with the use of various pulse sequences and contrast enhancements.[103-105] Perfusion with exogenous vascular contrast agents [106,107] allows for the detection of the contrast enhanced vessels against the un-enhanced surrounding soft tissue. Micro-MRI possesses the resolution necessary to detect in-plane microvessels (*i.e.* capillaries, < 10 μm).[108] However, the image signal-to-noise (SNR) in combination with non-isotropic voxels, hinders the accurate detection and characterization of microvessels within the large slice thicknesses.[109]

Ultrasound (US) is a common and relatively inexpensive imaging technique, in comparison to micro-MRI and micro-computed tomography.[110] The use of contrast-enhanced ultrasound (CEUS) is commonly employed to detect microvessels. Separately, CEUS detects contrast-enhanced vessels facilitated with a bolus injection of microbubble backscatters,[5] and US can detect fractures along the bone surfaces.[111,112] However, the imaging of vessels within bones has proven challenging due to internal reflections of the backscattered signal. Lower frequency and increased power transducers can penetrate deeper into tissues and provide the internal visualization of bone; however, these imaging systems have reduced resolution[113] and increased heat tissue deposition.[114,115] In addition to the reduction in resolution and increased possibility of sample degradation (through increased heat deposition), the typical contrast-to-noise ratio (CNR) within CEUS images is rather poor, especially at resolutions necessary to distinguish between microvessels and subchondral bone.

Micro-computed tomography (micro-CT, Figure 1.4) is a ubiquitous imaging technique routinely used for the visualization and characterization of bone[95,116-118] and vessels (*i.e.* angiography).[119,120] Micro-CT is commonly used in the analysis and visualization of dense x-ray attenuating objects, such as bone. However, visualization and detection of the low x-ray attenuating vessels require the addition of an exogenous vascular contrast agent (similar to micro-MRI and CEUS).[121]

Figure 1.4: Micro-CT scanner located at Robarts Research Institute.

In comparison to CEUS, the noise within micro-CT images is reduced and on par with those acquired with micro-MRI. Therefore, with an already well-established ability to characterize and visualize bone and vessels, micro-CT is the ideal imaging methodology for the *in vitro* and *ex vivo* study of changes to the subchondral bone and its associated vascular networks during the initiation and progression of OA.

1.4 Micro-Computed Tomography Analysis of Micro-Vasculature and Bone

Micro-CT acquisition involves the projection of x-rays through a sample, where a detector records the x-ray attenuation (*i.e.* x-ray absorption) along each ray path. Signal intensity within micro-CT images is dependent on the electron density of the sample. The generation of a micro-CT image involves the acquisition of hundreds of two-dimensional (2D) projections at many view angles around the object of interest. Three-dimensional (3D) image reconstruction is then carried out using established algorithms (such as filtered back-projection, implemented in cone-beam geometry).[122] Within the 3D volume, each volumetric element (*i.e.* voxel) is assigned a CT number proportional to the linear attenuation coefficient – of the material within that voxel.[123]

In practice, micro-CT is commonly used for the examination of objects with natural endogenous contrast, resulting in easier visualization within CT images[124]– such as bones,[125-128] verification of medical apparatuses,[129,130] geological and material analysis.[131-135] However, as previously mentioned, visualizing materials with low-electron densities (*i.e.* soft tissues) is difficult and requires contrast enhancement *via* exogenous agents.[136]

1.4.1 Contrast Enhancement

Visualization of materials with low x-ray contrast difference relative to their surroundings (*e.g.* blood vessels within tissue) requires the addition of an exogenous contrast agent.[137,138] Clinically, an iodine-based vascular contrast agent is injected into the blood stream to enhance the x-ray attenuation of perfused vessels (*i.e.* angiography). Thus, the contrast-enhanced vessels can be easily visualized and automatically segmented (based on greyscale values) from surrounding non-contrast enhanced soft tissues. Due to insufficient spatial resolution and partial volume effects, perfused contrast-enhanced vessels are indistinguishable and masked when present near and within dense x-ray attenuating bone. Thus, iodine-based agents are unable to facilitate the distinction and automatic separation of perfused vessels from nearby bone, when based on greyscale values alone (Figure 1.5).[139]

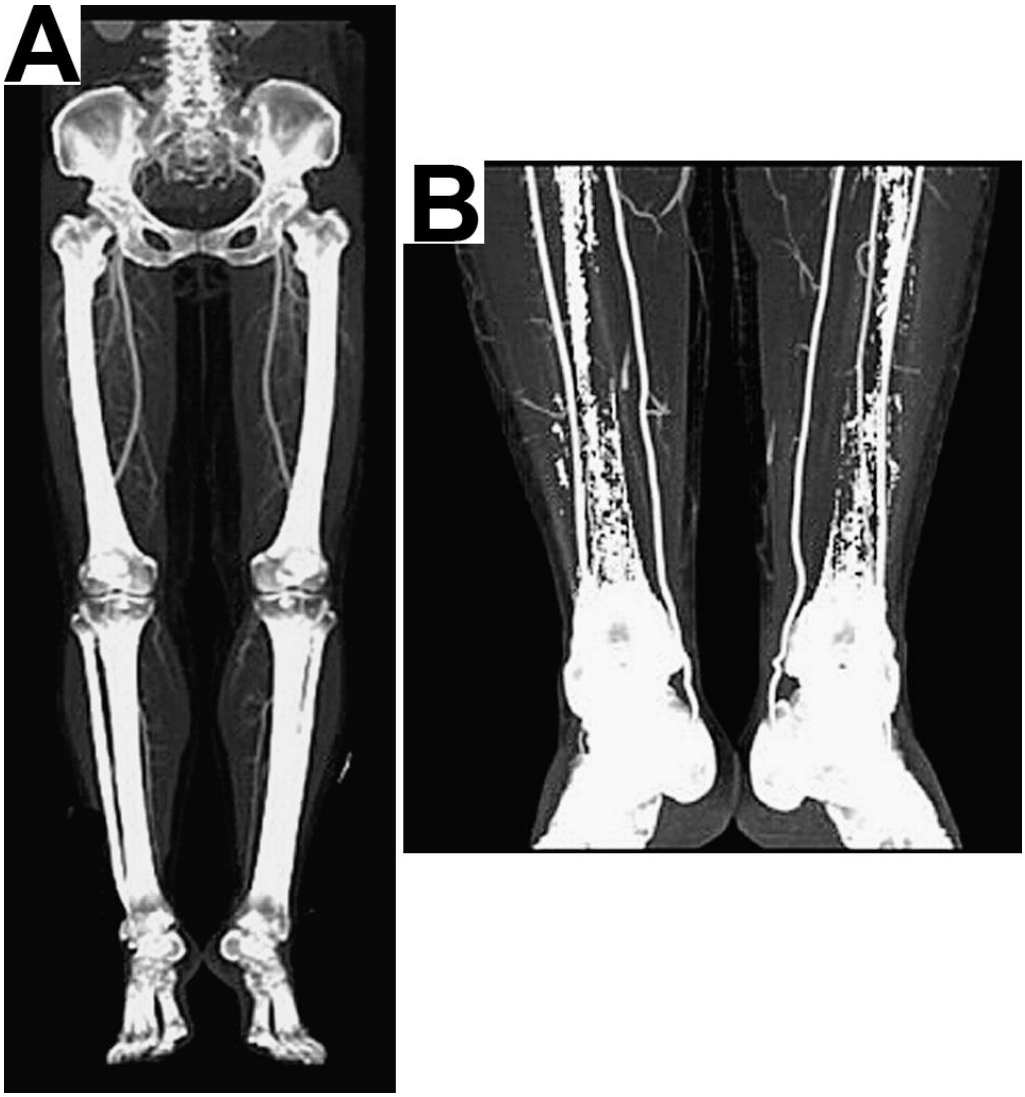

Figure 1.5: Images depicting the typical results of a CT angiogram of the legs of a patient**.** Iodine vascular contrast enhancement of perfused vasculature (*i.e.* femoral artery) is easily distinguished from surrounding soft tissue. However, as one can imagine, distinguishing perfused vasculature surrounding dense skeletal structure (*i.e.* femur, tibia, and ankle) based on greyscale values is extremely difficult. Modified with permission from Yamamoto *et al.*, 2009.[140] Copyright Elsevier.

Pre-clinically, higher-electron density barium (Ba)- and lead (Pb)-based contrast agents provide significantly higher x-ray attenuation than the iodine-based counterpart.[141] However, the contrast enhancement, provided by Ba and Pb, exhibits similar greyscale

values as cortical bone,[142] hindering the automated separation of the perfused vascular network within and around bone.

To overcome this challenge, the sample can be scanned with micro-CT before the addition of the contrast agent (*i.e.* bone-only image) and following perfusion of the contrast agent and decalcification of bone (*i.e.* vessel-only image).[143,144] Combining the two resulting scans would provide a visualization of the interaction between the perfused vessels and bone. However, the main disadvantage of this methodology is the susceptibility to improper image co-registration between the acquired scans, caused by movement of vessels and tissues during perfusion and decalcification processes. The resulting misalignments between the vascular network and bone may lead to misinterpretations regarding the anatomical relationship between vessels and bone.

Fortunately, there does exist a micro-CT imaging technique that can non-destructively and simultaneously acquire segmented volumes of soft tissue, bone and perfused vessels: dual-energy micro-computed tomography.

1.4.2 Dual-Energy Micro-Computed Tomography (DECT)

Dual-energy micro-CT (DECT) is an imaging technique that can separate components within a sample, based on their elemental composition. As the name infers, DECT involves scanning specimens at two x-ray energies, followed by the application of decomposition algorithms that exploit differences between the elemental specific x-ray attenuation signatures of each component. With this approach, visually distinct and quantifiable 3D volumes of each component can be obtained.[142] The performance of DECT and image decomposition can be further improved by tailoring the DECT-acquisition parameters to the specific absorption K-edge of the material of interest.

When sufficient x-ray energy is present to exceed an elements' unique absorption K-edge energy (*i.e.* the x-ray energy required to eject an inner K-shell electron), a significant increase in x-ray attenuation is observed. Image decomposition of the material-of-interest can be significantly improved by tailoring and narrowing the low- and high-energy (*i.e.* dual-energy) x-ray spectra around the element-specific distinctive x-ray attenuation spike.

Synchrotron radiation-based DECT (SRDECT) presents itself as an ideal DECT imaging technique due to its ability to provide monochromatic x-ray energies.[145,146] Synchrotron facilities can provide x-rays of a single energy with high photon flux, resulting in increased signal-to-noise, reduced noise, and a reduction in scan times.[147] Additionally, the sub-micron resolution[148] can allow the resolution of smaller structures, and recent developments detectors have allowed for larger field-of-views.[149] While appealing, the main drawbacks associated with SRDECT are: (1) limited number of synchrotron facilities; (2) cost associated with travelling to these facilities; (3) competition for beamtime; and (4) synchronization of biological experiments with available beamtime.

The use of pre-clinical micro-CT scanners for DECT analysis is a more practical approach due to the wider availability of scanners (in comparison to synchrotrons) and their current use in DECT research.[150-152] However, optimizing the performance of DECT on pre-clinical, gantry-based, cone-beam, micro-CT scanners has been challenging due to: (1) lower x-ray tube potentials (90 kVp) which may limit the performance of DECT on contrast agents of high-Z (*i.e.* Pb); (2) limited accessibility to micro-CT scanner internal hardware to apply the necessary x-ray filtration to shape output x-ray spectra; and (3) inherent gantry movements and non-reproducible bed micro-movements, which may result in image misalignment.

Recent developments outlined throughout this thesis will demonstrate the methodologies and techniques implemented to optimally perform DECT on a pre-clinical, gantry-based, cone-beam, micro-CT scanner. We explain how to tailor the output x-ray spectrum of a pre-clinical micro-CT scanner for a customizable novel *ex vivo* vascular perfusion contrast agent. The combination of our contrast agent and DECT was then applied to study the micro-vascular and subchondral bone differences within the hindlimbs of a well-characterized surgically induced rat model of OA over the course of 8-weeks post-operatively.

1.5 Thesis Objectives and Hypotheses

In this thesis, we present the methodologies required to: (1) develop a novel pre-clinical, DECT-compatible, *ex vivo* Er-based microvascular (*i.e.* capillaries of < 10 μm) perfusion

contrast agent; (2) implementation of DECT on pre-clinical, gantry-based, micro-CT scanners with a lower peak tube potential of 90 kVp; and (3) the combination of the above techniques to study the concurrent microvascular and subchondral bone changes that may occur during the initiation and progression of OA in a well-characterized surgically induced rat hindlimb model of OA (*i.e.* ACLX + PMM). The ultimate results of each Chapter are summarized as follows.

In Chapter 2, we describe and characterize a novel DECT-compatible erbium (Er)-based *ex vivo* vascular perfusion contrast agent. Ultrasonic cavitation was employed to create a colloidal suspension of nanoparticle-sized aggregates of erbium oxide (Er_2O_3) suspended within a two-part silicone elastomer carrier. Intact mice were perfused post-mortem with our Er-based suspension to evaluate its efficacy as a vascular perfusion contrast agent. Micro-CT scans (50 μm isotropic voxel spacing) of Er-perfused mice confirmed a significantly higher contrast enhancement of vessels when compared with nearby dense bone and with a commercially available Pb-based contrast agent. High-resolution micro-CT scans (5 μm isotropic voxel spacing) of well-characterized mouse kidney vasculature verified the ability of the novel vascular contrast agent to perfuse the smallest vessels (*i.e.* capillaries, < 10 μm).

In Chapter 3, we outline the methodology required to customize and optimize DECT for our novel Er-based contrast agent (Chapter 2) in a way that is compatible with the large installed base of pre-clinical gantry-based cone-beam micro-CT scanners with a 90 kVp operating x-ray tube potential. This chapter outlines the required aspects for the optimum performance of DECT: (1) choosing and fabricating appropriate x-ray filtration and acquisition protocols to match Er's absorption K-edge; (2) fabrication of an automated filter-exchange mechanism for the automated acquisition of DECT images; and (3) accurate sub-voxel image co-registration using fiducial markers. The optimized DECT was demonstrated through the automated decomposition of several Er-perfused rat hindlimbs into distinct and quantifiable 3D volumes of soft tissue, bone, and vessel.

In Chapter 4, the combination of our novel Er-based contrast agent (Chapter 2) and optimized DECT (Chapter 3) was utilized to simultaneously study the subchondral bone

and microvessel changes during the initiation and progression of OA within a well-characterized surgically-induced rat hindlimb model of OA (*i.e.* ACLX + PMM). Rats (N = 56) were split into two surgery groups (ACLX + PMM or sham surgery) and for various time points (T = 0, 1, 2, 4, and 8 weeks) post-surgery. Quantitative analysis of vessel and bone changes was confined to the distal femoral epiphysis and proximal tibial epiphysis regions, due to their proximity to the cartilaginous surface and ease of contouring regions of interest within the CT data.

In Chapter 5, we present a summary of the main goals and findings from Chapters 2 – 4. Additionally, we review future directions and research that may benefit from the work presented within this thesis.

1.6 References

1. J. R. Levick, *An Introduction to Cardiovascular Physiology*. (Elsevier Science, 2013).

2. P. Carmeliet, Angiogenesis in health and disease. *Nature Medicine* **9**, 653-660 (2003).

3. R. Cheng, J.-x. Ma, Angiogenesis in Diabetes and Obesity. *Reviews in Endocrine & Metabolic Disorders* **16**, 67-75 (2015).

4. P. Lafforgue, Pathophysiology and natural history of avascular necrosis of bone. *Joint Bone Spine* **73**, 500-507 (2006).

5. M. R. Lowerison, J. J. Tse, M. N. Hague, A. F. Chambers, D. W. Holdsworth, J. C. Lacefield, Compound speckle model detects anti-angiogenic tumor response in preclinical nonlinear contrast-enhanced ultrasonography. *Medical Physics* **44**, 99-111 (2017).

6. P. M. Hoff, K. K. Machado, Role of angiogenesis in the pathogenesis of cancer. *Cancer Treatment Reviews* **38**, 825-833 (2012).

7. N. Nishida, H. Yano, T. Nishida, T. Kamura, M. Kojiro, Angiogenesis in Cancer. *Vascular Health and Risk Management* **2**, 213-219 (2006).

8. J. I. Barzilay, P. Bůžková, H. A. Fink, J. A. Cauley, J. A. Robbins, P. S. Garimella, D. I. Jalal, K. J. Mukamal, Systemic markers of microvascular disease and bone mineral density in older adults. *Osteoporosis International* **27**, 3217-3225 (2016).

9. V. V. Shanbhogue, S. Hansen, M. Frost, K. Brixen, A. P. Hermann, Bone disease in diabetes: another manifestation of microvascular disease? *The Lancet Diabetes & Endocrinology* **5**, 827-838 (2017).

10. K. Alagiakrishnan, A. Juby, D. Hanley, W. Tymchak, A. Sclater, Role of vascular factors in osteoporosis. *J Gerontol A Biol Sci Med Sci* **58**, 362-366 (2003).

11. J. Filipowska, K. A. Tomaszewski, Ł. Niedźwiedzki, J. A. Walocha, T. Niedźwiedzki, The role of vasculature in bone development, regeneration and proper systemic functioning. *Angiogenesis* **20**, 291-302 (2017).

12. D. M. Findlay, Vascular pathology and osteoarthritis. *Rheumatology (Oxford)* **46**, 1763-1768 (2007).

13. J. L. Hamilton, M. Nagao, B. R. Levine, D. Chen, B. R. Olsen, H.-J. Im, Targeting VEGF and its Receptors for the Treatment of Osteoarthritis and Associated Pain. *J Bone Miner Res* **31**, 911-924 (2016).

14. S. M. Chim, J. Tickner, S. T. Chow, V. Kuek, B. Guo, G. Zhang, V. Rosen, W. Erber, J. Xu, Angiogenic factors in bone local environment. *Cytokine Growth Factor Rev* **24**, 297-310 (2013).

15. D. T. Felson Osteoarthritis of the Knee. *New England Journal of Medicine* **354**, 841-848 (2006).

16. J. Y. Reginster, The prevalence and burden of arthritis. *Rheumatology (Oxford)* **41**, 3-6 (2002).

17. M. C. Corti, C. Rigon, Epidemiology of osteoarthritis: prevalence, risk factors and functional impact. *Aging clinical and experimental research* **15**, 359-363 (2003).

18. J. M. Hootman, C. G. Helmick, T. J. Brady, A Public Health Approach to Addressing Arthritis in Older Adults: The Most Common Cause of Disability. *American Journal of Public Health* **102**, 426-433 (2012).

19. A. Mobasheri, M. Batt, An update on the pathophysiology of osteoarthritis. *Ann Phys Rehabil Med* **59**, 333-339 (2016).

20. A. Litwic, M. Edwards, E. Dennison, C. Cooper, Epidemiology and Burden of Osteoarthritis. *British Medical Bulletin* **105**, 185-199 (2013).

21. T. Neogi, The Epidemiology and Impact of Pain in Osteoarthritis. *Osteoarthritis Cartilage* **21**, 1145-1153 (2013).

22. J. H. Salmon, A. C. Rat, J. Sellam, M. Michel, J. P. Eschard, F. Guillemin, D. Jolly, B. Fautrel, Economic impact of lower-limb osteoarthritis worldwide: a systematic review of cost-of-illness studies. *Osteoarthritis and Cartilage* **24**, 1500-1508 (2016).

23. F. C. Breedveld, Osteoarthritis--the impact of a serious disease. *Rheumatology (Oxford)* **43 Suppl 1**, i4-8 (2004).

24. K. V. MacDonald, C. Sanmartin, K. Langlois, D. A. Marshall, Symptom onset, diagnosis and management of osteoarthritis. *Health Rep* **25**, 10-17 (2014).

25. G. H. C. Bombardier, D. Mosher, The Impact of Arthritis in Canada:Today and Over the Next 30 Years. 2011.

26. K. Sinusas, Osteoarthritis: diagnosis and treatment. *Am Fam Physician* **85**, 49-56 (2012).

27. H. J. Braun, G. E. Gold, Diagnosis of osteoarthritis: Imaging. *Bone* **51**, 278-288 (2012).

28. C. Y. J. Wenham, A. J. Grainger, P. G. Conaghan, The role of imaging modalities in the diagnosis, differential diagnosis and clinical assessment of peripheral joint osteoarthritis. *Osteoarthritis and Cartilage* **22**, 1692-1702 (2014).

29. M. Boesen, K. Ellegaard, M. Henriksen, H. Gudbergsen, P. Hansen, H. Bliddal, E. M. Bartels, R. G. Riis, Osteoarthritis year in review 2016: imaging. *Osteoarthritis and Cartilage* **25**, 216-226 (2017).

30. P. C. Birchfield, Osteoarthritis overview. *Geriatric Nursing* **22**, 124-131 (2001).

31. P. A. Dieppe, L. S. Lohmander, Pathogenesis and management of pain in osteoarthritis. *The Lancet* **365**, 965-973 (2005).

32. U. L. F. Jakobsson, I. R. Hallberg, Pain and quality of life among older people with rheumatoid arthritis and/or osteoarthritis: a literature review. *Journal of Clinical Nursing* **11**, 430-443 (2002).

33. B. Sharif, J. Kopec, N. Bansback, M. M. Rahman, W. M. Flanagan, H. Wong, P. Fines, A. Anis, Projecting the direct cost burden of osteoarthritis in Canada using a microsimulation model. *Osteoarthritis and Cartilage* **23**, 1654-1663 (2015).

34. D. J. Hunter, D. Schofield, E. Callander, The individual and socioeconomic impact of osteoarthritis. *Nat Rev Rheumatol* **10**, 437-441 (2014).

35. B. Sharif, R. Garner, D. Hennessy, C. Sanmartin, W. M. Flanagan, D. A. Marshall, Productivity costs of work loss associated with osteoarthritis in Canada from 2010 to 2031. *Osteoarthritis and Cartilage* **25**, 249-258 (2017).

36. P. Qvist, A. C. Bay-Jensen, C. Christiansen, E. B. Dam, P. Pastoureau, M. A. Karsdal, The disease modifying osteoarthritis drug (DMOAD): Is it in the horizon? *Pharmacol Res* **58**, 1-7 (2008).

37. M. A. Karsdal, M. Michaelis, C. Ladel, A. S. Siebuhr, A. R. Bihlet, J. R. Andersen, H. Guehring, C. Christiansen, A. C. Bay-Jensen, V. B. Kraus, Disease-modifying treatments for osteoarthritis (DMOADs) of the knee and hip: lessons learned from failures and opportunities for the future. *Osteoarthritis and Cartilage* **24**, 2013-2021 (2016).

38. R. S. Aujla, C. N. Esler, Total Knee Arthroplasty for Osteoarthritis in Patients Less Than Fifty-Five Years of Age: A Systematic Review. *The Journal of Arthroplasty*.

39. S. T. Skou, E. M. Roos, M. B. Laursen, M. S. Rathleff, L. Arendt-Nielsen, S. Rasmussen, O. H. Simonsen, Two year outcome from two parallel randomized trials on total knee replacement and non-surgical treatment of knee osteoarthritis. *Osteoarthritis and Cartilage* **25**, S35-S36.

40. P. F. Sharkey, P. M. Lichstein, C. Shen, A. T. Tokarski, J. Parvizi, Why are total knee arthroplasties failing today--has anything changed after 10 years? *J Arthroplasty* **29**, 1774-1778 (2014).

41. A. V. Lombardi Jr, K. R. Berend, J. B. Adams, Why knee replacements fail in 2013. *patient, surgeon, or implant?* **96-B**, 101-104 (2014).

42. P. Sabouret, F. Lavoie, J. M. Cloutier, Total knee replacement with retention of both cruciate ligaments: a 22-year follow-up study. *Bone Joint J* **95-b**, 917-922 (2013).

43. J. A. Rodriguez, H. Bhende, C. S. Ranawat, Total condylar knee replacement: a 20-year followup study. *Clinical Orthopaedics and Related Research®*, 10-17 (2001).

44. J. J. Callaghan, C. T. Martin, Y. Gao, A. J. Pugely, S. S. Liu, D. D. Goetz, S. S. Kelley, R. C. Johnston, What Can Be Learned From Minimum 20-year Followup Studies of Knee Arthroplasty? *Clinical Orthopaedics and Related Research* **473**, 94-100 (2015).

45. J. J. Callaghan, M. W. Beckert, D. W. Hennessy, D. D. Goetz, S. S. Kelley, Durability of a cruciate-retaining TKA with modular tibial trays at 20 years. *Clinical Orthopaedics and Related Research®* **471**, 109-117 (2013).

46. J. A. Buckwalter, Articular Cartilage Injuries. *Clinical Orthopaedics and Related Research* **402**, 21-37 (2002).

47. J. T. Badlani, C. Borrero, S. Golla, C. D. Harner, J. J. Irrgang, The effects of meniscus injury on the development of knee osteoarthritis: data from the osteoarthritis initiative. *Am J Sports Med* **41**, 1238-1244 (2013).

48. E. M. Roos, Joint injury causes knee osteoarthritis in young adults. *Curr Opin Rheumatol* **17**, 195-200 (2005).

49. A. S. Anderson, R. F. Loeser, Why is Osteoarthritis an Age-Related Disease? *Best Pract Res Clin Rheumatol* **24**, 15 (2010).

50. M. Blagojevic, C. Jinks, A. Jeffery, K. P. Jordan, Risk factors for onset of osteoarthritis of the knee in older adults: a systematic review and meta-analysis. *Osteoarthritis Cartilage* **18**, 24-33 (2010).

51. R. Birtwhistle, R. Morkem, G. Peat, T. Williamson, M. E. Green, S. Khan, K. P. Jordan, Prevalence and management of osteoarthritis in primary care: an epidemiologic cohort study from the Canadian Primary Care Sentinel Surveillance Network. *CMAJ Open* **3**, E270-E275 (2015).

52. R. M. Aspden, Obesity punches above its weight in osteoarthritis. *Nat Rev Rheumatol* **7**, 65-68 (2011).

53. R. Pandey, N. Kumar, S. Paroha, R. Prasad, M. Yadav, S. Jain, H. Yadav, Impact of obesity and diabetes on arthritis: An update. *Health* **5**, 14 (2013).

54. T. D. Spector, F. Cicuttini, J. Baker, J. Loughlin, D. Hart, Genetic influences on osteoarthritis in women: a twin study. *Bmj* **312**, 940-943 (1996).

55. T. D. Spector, A. J. MacGregor, Risk factors for osteoarthritis: genetics. *Osteoarthritis Cartilage* **12, Supplement**, (2004).

56. G. Schett, A. Kleyer, C. Perricone, E. Sahinbegovic, A. Iagnocco, J. Zwerina, R. Lorenzini, F. Aschenbrenner, F. Berenbaum, M. A. D'Agostino, J. Willeit, S. Kiechl, Diabetes is an independent predictor for severe osteoarthritis: results from a longitudinal cohort study. *Diabetes Care* **36**, 403-409 (2013).

57. M. M. Rahman, J. A. Kopec, J. Cibere, C. H. Goldsmith, A. H. Anis, The relationship between osteoarthritis and cardiovascular disease in a population health survey: a cross-sectional study. *BMJ Open* **3**, (2013).

58. G. Li, J. Yin, J. Gao, T. S. Cheng, N. J. Pavlos, C. Zhang, M. H. Zheng, Subchondral bone in osteoarthritis: insight into risk factors and microstructural changes. *Arthritis Res Ther* **15**, 223 (2013).

59. R. J. Lories, F. P. Luyten, The bone-cartilage unit in osteoarthritis. *Nat Rev Rheumatol* **7**, 43-49 (2011).

60. D. M. Findlay, Subchondral bone in osteoarthritis.

61. D. A. Walsh, C. S. Bonnet, E. L. Turner, D. Wilson, M. Situ, D. F. McWilliams, Angiogenesis in the synovium and at the osteochondral junction in osteoarthritis. *Osteoarthritis and Cartilage* **15**, 743-751 (2007).

62. S. Ashraf, D. A. Walsh, Angiogenesis in osteoarthritis. *Curr Opin Rheumatol* **20**, 573-580 (2008).

63. C. S. Bonnet, D. A. Walsh, Osteoarthritis, angiogenesis and inflammation. *Rheumatology (Oxford)* **44**, 7-16 (2005).

64. L. Haywood, D. F. McWilliams, C. I. Pearson, S. E. Gill, A. Ganesan, D. Wilson, D. A. Walsh, Inflammation and angiogenesis in osteoarthritis. *Arthritis Rheum* **48**, (2003).

65. M. Marenzana, T. R. Arnett, The Key Role of the Blood Supply to Bone. *Bone Research* **1**, 203-215 (2013).

66. F. Feihl, L. Liaudet, B. Waeber, B. I. Levy, Hypertension: a disease of the microcirculation? *Hypertension* **48**, 1012-1017 (2006).

67. H. Sasaki, K. Takayama, T. Matsushita, K. Ishida, S. Kubo, T. Matsumoto, N. Fujita, S. Oka, M. Kurosaka, R. Kuroda, Autophagy modulates osteoarthritis-related gene expression in human chondrocytes. *Arthritis & Rheumatism* **64**, 1920-1928 (2012).

68. S. Le Clanche, D. Bonnefont-Rousselot, E. Sari-Ali, F. Rannou, D. Borderie, Inter-relations between osteoarthritis and metabolic syndrome: A common link? *Biochimie* **121**, 238-252 (2016).

69. R. Chadha, Revealed aspect of metabolic osteoarthritis. *Journal of Orthopaedics* **13**, 347-351 (2016).

70. S. Suri, S. E. Gill, S. Massena de Camin, D. Wilson, D. F. McWilliams, D. A. Walsh, Neurovascular invasion at the osteochondral junction and in osteophytes in osteoarthritis. *Ann Rheum Dis* **66**, 1423-1428 (2007).

71. M. Pickarski, T. Hayami, Y. Zhuo, L. T. Duong, Molecular changes in articular cartilage and subchondral bone in the rat anterior cruciate ligament transection and meniscectomized models of osteoarthritis. *BMC Musculoskelet Disord* **12**, 197 (2011).

72. T. Hayami, M. Pickarski, Y. Zhuo, G. A. Wesolowski, G. A. Rodan, l. T. Duong, Characterization of articular cartilage and subchondral bone changes in the rat anterior cruciate ligament transection and meniscectomized models of osteoarthritis. *Bone* **38**, (2006).

73. X. L. Yuan, H. Y. Meng, Y. C. Wang, J. Peng, Q. Y. Guo, A. Y. Wang, S. B. Lu, Bone–cartilage interface crosstalk in osteoarthritis: potential pathways and future therapeutic strategies. *Osteoarthritis and Cartilage* **22**, 1077-1089 (2014).

74. P. I. Mapp, P. S. Avery, D. F. McWilliams, J. Bowyer, C. Day, S. Moores, R. Webster, D. A. Walsh, Angiogenesis in two animal models of osteoarthritis. *Osteoarthritis Cartilage* **16**, (2008).

75. A. M. Malfait, C. B. Little, J. J. McDougall, A commentary on modelling osteoarthritis pain in small animals. *Osteoarthritis and Cartilage* **21**, 1316-1326 (2013).

76. A.-M. Malfait, C. B. Little, On the predictive utility of animal models of osteoarthritis. *Arthritis Res Ther* **17**, 225 (2015).

77. E. L. Kuyinu, G. Narayanan, L. S. Nair, C. T. Laurencin, Animal models of osteoarthritis: classification, update, and measurement of outcomes. *Journal of Orthopaedic Surgery and Research* **11**, 19 (2016).

78. E. Teeple, G. D. Jay, K. A. Elsaid, B. C. Fleming, Animal Models of Osteoarthritis: Challenges of Model Selection and Analysis. *The AAPS Journal* **15**, 438-446 (2013).

79. S. H. Chang, T. Yasui, S. Taketomi, T. Matsumoto, J. R. Kim-Kaneyama, T. Omiya, Y. Hosaka, H. Inui, Y. Omata, R. Yamagami, D. Mori, F. Yano, U. Chung, S. Tanaka, T. Saito, Comparison of mouse and human ankles and establishment of mouse ankle osteoarthritis models by surgically-induced instability. *Osteoarthritis and Cartilage* **24**, 688-697 (2016).

80. P. M. van der Kraan, Factors that influence outcome in experimental osteoarthritis. *Osteoarthritis and Cartilage* **25**, 369-375 (2017).

81. K. O. W. Chan, G. Y. F. Ng, A review on the effects of glucosamine for knee osteoarthritis based on human and animal studies. *Hong Kong Physiotherapy Journal* **29**, 42-52 (2011).

82. A. Chevrier, M. Nelea, M. B. Hurtig, C. D. Hoemann, M. D. Buschmann, Meniscus structure in human, sheep, and rabbit for animal models of meniscus repair. *Journal of Orthopaedic Research* **27**, 1197-1203 (2009).

83. C. B. Little, D. J. Hunter, Post-traumatic osteoarthritis: from mouse models to clinical trials. *Nat Rev Rheumatol* **9**, 485-497 (2013).

84. L. G. Ameye, M. F. Young, Animal models of osteoarthritis: lessons learned while seeking the "Holy Grail". *Curr Opin Rheumatol* **18**, 537-547 (2006).

85. H. B. van der Worp, D. W. Howells, E. S. Sena, M. J. Porritt, S. Rewell, V. O'Collins, M. R. Macleod, Can Animal Models of Disease Reliably Inform Human Studies? *PLoS Medicine* **7**, e1000245 (2010).

86. J. Seok, H. S. Warren, A. G. Cuenca, M. N. Mindrinos, H. V. Baker, W. Xu, D. R. Richards, G. P. McDonald-Smith, H. Gao, L. Hennessy, C. C. Finnerty, C. M. López, S. Honari, E. E. Moore, J. P. Minei, J. Cuschieri, P. E. Bankey, J. L. Johnson, J. Sperry, A. B. Nathens, T. R. Billiar, M. A. West, M. G. Jeschke, M. B. Klein, R. L. Gamelli, N. S. Gibran, B. H. Brownstein, C. Miller-Graziano, S. E. Calvano, P. H. Mason, J. P. Cobb, L. G. Rahme, S. F. Lowry, R. V. Maier, L.

L. Moldawer, D. N. Herndon, R. W. Davis, W. Xiao, R. G. Tompkins, I. the, L. S. C. R. P. Host Response to Injury, A. Abouhamze, U. G. J. Balis, D. G. Camp, A. K. De, B. G. Harbrecht, D. L. Hayden, A. Kaushal, G. E. O'Keefe, K. T. Kotz, W. Qian, D. A. Schoenfeld, M. B. Shapiro, G. M. Silver, R. D. Smith, J. D. Storey, R. Tibshirani, M. Toner, J. Wilhelmy, B. Wispelwey, W. H. Wong, Genomic responses in mouse models poorly mimic human inflammatory diseases. *Proc Natl Acad Sci U S A* **110**, 3507-3512 (2013).

87. A. M. Bendele, Animal models of osteoarthritis. *J Musculoskelet Neuronal Interact* **1**, (2001).

88. A. M. Bendele, J. F. Hulman, Spontaneous cartilage degeneration in guinea pigs. *Arthritis & Rheumatism* **31**, 561-565 (1988).

89. M. Schünke, B. Tillmann, M. Brück, W. Müller-Ruchholtz, Morphologic characteristics of developing osteoarthrotic lesions in the knee cartilage of str/in mice. *Arthritis & Rheumatism* **31**, 898-905 (1988).

90. C. T. Appleton, D. D. McErlain, J. L. Henry, D. W. Holdsworth, F. Beier, Molecular and histological analysis of a new rat model of experimental knee osteoarthritis. *Ann N Y Acad Sci* **1117**, 165-174 (2007).

91. D. L. Batiste, A. Kirkley, S. Laverty, L. M. F. Thain, A. R. Spouge, D. W. Holdsworth, Ex vivo characterization of articular cartilage and bone lesions in a rabbit ACL transection model of osteoarthritis using MRI and micro-CT. *Osteoarthritis Cartilage* **12**, (2004).

92. C. Guingamp, P. Gegout-Pottie, L. Philippe, B. Terlain, P. Netter, P. Gillet, Mono-iodoacetate-induced experimental osteoarthritis. A dose-response study of loss of mobility, morphology, and biochemistry. *Arthritis & Rheumatism* **40**, 1670-1679 (1997).

93. S. Miyamoto, J. Nakamura, S. Ohtori, S. Orita, T. Omae, T. Nakajima, T. Suzuki, K. Takahashi, Intra-articular injection of mono-iodoacetate induces osteoarthritis of the hip in rats. *BMC Musculoskelet Disord* **17**, 132 (2016).

94. H. Fang, F. Beier, Mouse models of osteoarthritis: modelling risk factors and assessing outcomes. *Nat Rev Rheumatol* **10**, 413-421 (2014).

95. D. D. McErlain, C. T. Appleton, R. B. Litchfield, V. Pitelka, J. L. Henry, S. M. Bernier, F. Beier, D. W. Holdsworth, Study of subchondral bone adaptations in a rodent surgical model of OA using in vivo micro-computed tomography. *Osteoarthritis Cartilage* **16**, 458-469 (2008).

96. C. T. Appleton, D. D. McErlain, J. L. Henry, D. W. Holdsworth, F. Beier, Molecular and histological analysis of a new rat model of experimental knee osteoarthritis. *Ann N Y Acad Sci* **1117**, (2007).

97. C. Schürmann, F. Gremse, H. Jo, F. Kiessling, R. P. Brandes, Micro-CT Technique Is Well Suited for Documentation of Remodeling Processes in Murine Carotid Arteries. *PLoS One* **10**, e0130374 (2015).

98. B. Roche, V. David, A. Vanden-Bossche, F. Peyrin, L. Malaval, L. Vico, M.-H. Lafage-Proust, Structure and quantification of microvascularisation within mouse long bones: What and how should we measure? *Bone* **50**, 390-399 (2012).

99. D. A. Binks, E. M. Gravallese, D. Bergin, R. J. Hodgson, A. L. Tan, M. M. Matzelle, D. McGonagle, A. Radjenovic, Role of vascular channels as a novel mechanism for subchondral bone damage at cruciate ligament entheses in osteoarthritis and inflammatory arthritis. *Annals of the Rheumatic Diseases* **74**, 196-203 (2015).

100. Y. Xu, J. G. Pickering, Z. Nong, E. Gibson, J.-M. Arpino, H. Yin, A. D. Ward, A Method for 3D Histopathology Reconstruction Supporting Mouse Microvasculature Analysis. *PLoS One* **10**, e0126817 (2015).

101. J. Dauguet, T. Delzescaux, F. Condé, J.-F. Mangin, N. Ayache, P. Hantraye, V. Frouin, Three-dimensional reconstruction of stained histological slices and 3D non-linear registration with in-vivo MRI for whole baboon brain. *Journal of Neuroscience Methods* **164**, 191-204 (2007).

102. M. E. Vandenberghe, A. S. Herard, N. Souedet, E. Sadouni, M. D. Santin, D. Briet, D. Carre, J. Schulz, P. Hantraye, P. E. Chabrier, T. Rooney, T. Debeir, V. Blanchard, L. Pradier, M. Dhenain, T. Delzescaux, High-throughput 3D whole-brain quantitative histopathology in rodents. *Sci Rep* **6**, 20958 (2016).

103. K. Chiba, M. Uetani, Y. Kido, M. Ito, N. Okazaki, K. Taguchi, H. Shindo, Osteoporotic changes of subchondral bone in osteoarthritis of the knee: a 3-T MRI study. *Osteoporosis International* **23**, 589-597 (2012).

104. J. A. Hipp, A. Jansujwicz, C. A. Simmons, B. D. Snyder, Trabecular bone morphology from micro-magnetic resonance imaging. *Journal of Bone and Mineral Research* **11**, 286-292 (1996).

105. J. L. Tremoleda, M. Khalil, L. L. Gompels, M. Wylezinska-Arridge, T. Vincent, W. Gsell, Imaging technologies for preclinical models of bone and joint disorders. *EJNMMI Research* **1**, 11-11 (2011).

106. J. P. Dyke, M. Synan, P. Ezell, D. Ballon, J. Racine, R. K. Aaron, Characterization of bone perfusion by dynamic contrast-enhanced magnetic resonance imaging and positron emission tomography in the Dunkin–Hartley guinea pig model of advanced osteoarthritis. *Journal of Orthopaedic Research* **33**, 366-372 (2015).

107. J.-F. Budzik, G. Lefebvre, H. Behal, S. Verclytte, P. Hardouin, P. Teixeira, A. Cotten, Bone marrow perfusion measured with dynamic contrast enhanced

magnetic resonance imaging is correlated to body mass index in adults. *Bone* **99**, 47-52 (2017).

108. G. A. Johnson, H. Benveniste, R. D. Black, L. W. Hedlund, R. R. Maronpot, B. R. Smith, Histology by magnetic resonance microscopy. *Magn Reson Q* **9**, 1-30 (1993).

109. A. P. Pathak, E. Kim, J. Zhang, M. V. Jones, Three-Dimensional Imaging of the Mouse Neurovasculature with Magnetic Resonance Microscopy. *PLoS One* **6**, e22643 (2011).

110. I. Sudoł-Szopińska, C. Schueller-Weidekamm, A. Plagou, J. Teh, Ultrasound in Arthritis. *Radiologic Clinics of North America*.

111. R. E. Friedrich, M. Heiland, S. Bartel-Friedrich, Potentials of ultrasound in the diagnosis of midfacial fractures. *Clinical Oral Investigations* **7**, 226-229 (2003).

112. T. H. Marshburn, E. Legome, A. Sargsyan, S. M. Li, V. A. Noble, S. A. Dulchavsky, C. Sims, D. Robinson, Goal-directed ultrasound in the detection of long-bone fractures. *J Trauma* **57**, 329-332 (2004).

113. A. Ng, J. Swanevelder, Resolution in ultrasound imaging. *Continuing Education in Anaesthesia Critical Care & Pain* **11**, 186-192 (2011).

114. G. ter Haar, in *Interventional Oncology: A Practical Guide for the Interventional Radiologist*, P. Mueller, A. Adam, Eds. (Springer New York, New York, NY, 2012), pp. 51-63.

115. G. M. Hahn, P. Kernahan, A. Martinez, D. Pounds, S. Prionas, T. Anderson, G. Justice, Some Heat Transfer Problems Associated with Heating By Ultrasound, Microwaves, or Radio Frequency. *Ann N Y Acad Sci* **335**, 327-346 (1980).

116. D. L. Batiste, A. Kirkley, S. Laverty, L. M. Thain, A. R. Spouge, D. W. Holdsworth, Ex vivo characterization of articular cartilage and bone lesions in a rabbit ACL transection model of osteoarthritis using MRI and micro-CT. *Osteoarthritis Cartilage* **12**, (2004).

117. D. W. Holdsworth, M. M. Thornton, Micro-CT in small animal and specimen imaging. *Trends in Biotechnology* **20**, S34-S39 (2002).

118. U. U. Joseph, V. S. Arthur, W. Ian, P. Vasek, A. G. Harvey, T. M. Underhill, W. H. David, In vivo micro-CT analysis of bone remodeling in a rat calvarial defect model. *Physics in Medicine & Biology* **54**, 2147 (2009).

119. P. Blery, P. Pilet, A. V. Bossche, A. Thery, J. Guicheux, Y. Amouriq, F. Espitalier, N. Mathieu, P. Weiss, Vascular imaging with contrast agent in hard and soft tissues using microcomputed-tomography. *Journal of Microscopy* **262**, 40-49 (2016).

120. D. Sarhaddi, B. Poushanchi, M. Merati, C. Tchanque-Fossuo, A. Donneys, J. Baker, S. R. Buchman, Validation of Histologic Bone Analysis Following Microfil Vessel Perfusion. *Journal of histotechnology* **35**, 180-183 (2012).

121. A. Lahooti, S. Sarkar, S. Laurent, S. Shanehsazzadeh, Dual nano-sized contrast agents in PET/MRI: a systematic review. *Contrast Media & Molecular Imaging* **11**, 428-447 (2016).

122. L. A. Feldkamp, L. C. Davis, J. W. Kress, Practical cone-beam algorithm. *Journal of the Optical Society of America A* **1**, 612-619 (1984).

123. C. T. Badea, M. Drangova, D. W. Holdsworth, G. A. Johnson, In Vivo Small Animal Imaging using Micro-CT and Digital Subtraction Angiography. *Physics in medicine and biology* **53**, R319-R350 (2008).

124. J. T. Bushberg, *The Essential Physics of Medical Imaging*. (Lippincott Williams & Wilkins, 2002).

125. A. K. Willi, X-ray computed tomography. *Physics in Medicine & Biology* **51**, R29 (2006).

126. S. M. Botter, G. J. van Osch, J. H. Waarsing, J. S. Day, J. A. Verhaar, H. A. Pols, J. P. van Leeuwen, H. Weinans, Quantification of subchondral bone changes in a murine osteoarthritis model using micro-CT. *Biorheology* **43**, 379-388 (2006).

127. M. Ding, C. C. Danielsen, I. Hvid, S. Overgaard, Three-dimensional microarchitecture of adolescent cancellous bone. *Bone* **51**, 953-960 (2012).

128. R. E. Guldberg, R. T. Ballock, B. D. Boyan, C. L. Duvall, A. S. P. Lin, S. Nagaraja, M. Oest, J. Phillips, B. D. Porter, G. Robertson, W. R. Taylor, Analyzing bone, blood vessels, and biomaterials with microcomputed tomography. *Engineering in Medicine and Biology Magazine, IEEE* **22**, 77-83 (2003).

129. F. Hindelang, R. Zurbach, Y. Roggo, Micro Computer Tomography for medical device and pharmaceutical packaging analysis. *Journal of Pharmaceutical and Biomedical Analysis* **108**, 38-48 (2015).

130. R. J. Morrison, K. N. Kashlan, C. L. Flanangan, J. K. Wright, G. E. Green, S. J. Hollister, K. J. Weatherwax, Regulatory Considerations in the Design and Manufacturing of Implantable 3D-Printed Medical Devices. *Clinical and Translational Science* **8**, 594-600 (2015).

131. A. K. Agrawal, P. S. Sarkar, B. Singh, Y. S. Kashyap, P. T. Rao, A. Sinha, Application of X-ray micro-CT for micro-structural characterization of APCVD deposited SiC coatings on graphite conduit. *Applied Radiation and Isotopes* **108**, 133-142 (2016).

132. A. Maurício, M. F. Pereira, C. Rocha, C. Figueiredo, J. M. Marques, X-ray Micro-CT Study of Cabeço de Vide Serpentinites and Carbonate Rock Samples: A Preliminary Approach. *Procedia Earth and Planetary Science* **17**, 952-955 (2017).

133. E. I. Jussiani, P. J. dos Reis, C. R. Appoloni, Determining chemical composition of materials through micro-CT images. *Micron* **89**, 9-15 (2016).

134. S. Tomioka, T. Kozaki, H. Takamatsu, N. Noda, S. Nisiyama, N. Kozai, S. Suzuki, S. Sato, Analysis of microstructural images of dry and water-saturated compacted bentonite samples observed with X-ray micro CT. *Applied Clay Science* **47**, 65-71 (2010).

135. F. Cosmi, A. Bernasconi, Micro-CT investigation on fatigue damage evolution in short fibre reinforced polymers. *Composites Science and Technology* **79**, 70-76 (2013).

136. J. Lancaster, B. Hasegawa, *Fundamental Mathematics and Physics of Medical Imaging*. (CRC Press, 2016).

137. L. Faggioni, E. Neri, P. Sbragia, R. Pascale, L. D'Errico, D. Caramella, C. Bartolozzi, 80-kV Pulmonary CT Angiography With 40 mL of Iodinated Contrast Material in Lean Patients: Comparison of Vascular Enhancement With Iodixanol (320 mg I/mL)and Iomeprol (400 mg I/mL). *American Journal of Roentgenology* **199**, 1220-1225 (2012).

138. D. Andreini, S. Mushtaq, E. Conte, C. Segurini, M. Guglielmo, M. Petullà, V. Volpato, A. Annoni, A. Baggiano, A. Formenti, A. L. Bartorelli, C. Fiorentini, M. Pepi, Coronary CT angiography with 80 kV tube voltage and low iodine concentration contrast agent in patients with low body weight. *Journal of Cardiovascular Computed Tomography* **10**, 322-326 (2016).

139. M. M. Lell, K. Anders, M. Uder, E. Klotz, H. Ditt, F. Vega-Higuera, T. Boskamp, W. A. Bautz, B. F. Tomandl, New Techniques in CT Angiography. *RadioGraphics* **26**, S45-S62 (2006).

140. S. Yamamoto, J. McWilliams, C. Arellano, W. Marfori, W. Cheng, T. McNamara, W. J. Quinones-Baldrich, S. G. Ruehm, Dual-energy CT angiography of pelvic and lower extremity arteries: dual-energy bone subtraction versus manual bone subtraction. *Clinical Radiology* **64**, 1088-1096 (2009).

141. H. Lusic, M. W. Grinstaff, X-Ray Computed Tomography Contrast Agents. *Chemical reviews* **113**, 10.1021/cr200358s (2013).

142. P. V. Granton, S. I. Pollmann, N. L. Ford, M. Drangova, D. W. Holdsworth, Implementation of dual- and triple-energy cone-beam micro-CT for postreconstruction material decomposition. *Med Phys* **35**, 5030-5042 (2008).

143. H. Nyangoga, P. Mercier, H. Libouban, M. F. Basle, D. Chappard, Three-dimensional characterization of the vascular bed in bone metastasis of the rat by microcomputed tomography (MicroCT). *PLoS One* **6**, e17336 (2011).

144. S. Sutter, A. Todorov, T. Ismail, A. Haumer, I. Fulco, G. Schulz, A. Scherberich, A. Kaempfen, I. Martin, D. J. Schaefer, Contrast-Enhanced Microtomographic Characterisation of Vessels in Native Bone and Engineered Vascularised Grafts Using Ink-Gelatin Perfusion and Phosphotungstic Acid. *Contrast Media & Molecular Imaging* **2017**, 10 (2017).

145. T. Masami, T. Takanori, S. Makoto, E. Masahiro, N. Yutaka, O. Yumiko, K. Toshiyuki, H. Kazuyuki, U. Kentaro, Y. Naoto, Electron density measurement with dual-energy x-ray CT using synchrotron radiation. *Physics in Medicine & Biology* **48**, 673 (2003).

146. D. M. L. Cooper, L. D. Chapman, Y. Carter, Y. Wu, A. Panahifar, H. M. Britz, B. Bewer, W. Zhouping, M. J. M. Duke, M. Doschak, Three dimensional mapping of strontium in bone by dual energy K-edge subtraction imaging. *Physics in Medicine & Biology* **57**, 5777 (2012).

147. Y.-C. Lin, Y. Hwu, G.-S. Huang, M. Hsiao, T.-T. Lee, S.-M. Yang, T.-K. Lee, N.-Y. Chen, S.-S. Yang, A. Chen, S.-M. Ka, Differential synchrotron X-ray imaging markers based on the renal microvasculature for tubulointerstitial lesions and glomerulopathy. *Scientific Reports* **7**, 3488 (2017).

148. D. P. Clark, C. T. Badea, Micro-CT of rodents: State-of-the-art and future perspectives. *Physica Medica* **30**, 619-634 (2014).

149. K. Umetani, Y. Kawata, N. Niki, in *SPIE/COS Photonics Asia*. (SPIE, 2016), vol. 10020, pp. 9.

150. I. Danad, B. Ó Hartaigh, J. K. Min, Dual-energy computed tomography for detection of coronary artery disease. *Expert review of cardiovascular therapy* **13**, 1345-1356 (2015).

151. Y. H. Lee, G. G. Song, Diagnostic accuracy of dual-energy computed tomography in patients with gout: A meta-analysis. *Semin Arthritis Rheum*, (2017).

152. R. Salvador, M. P. Luque, A. Ciudin, B. Pano, L. Bunesch, C. Sebastia, C. Nicolau, Usefulness of dual-energy computed tomography with and without dedicated software in identifying uric acid kidney stones. *Radiologia* **58**, 120-128 (2016).

Chapter 2

2 Erbium-Based Perfusion Contrast Agent for Small-Animal Microvessel Imaging

2.1 Introduction

It is increasingly important in pre-clinical research to study the vasculature in both soft tissue and bone.[1-5] This includes visualization, quantification, and characterization of microvessels (*i.e.* vessels less than 10 µm in diameter). Micro-computed tomography (micro-CT) of intact *ex vivo* small animals can provide images with spatial resolution better than 5 µm.[6-8] However, blood-filled vessels lack inherent radiographic contrast, requiring the use of an exogeneous contrast agent that can pass through capillaries and be retained within the vascular system. The increased contrast provided by such an agent facilitates automated (or semi-automated) segmentation (*i.e.* separation) of the perfused vasculature from surrounding tissues.

The performance (sensitivity, specificity, and accuracy) of vessel segmentation algorithms has been shown to be dependent on the contrast-to-noise ratio (CNR, defined as the ratio of the vessel signal to surrounding tissue signal) between the contrast-enhanced vasculature and surrounding tissue in the micro-CT image.[9] Higher CNR results in a more robust and objective classification of the perfused vessels, leading to a more accurate assessment of their microarchitecture. The CNR can be increased by either reducing background noise or increasing the signal intensity within the vessel. However, decreasing micro-CT image noise is typically impractical, as it is achieved through much longer scan times.[10] Therefore, the most effective method to increase vessel CNR is to increase the contrast within the vasculature, using a radiopaque exogeneous contrast agent.

Several formulations of exogeneous vascular contrast agents are commonly available. Most clinical contrast agents for *in vivo* use are iodine-based. However, their small molecular size of < 800 Da, results in rapid clearance (*i.e.* within minutes) *via* the kidneys.[11,12] Even in post-mortem studies with increased iodine concentrations and scan

times, the short retention time of these iodine-based agents make them unsuitable for micro-vessel studies. Pre-clinical exogeneous agents, of larger molecular sizes (*i.e.* > 1100 Da), can remain within the blood pool for hours.[13,14] These contrast agents are typically iodine-, barium-, or lead-based and have been used effectively to study vessel microarchitecture in the heart,[15,16] kidney,[17,18] tumours,[19,20] nerves,[21-23] and long bones.[24,25] However, these pre-clinical contrast agents do not exhibit optimal x-ray absorption (and hence do not optimize CNR) on a large installed base of micro-CT machines that typically operate at a maximum of 90 kilo-electron volts (keV).

X-ray absorption, responsible for observed contrast within x-ray images, is influenced by the K-edge of the contrast material (*i.e.* the energy required to eject an inner K-shell electron). The K-edges for common pre-clinical contrast agents are 33 keV for iodine, 37.4 keV for barium, and 88 keV for lead. These K-edge energies are not optimally matched for typical micro-focus tubes operating at a peak potential of 90 kVp, as the K-edge energies are located either at the low- or high-energy range of the output spectrum of the tube. Ideally, a contrast agent with a K-edge closer to the mean energy of the output spectrum of these micro-CT machines (~42.7 keV) would provide enhanced x-ray absorption.

The lanthanide erbium (Er), with a K-edge at 57.5 keV, would provide the contrast necessary for micro-CT scanners operating at 90 kVp. An Er-based contrast agent would also provide an additional benefit for dual-energy micro-CT studies, which require CT scans above and below the K-edge of the material of interest.[26] In this study, we describe a novel contrast agent based on erbium oxide (Er_2O_3) nanoparticles (nominal diameter of ~50 nm), and illustrate a process by which Er_2O_3 nanoparticles form a colloidal suspension in a continuous-phase fluid (*i.e.* two-part liquid silicone elastomer). This methodology of contrast agent fabrication resulted in a high atomic number (and consequently highly x-ray attenuating) *ex vivo* vascular perfusion contrast agent, with sufficiently low viscosity (19.2 mPa·s) to ensure the perfusion of the micro-vascular network (< 10 µm).

Using single-energy micro-CT, we demonstrate the efficacy of the custom contrast agent in a post-mortem murine model. The contrast agent perfused the smallest vessels in a mouse kidney (*i.e.* glomerular capillary bundles), and provided increased CNR with respect to surrounding tissues, facilitating the visualization of micro-vessels with diameter < 10 μm. The Er-based contrast agent provided a greater CNR than commercially available agents, while also possessing a more appropriate absorption K-edge energy (57.5 keV). The resulting increase in vessel contrast would enhance the performance and automation of segmentation algorithms in all types of vascular networks and small-animal models (for both single- and dual-energy studies). This approach will be applicable in many pre-clinical studies, including musculoskeletal, cardiovascular, neurovascular, and oncological research programs.

2.2 Materials and Methods

2.2.1 Er-based Contrast Agent Preparation

Erbium oxide (Er_2O_3) nanoparticles (NPs) were chosen as the main constituent of the contrast agent, due to their high x-ray attenuation and availability in a nanoparticulate powder (nominal diameter ~ 50 nm). To deliver the Er_2O_3 NPs throughout the vascular network, a commercially available two-part silicone elastomer (commonly used for vascular perfusion, Microfil MV-132, Flowtech Inc., Carver, MA, USA) was chosen as the carrier matrix. Uncured, this silicone elastomer has a manufacturer-reported viscosity of 20 mPa·s and when cured, the silicone matrix entrains the suspended Er_2O_3 NPs to form a stable silicone cast of the perfused vasculature. Initial experiments revealed difficulties incorporating the Er_2O_3 NPs within the two-part silicone elastomer. Analysis, *via* confocal fluorescence microscopy, of the uncoated Er_2O_3 powder revealed the tendency of the NPs to naturally aggregate into clusters > 1 μm, due to van der Waals forces – nanoparticulate powders have been shown to naturally clump and form much larger particle sizes when left uncoated or untreated.[27,28] Large aggregates such as these could clump together and prevent the perfusion of arterioles and capillaries, inhibiting perfusion of the venous system. Thus, to address the fact that uncoated nanoparticles tend to aggregate into large clumps (*i.e.* > 100 μm) a method was devised to ensure the size of the Er_2O_3 NPs in the final product remained smaller than 100 nm, as follows.

2.2.2 Er_2O_3 NP silicone elastomer suspension

Uncoated Er_2O_3 NPs of ~50 nm nominal diameter (Nanostructured and Amorphous Materials, Houston, TX, USA) were ground using a mortar and pestle for ~ 5 minutes to break down large aggregates. The ground powder was then mixed with an additive-free clear two-part silicone elastomer (Microfil MV-132, Carver, MA, USA), which is mixed in a ratio of two parts MV-Diluent to one part MV-132. To prepare 30 mL of contrast agent, 4.0 g of ground Er_2O_3 (*i.e.* 13.3% w/v) was added to 17.47 mL of MV-Diluent and 8.73 mL of MV-132; the remaining 3.8 mL was comprised of the curing agent described below, which was added immediately prior to perfusion into the animal. The uncured suspension of Er_2O_3 powder and silicone elastomer was probe sonicated (Branson Digital Sonifier 450D, standard 13 mm tapped horn, Crystal Electronics, Newmarket, ON, CAN) for a total of 35 minutes with 25% amplitude and a duty cycle of 30 s ON to 10 s OFF. Due to the intense heat generated during sonication, the samples were immersed in an ice bath and sonication was performed in three intervals interspersed with 5 – 10 minute cool-down periods. The Er_2O_3 NP silicone elastomer suspension was prepared several hours prior to perfusion, to allow particle aggregates to settle, then decanted prior to use. If prepared further in advance, sonication of the suspension of 5 - 10 minutes is required to ensure particle re-suspension.

2.2.3 Curing agent

To facilitate consistent and controlled curing of the Er_2O_3 NP silicone elastomer suspension, a tin-based curing agent was prepared in-house. The curing agent comprised a solution of 40% (w/w) dibutyltin dilaurate (Sigma Aldrich, St. Louis, MI, USA) in tetraethyl orthosilicate (Sigma Aldrich, St. Louis, MI, USA), which was mixed using a magnetic stirrer for several hours until it became a homogeneous pale-yellow transparent solution.

2.2.4 Er-based Contrast Agent Characterization

Particle and aggregate sizes of the “raw” and sonicated Er_2O_3 powder were evaluated visually using confocal fluorescence microscopy. Prior to sonication, drops of raw Er_2O_3 powder mixed within the two-part silicone elastomer were dispensed on a glass bottom

microwell dish (MatTek Corporation, Ashland, MA, USA). Following sonication, drops of the prepared Er-based suspension were placed on a separate microwell dish. Samples were analyzed using confocal fluorescence microscopy (Leica DMi8, Wetzlar, Germany), an Ar 488 nm laser for excitation, and emission bandwidths of 493 – 739 nm. To visualize particle sizes within the non-sonicated "raw" sample and sonicated suspension, a 20x (HC PL APO CS2 20x/0.75 DRY) and 63x (HC PL APO CS2 63x/1.40 OIL) objective lens were used, respectively.

Dynamic Light Scattering (DLS) was used to quantify the size distribution of the prepared Er-based suspension. A 10% (v/v) dilution of the suspension in MV-Diluent was prepared and analyzed with DLS (ZetaSizer Nano instrument, Malvern Instruments Ltd, Malvern, UK). Measurements were performed at room temperature (25°C) in a quartz cuvette (1 mg/mL).

The viscosity of the contrast agent was measured using a lab-based Modular Compact Rheometer (MCR 302, Anton Paar, Graz, Austria); the measured viscosity was used to correct the DLS measurements.

2.2.5 Animals

All animal studies were approved by the Animal Use Subcommittee at Western University (protocol #2015-018). Five male C57BL/6 mice (~30 g) were used for this study. The mouse model was selected to demonstrate the capability of the Er_2O_3 contrast agent to perfuse the microvasculature of the smallest of the commonly used small animal models. Anesthetized mice were exsanguinated with sterile saline followed by perfusion with the Er-contrast agent. To prevent blood clot formation during exsanguination, sterile 0.9% (w/v) saline was heparinized to 0.4% (1 mL of heparin (Sandoz, QC, CAN) in 250 mL saline). Sterile tubing (Baxter Canada, Mississauga, ON, CAN), 1.8 m in length, was used to connect the saline bag to a blunted 21G × 3/4" butterfly catheter (BD, Franklin Lakes, NJ, USA). The saline IV bag was hung 127 cm above the surgery table, thereby providing a pressure of 94 mmHg. Five minutes prior to the start of the procedure the mice were given a 100 µl intraperitoneal injection of heparin. After induction of anesthesia (3% isoflurane (Baxter Canada, Mississauga, ON, CAN) in O_2 at a rate of 2

mL/min) an incision was made along the thoracic cavity exposing the heart. The butterfly catheter was carefully inserted into the left ventricle parallel to the septum. A drop of cyanoacrylate (Krazy Glue, Elmer's Products, Atlanta, GA, USA) was applied at the entry point of the catheter into the left ventricle to avoid accidental piercing of the septum. The right atrium was clipped to allow for circulatory system drainage. The heparinized saline solution was perfused throughout the circulatory system for 10 minutes to ensure complete removal of the blood.

During saline perfusion, 3.8 mL (12.7% v/v) of curing agent was added to 36.2 ml Er_2O_3-based silicone elastomer suspension and vortexed (VWR® Fixed Speed Vortex Mixer, Radnor, PA, USA) continuously for 8 minutes. The contrast agent was injected into an empty IV bag (with separate 1.8 m of surgical tubing) and hung 160 cm above the mice (129 mm Hg). While this value is greater than the mean arterial pressure (MAP) of mice (~ 103 mm Hg),[29,30] it was chosen to ensure complete perfusion of the animal before the contrast agent cured. Furthermore, the perfusion pressure used in this study is significantly lower than the >150 mmHg used in prior studies using the lead-based Microfil agent.[22,31-33] Perfusion at a pressure more closely matched to peak systolic pressure (*i.e.* ~120 mmHg) reduces the risk of vascular dilation and capillary rupture. The contrast agent was let to freely perfuse through the animal until completely cured, which occurred approximately ~35 minutes after start of perfusion. Following contrast agent curing, mice were placed in 10% neutral buffered formalin overnight, prior to micro-CT scanning.

2.2.6 Data Collection and Analysis

Whole body mouse scans were acquired with a pre-clinical micro-CT scanner (Vision 120, GE Healthcare, London, ON, CAN). The scan parameters were 90 kVp (no added filtration), 40 mA, 900 views, 0.4º increment angle over 360º, geometric magnification of 1.13, 16 ms exposure, resulting in a total exposure time of 14.4 s and 576 mAs. Including the time required for gantry motion and recording of image projections, the total acquisition time was 5 minutes. The projection images were binned 2 × 2 prior to reconstruction for a final isotropic voxel spacing of 100 μm.

Higher resolution scans of the hindlimb regions were acquired on a specimen scanner (Locus, GE Healthcare, London, ON, CAN) using a 3 hr scan protocol (900 views, 80 kVp, 80 μA, no added filtration, 0.4° increment angle over 360º, geometric magnification of 1.41, 15 frame averaging, and 2 × 2 binning for a final isotropic voxel spacing of 40 μm). To prevent sample motion during these high-resolution image acquisitions, the perfused mouse was placed in a 50 mL tube.

Confirmation of perfusion of micro-vessels (*i.e.* < 10 μm) was achieved by high-resolution single-energy micro-CT. Fabricated micro-vessel constructs, or synthetic capillaries have been utilized to evaluate micro-vessel perfusions in the past,[34,35] but fabricating synthetic vessels with diameters on the order of 10 μm remains technically challenging. Fortunately, the mouse kidney is a well-characterized organ system, with known vessel diameters ranging from the renal artery (~0.3 mm) to capillaries (~10 μm).[36,37] The kidney contains many glomeruli (responsible for the waste removal and blood filtering), which are comprised of capillaries in a bundle of ~75 μm diameter.[38] Therefore, an excised Er_2O_3-perfused kidney was embedded in paraffin in a 1.2 mL tube (Corning®, Corning, NY, USA) and scanned with a specimen scanner (Locus SP, GE Healthcare, London, ON, CAN), using a 16 hr protocol. Scan parameters were 80 kVp, 80 μA, 900 projections, no added filtration, 0.4° increment angle over 360º, geometric magnification of 3.83, 14 frame averaging, and 1 × 1 binning for a final isotropic spatial resolution of 4.8 μm.

The micro-CT scanners used in this study were all equipped with a CsI-based energy-weighted detector. It has been shown that the peak response of these detectors[39] is very close to the absorption K-edge of Er (57.5 keV), making them ideally suited for detection of an Er-based contrast agent.

Each of the scans contained calibrators of water and air, which were used for image calibration and conversion into Hounsfield units (HU). This allowed us to quantify the amount of contrast enhancement of perfused vasculature, based on the CT signal level in HU within various organs throughout the vascular system. Using 3D visualization and analysis software (MicroView, GE Healthcare, London, ON, CAN), regions of interest

(ROI) 500 × 500 × 500 μm were generated in each region and the mean HU values recorded. Specifically, for all mice, the mean HU was determined from the heart (left ventricle), testes, and inferior vena cava (IVC), as they represented the beginning, middle, and end of the perfusion pathway, respectively. The CT signal levels within the selected organs were compared to cortical bone within the diaphysis region (*i.e.* the densest endogenous contrast) and a commercially available lead-based contrast agent. A rat hindlimb previously perfused with the widely used and commercially available lead-based contrast agent (Microfil MV-122, Flowtech Inc, Caver, MA, USA) was scanned using the 100 μm acquisition protocol.

All statistical analyses were performed using Prism 6 (GraphPad Software Inc, La Jolla, CA, USA). Repeated measures ANOVA was used to test for statistical differences between all Er-based contrast-enhanced regions (*i.e.* heart, testes, IVC) and cortical bone. In a separate test, one-way unpaired ANOVA was performed to compare the mean attenuation in Er-perfused vessels against cortical bone and the Microfil MV122-perfused rat femoral artery. Statistical differences were noted if a $p < 0.05$ was achieved.

2.3 Results

2.3.1 Efficacy of an *ex vivo* Er-based contrast agent for vascular perfusion

An effective pre-clinical post-mortem x-ray compatible vascular contrast agent must be comprised of small, x-ray attenuating particles homogeneously suspended within a low-viscosity medium. These characteristics will ensure uniform contrast enhancement of perfused vasculature, including micro-vessels with diameter < 10 μm (*i.e.* capillaries). Automated segmentation algorithms, which are typically based on grey-scale levels, require homogeneous perfusion of micro-vessels to effectively separate perfused vasculature from surrounding tissues, so it is essential to employ an appropriate particle size, uniformly distributed in the carrier medium.

Ultrasonic cavitation (sonication) was used to successfully break up large aggregates of Er_2O_3 to nm-sized aggregates, which could be homogeneously incorporated within the two-part silicone matrix. Following intense sonication, a visually homogeneous suspension of 13.3% w/v Er_2O_3 within the two-part silicone elastomer was achieved. The Er_2O_3 NPs were found to remain in suspension for several days, allowing for the contrast agent to be prepared several days prior to use. Confocal fluorescence microscopy visually confirmed that the size of the sonicated nanoparticles within the Er_2O_3 contrast agent suspension (Figure 2.1B) were less than 100 nm – a size that can pass easily through the micro-vessels of any vascular system.

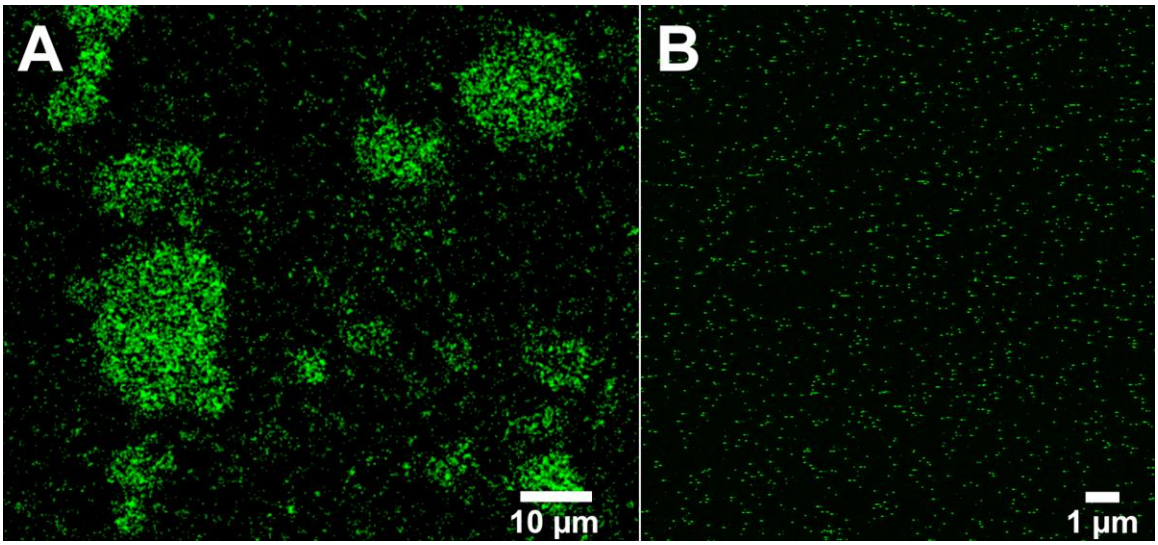

Figure 2.1: Confocal fluorescence microscopy images of (**A**) non-sonicated raw Er_2O_3 powder naturally aggregated to large micro-sized (> 10 µm) particles when mixed within the two-part silicone elastomer, making the suspension not suitable for microvascular perfusion. However, with sonication, nano-sized (~70 nm) particles were achieved (**B**).

The ability of a contrast agent to perfuse the microvasculature also depends on its viscosity. Measuring the viscosity of the uncured Er-based contrast agent – at 19.2 mPa·s – demonstrated agreement with the 20 mPa·s viscosity reported by the manufacturer of the two-part silicone elastomer, confirming that the uncured Er_2O_3 contrast agent is able to pass through small vessels under standard perfusion pressures.

Based on the measured viscosity of 19.2 mPa·s, the DLS measurement reported a Gaussian particle size distribution with mean hydrodynamic diameter of 64.8 nm, standard deviation of 11.1 nm, and a range from 44 to 122 nm (Figure 2.2 and A.1). Measurements of particle size and carrier viscosity indicated that the prepared Er_2O_3 suspension should easily pass through micro-vessels; this aspect of performance was further evaluated by micro-CT imaging of intact perfused mice.

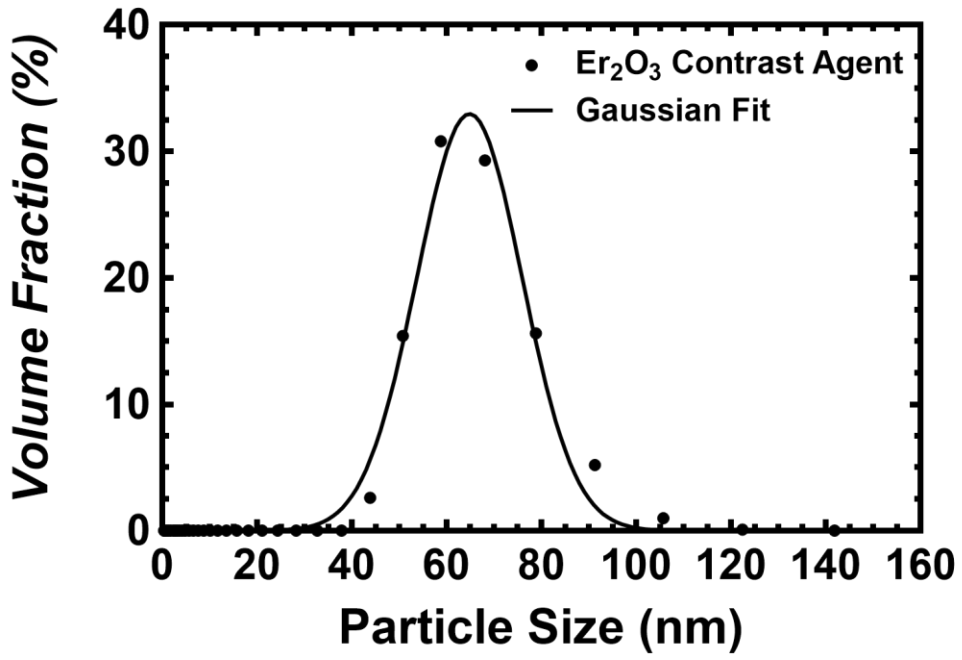

Figure 2.2: Dynamic light scattering (DLS) results demonstrating the particle size distribution of a sample of the Er_2O_3 contrast agent. Average particle size is 64.8 ± 11.1 nm. Results of a suspension that was mixed and subsequently stored for 2-years are shown in A.1.

Whole Er_2O_3-perfused C57Bl/6 mice scanned with 50 µm isotropic voxel spacing, and rebinned 2 × 2 to a final resolution of 100 µm, revealed a uniform and homogeneous distribution of the cured Er_2O_3 contrast agent within the vasculature throughout the entire perfused mouse (Figure 2.3). The vasculature displayed enhanced contrast in comparison to surrounding tissues throughout an intact animal; importantly the attenuation of the contrasted vessels was higher than that of bone.

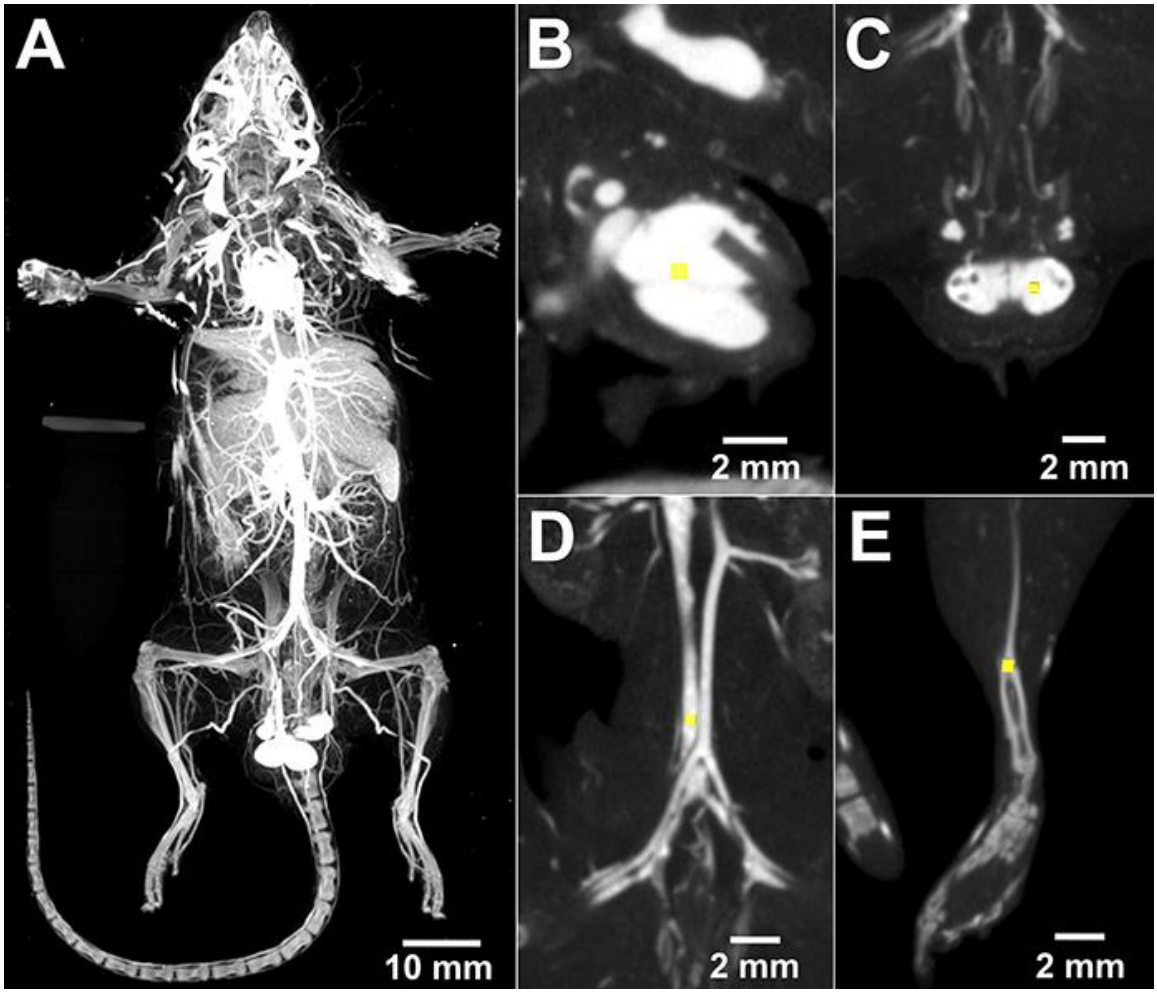

Figure 2.3: Rebinned 100 µm voxel images where the (**A**) Maximum intensity projection (MIP) of a whole-body perfused mouse demonstrates that the attenuation of the Er_2O_3 contrast agent in the vasculature is higher than the mouse's skeletal structure. Quantitative measurements of attenuation (in HU) were obtained from regions drawn within heart (**B**), testes (**C**), inferior vena cava (**D**), and cortical bone (**E**).

Scans of Er-contrast-perfused hindlimbs were acquired with 20 µm isotropic voxel spacing and subsequently rebinned 2 × 2 for a final resolution of 40 µm (Figure 2.4), to observe the smaller vasculature next to the dense bony structures of the femur and tibia. From these results, we were able to clearly see a feeding artery that runs within (Figure 2.4A) and along (Figure 2.4B) the entire length of each long bone. At this higher resolution, smaller structures such as a foramen (*i.e.* an opening for blood vessels to enter bone) can be visualized (Figure 2.4C). The ability to differentiate the foramen from the vessel running through it is particularly noteworthy, as this is not possible with other contrast agents that have lower attenuation coefficients. The observed perfusion of the venous system (Figure 2.4A yellow arrows) suggests successful perfusion of the capillaries, which is further supported by the lack of visible contrast-agent pooling within the interstitial space (pooling might have been observed if over-pressurization during perfusion had caused micro-vessel rupture).

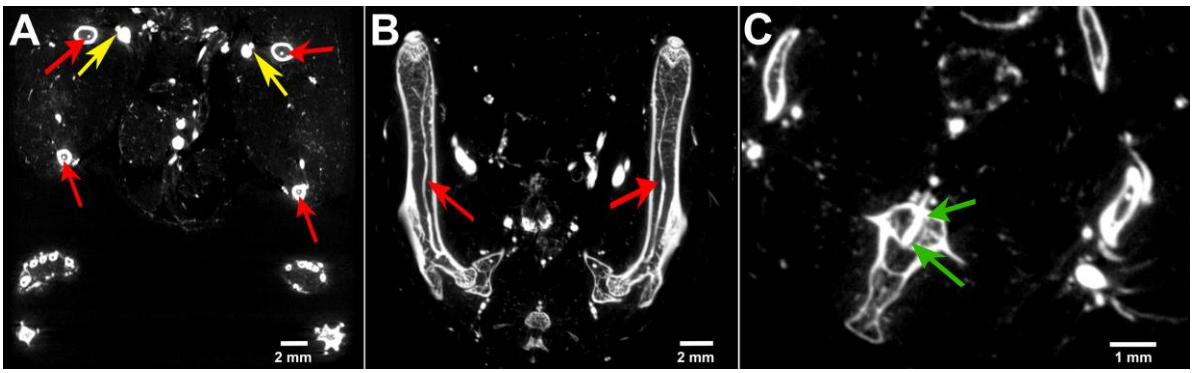

Figure 2.4: Multi-planar reformatted images at 40 µm, resulting from 2 × 2 rebinning of 20 µm acquired micro-CT scans, clearly depict the ability to visualize the extent of the nutrient arteries, which run along the tibia and femur. Red arrows highlight the nutrient arteries in cross-section in **(A)** and along their entire length in **(B).** At this resolution the depiction of parallel arteries and veins (yellow arrows) indicates successful perfusion through the capillary network. The ability to visualize vessels as they pass through a foramen (green arrows) into bone is depicted in **(C).**

2.3.2 Visualization of capillary bed perfusion

The results of the high-resolution micro-CT scan revealed that the Er_2O_3 contrast agent successfully perfused the entire continuous, well-ordered vascular tree of the kidney (Figure 2.5). The contrast enhancement of the vasculature was sufficiently high, such that a single grey-scale threshold separated perfused vasculature from surrounding tissues, allowing for the generation of 3D images of the kidney vessel microarchitecture (Figure 2.5B). The virtual Er_2O_3 vascular "cast" (Figure 2.5A and B) showed complete perfusion from the abdominal aorta (*i.e.* a main feeding vessel) down to the 6^{th} and 7^{th} arterial branches (*i.e.* glomeruli afferent arterioles). Previous research has shown that mouse glomeruli afferent arterioles can be as small as ~13 µm;[36] thus, visualization of individual glomeruli (*i.e.* several capillaries) suggests that our contrast agent is able to perfuse structures < 13 µm (Figure 2.5C and D). While previous research has shown perfusion of the kidney down to the afferent arterioles[36,40-42] using a commercially available lead-based contrast agent, the main advantage of the Er_2O_3 – based contrast agent is its ability to provide higher contrast and CNR.

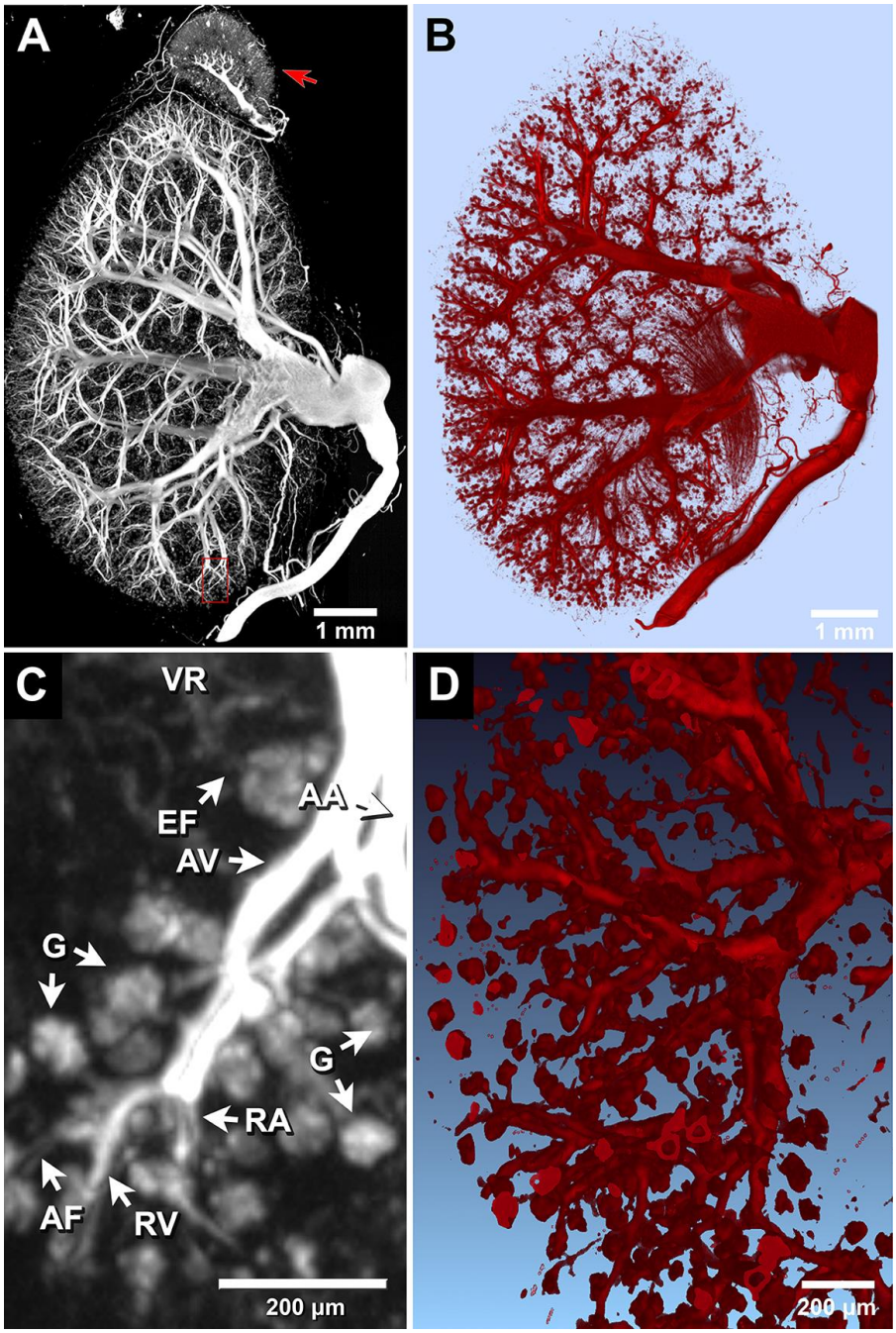

Figure 2.5: (A) MIP of an entire mouse kidney and attached adrenal gland (arrow) perfused with the new Er contrast agent. **(B)** 3D rendering of the perfused kidney with a plane cut to demonstrate an entire intact vascular tree. **(C)** magnified 0.35 mm thick slice MIP of the area outlined in red in **(A)**, demonstrating 6-7th level arterial branching. **(D)** 3D rendering of the terminal arteriole branches, ending in the glomeruli (the kidney's spherical capillary bed). G = glomeruli; AF = afferent arteriole; EF = efferent arteriole; RA = cruciate radial artery; RV = cruciate radial vein; AA = arcuate artery; AV = arcuate vein; and VR = vasa recta.

2.3.3 Contrast enhancement provided by the Er-based contrast agent in micro-CT

The measured mean CT values for the heart (4094 ± 264 HU), testes (4107 ± 182 HU), and IVC (4001 ± 305 HU), compared in Figure 2.6, showed no significance difference ($p = 0.3940$) between these three regions. On the other hand, the mean signal from cortical bone (2359 ± 207 HU) and the lead-based contrast agent Microfil MV-122 (2683 ± 77.6 HU) were significantly lower than the signal from the Er contrast-agent perfused vasculature ($p < 0.006$ and $p < 0.0001$ for bone and Microfil, respectively). The approximately 1400 HU difference in signal between that provided by the Er_2O_3 - based contrast agent and cortical bone will aid in facilitating the automatic segmentation of vessels from surrounding bone, which is not possible when commercially available contrast agents, such as Microfil MV 122, are used.

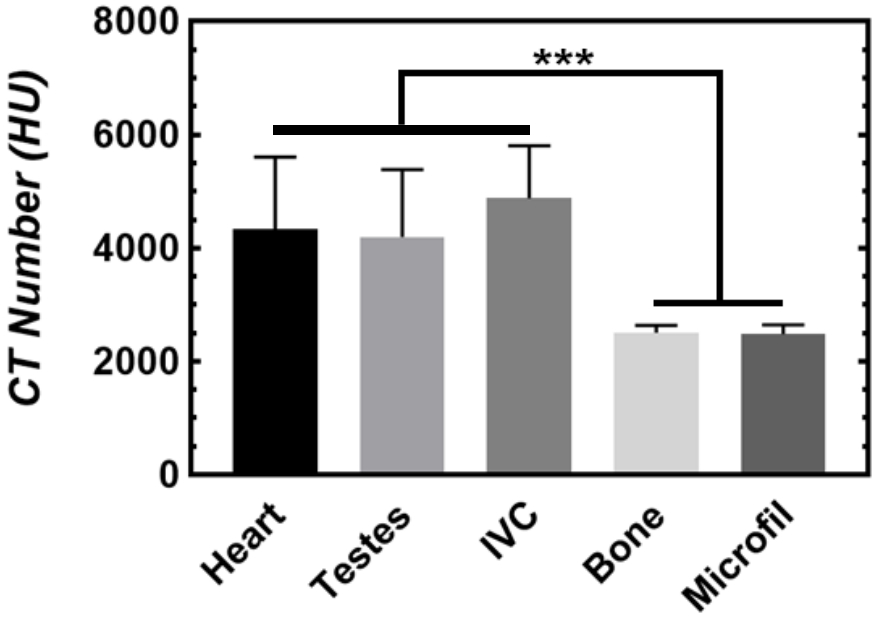

Figure 2.6: Heart, testes, and inferior vena cava (IVC) were chosen to represent the start, middle, and end of the perfusion route. The attenuation (HU) of the Er_2O_3 - based contrast agent in all three regions was significantly higher than that of cortical bone ($p < 0.006$, repeated measures ANOVA). Importantly, the attenuation of the Er_2O_3 – enhanced vasculature was significantly higher than that commercially available lead-based Microfil MV122 (one-way ANOVA,

$p < 0.0001$), while there was no difference between Microfil MV122 and cortical bone ($p > 0.9999$).

2.4 Discussion

We have demonstrated a methodology for the homogeneous incorporation of Er_2O_3 nanoparticles within a two-part silicone elastomer, forming a colloidal suspension capable of providing high x-ray attenuation that can facilitate the visualization and characterization of micro-vessels within a small animal model. In this study, we characterized and investigated the capabilities of the custom *ex vivo* Er-based vascular perfusion contrast agent.

Ultrasonic cavitation successfully broke down large naturally occurring Er_2O_3 aggregates (*i.e.* > 100 µm) into nm-sized particles (Figure 2.1B and 2.2) suspended within a silicone carrier. The prepared suspension was determined to possess low viscosity and a narrow particle size distribution that would facilitate the perfusion of intact whole-body mice (Figure 2.3). Micro-CT scans acquired with both 50 and 20 µm isotropic voxel spacings revealed whole-mouse perfusion and higher-ordered vascular branching (*i.e.* 1st to 3rd order) and visualization of vessels within bone (Figure 2.3 and 2.4). High-resolution scans with 5 µm spatial resolution demonstrated well-characterized vascular microarchitecture within a perfused kidney, with observed vascular filling down to vessels < 13 µm in diameter and contrast enhancement of capillary beds (*i.e.* glomeruli, Figure 2.5). Additionally, the attenuation of the Er-based contrast agent was found to be significantly higher than that of cortical bone (*i.e.* the densest naturally occurring substance within our samples) and the commonly used lead-based Microfil (MV-122) vascular contrast agent (Figure 2.6). This study clearly demonstrates the efficacy of the custom Er-based suspension as an *ex vivo* micro-CT vascular perfusion contrast agent.

An important benefit of the presented Er-based contrast agent is an x-ray attenuation coefficient that is significantly higher than that of both bone and other existing contrast agents. This difference facilitates the separation of microvessels from both soft tissue and bone in the images and can also result in a reduction of scan time. While shorter scans result in a greater amount of noise,[10] the higher contrast between the Er contrast agent

within the vasculature and surrounding tissue ensures that CNR remains high despite the shorter scan times. The approach used to incorporate the Er nanoparticles within the suspension (*i.e.* ultrasonic cavitation) renders the approach amenable to the production of custom contrast agents of varying elemental compositions and concentrations. Furthermore, silicone-compatible colorants can also be introduced within the silicone media to allow for the customization of the contrast agents' visual appearance against tissue; this may be useful for macroscopic visualization and post-mortem histological analysis.

In the current implementation, each working volume of contrast agent (*i.e.* 30 ml) is prepared individually, requiring approximately one hour of operator time. Larger volumes of contrast agent could be prepared in advance, with the curing catalyst being added just prior to usage. In this case, additional sonication may be required to ensure re-suspension of aggregated particles (Figure A.1).

As with other cast-forming contrast agents (*e.g.* Microfil) the new Er-based contrast agent is limited to applications of post-mortem vascular analysis at study endpoints. This limitation requires that larger cohorts of animals are needed to assess changes to the vasculature over periods of time. An *in vivo* contrast agent would make investigations with reduced sample size possible and allow for the study of vascular changes within the same animal over time; however, development of an *in vivo* contrast agent is not within the scope of this study. Currently, there exist *in vivo* contrast agents that reside within the blood pool for extended periods of time;[43,44] thus, we expect that the incorporation of Er into an *in vivo* agent is possible.

2.5 Conclusions

We have demonstrated the effectiveness of an Er-based suspension as a single-energy x-ray vascular contrast agent that significantly enhances the contrast – in comparison to surrounding dense bone and commercially available lead-based contrast agents (Figure 2.6) – of perfused vasculature within small animals (Figure 2.3-2.5). With an absorption K-edge at 57.5 keV, the Er-based contrast agent is also ideally suited for dual-energy micro-computed tomography (DECT) on a large installed base of high-resolution pre-

clinical micro-CT machines that operate at up to 90 kVp. The combination of the Er_2O_3-based vascular perfusion contrast agent with optimized DECT scan protocols and spectral shaping (using x-ray filtration) would facilitate rapid and automatic quantitative segmentation of perfused vasculature from surrounding tissues,[26] a process that is otherwise difficult due to partial volume effects that can limit traditional single-energy CT scans. Dual-energy CT-based material separation has been shown to be beneficial in studying a range of diseases in clinical applications (*i.e.* gout, cardiovascular, and cancer),[45-47] by allowing for the quantitative separation of the material of interest from surrounding tissues. The novel contrast agent that we describe has the potential to provide these advantages of DECT-based quantification and segmentation for pre-clinical investigations of vascular changes in small-animal models; this concept will be explored in Chapters 3 and 4.

2.6 References

1. A. J. LeBlanc, J. B. Hoying, Adaptation of the Coronary Microcirculation in Aging. *Microcirculation* **23**, 157-167 (2016).

2. C. T. Ambrose, The Role of Capillaries in the Lesser Ailments of Old Age and in Alzheimer's Disease and Vascular Dementia: The Potential of Pro-Therapeutic Angiogenesis. *J Alzheimers Dis* **54**, 31-43 (2016).

3. Z. Emrani, A. Karbalaie, A. Fatemi, M. Etehadtavakol, B.-E. Erlandsson, Capillary density: An important parameter in nailfold capillaroscopy. *Microvascular Research* **109**, 7-18 (2017).

4. C. N. Hall, C. Reynell, B. Gesslein, N. B. Hamilton, A. Mishra, B. A. Sutherland, F. M. O/'Farrell, A. M. Buchan, M. Lauritzen, D. Attwell, Capillary pericytes regulate cerebral blood flow in health and disease. *Nature* **508**, 55-60 (2014).

5. G. Katsuumi, I. Shimizu, Y. Yoshida, T. Minamino, The pathological role of vascular aging in cardio-metabolic disorder. *Inflammation and Regeneration* **36**, 16 (2016).

6. N. L. Ford, K. C. Graham, A. C. Groom, I. C. Macdonald, A. F. Chambers, D. W. Holdsworth, Time-course characterization of the computed tomography contrast enhancement of an iodinated blood-pool contrast agent in mice using a volumetric flat-panel equipped computed tomography scanner. *Invest Radiol* **41**, 384-390 (2006).

7. C. T. Badea, M. Drangova, D. W. Holdsworth, G. A. Johnson, In Vivo Small Animal Imaging using Micro-CT and Digital Subtraction Angiography. *Phys Med Biol* **53**, R319-R350 (2008).

8. L. Zagorchev, P. Oses, Z. W. Zhuang, K. Moodie, M. J. Mulligan-Kehoe, M. Simons, T. Couffinhal, Micro computed tomography for vascular exploration. *Journal of Angiogenesis Research* **2**, 7-7 (2010).

9. Y. Ding, W. O. Ward, T. Wasterlid, P. A. Gowland, A. M. Peters, J. Yang, L. Bai, Three-dimensional vessel segmentation using a novel combinatory filter framework. *Phys Med Biol* **59**, 7013-7029 (2014).

10. N. L. Ford, M. M. Thornton, D. W. Holdsworth, Fundamental image quality limits for microcomputed tomography in small animals. *Med Phys* **30**, 2869-2877 (2003).

11. G. J. Schwartz, S. L. Furth, Glomerular filtration rate measurement and estimation in chronic kidney disease. *Pediatric Nephrology* **22**, 1839-1848 (2007).

12. T. S. Desser, D. L. Rubin, H. Muller, G. L. McIntire, E. R. Bacon, J. L. Toner, Blood pool and liver enhancement in CT with liposomal lodixanol: Comparison with lohexol. *Academic Radiology* **6**, 176-183 (1999).

13. S. A. Detombe, J. Dunmore-Buyze, M. Drangova, Evaluation of eXIA 160XL cardiac-related enhancement in C57BL/6 and BALB/c mice using micro-CT. *Contrast Media & Molecular Imaging* **7**, 240-246 (2012).

14. P. Blery, P. Pilet, A. V. Bossche, A. Thery, J. Guicheux, Y. Amouriq, F. Espitalier, N. Mathieu, P. Weiss, Vascular imaging with contrast agent in hard and soft tissues using microcomputed-tomography. *J Microsc* **262**, 40-49 (2016).

15. S. A. Detombe, N. L. Ford, F. Xiang, X. Lu, Q. Feng, M. Drangova, Longitudinal follow-up of cardiac structure and functional changes in an infarct mouse model using retrospectively gated micro-computed tomography. *Invest Radiol* **43**, 520-529 (2008).

16. A. Y. Sheikh, K. E. A. van der Bogt, T. C. Doyle, M. K. Sheikh, K. J. Ransohoff, Z. A. Ali, O. P. Palmer, R. C. Robbins, M. P. Fischbein, J. C. Wu, Micro-CT for Characterization of Murine CV Disease Models. *JACC. Cardiovascular imaging* **3**, 783-785 (2010).

17. M. D. Bentley, M. C. Ortiz, E. L. Ritman, J. C. Romero, The use of microcomputed tomography to study microvasculature in small rodents. *Am J Physiol Regul Integr Comp Physiol* **282**, R1267-1279 (2002).

18. D. S. Perrien, M. A. Saleh, K. Takahashi, M. S. Madhur, D. G. Harrison, R. C. Harris, T. Takahashi, Novel methods for microCT-based analyses of vasculature

in the renal cortex reveal a loss of perfusable arterioles and glomeruli in eNOS-/- mice. *BMC Nephrology* **17**, 24 (2016).

19. K. C. Graham, N. L. Ford, L. T. MacKenzie, C. O. Postenka, A. C. Groom, I. C. MacDonald, D. W. Holdsworth, M. Drangova, A. F. Chambers, Noninvasive quantification of tumor volume in preclinical liver metastasis models using contrast-enhanced x-ray computed tomography. *Invest Radiol* **43**, 92-99 (2008).

20. H. Nyangoga, P. Mercier, H. Libouban, M. F. Basle, D. Chappard, Three-dimensional characterization of the vascular bed in bone metastasis of the rat by microcomputed tomography (MicroCT). *PLoS One* **6**, e17336 (2011).

21. M. Zamir, J. Twynstra, A. J. Vercnocke, I. Welch, S. M. Jorgensen, E. L. Ritman, D. W. Holdsworth, J. K. Shoemaker, Intrinsic microvasculature of the sciatic nerve in the rat. *Journal of the Peripheral Nervous System* **17**, 377-384 (2012).

22. S. Ghanavati, L. X. Yu, J. P. Lerch, J. G. Sled, A perfusion procedure for imaging of the mouse cerebral vasculature by X-ray micro-CT. *J Neurosci Methods* **221**, 70-77 (2014).

23. M. Cavaglia, S. M. Dombrowski, J. Drazba, A. Vasanji, P. M. Bokesch, D. Janigro, Regional variation in brain capillary density and vascular response to ischemia. *Brain Research* **910**, 81-93 (2001).

24. C. L. Duvall, W. R. Taylor, D. Weiss, R. E. Guldberg, Quantitative microcomputed tomography analysis of collateral vessel development after ischemic injury. *American Journal of Physiology - Heart and Circulatory Physiology* **287**, H302-H310 (2004).

25. L. Jósza, M. U. Lehto, M. Järvinen, M. Kvist, A. Réffy, P. Kannus, A comparative study of methods for demonstration and quantification of capillaries in skeletal muscle. *Acta histochemica* **94**, 89-96 (1993).

26. P. V. Granton, S. I. Pollmann, N. L. Ford, M. Drangova, D. W. Holdsworth, Implementation of dual- and triple-energy cone-beam micro-CT for postreconstruction material decomposition. *Med Phys* **35**, 5030-5042 (2008).

27. H.-Y. Kim, J. O. Sofo, D. Velegol, M. W. Cole, A. A. Lucas, Van der Waals Dispersion Forces between Dielectric Nanoclusters. *Langmuir* **23**, 1735-1740 (2007).

28. N. M. Kovalchuk, V. M. Starov, Aggregation in colloidal suspensions: Effect of colloidal forces and hydrodynamic interactions. *Advances in Colloid and Interface Science* **179–182**, 99-106 (2012).

29. X. Zhao, D. Ho, S. Gao, C. Hong, D. E. Vatner, S. F. Vatner, Arterial Pressure Monitoring in Mice. *Current protocols in mouse biology* **1**, 105-122 (2011).

30. T. L. Cunliffe-Beamer, in *The Mouse in Biomedical Research*, J. D. Small, J. G. Fox, Eds. (Academic Press, 1983), pp. 401-437.

31. M. Marxen, M. M. Thornton, C. B. Chiarot, G. Klement, J. Koprivnikar, J. G. Sled, R. M. Henkelman, MicroCT scanner performance and considerations for vascular specimen imaging. *Medical Physics* **31**, 305-313 (2004).

32. A. Dorr, J. G. Sled, N. Kabani, Three-dimensional cerebral vasculature of the CBA mouse brain: A magnetic resonance imaging and micro computed tomography study. *NeuroImage* **35**, 1409-1423 (2007).

33. D. Sarhaddi, B. Poushanchi, M. Merati, C. Tchanque-Fossuo, A. Donneys, J. Baker, S. R. Buchman, Validation of Histologic Bone Analysis Following Microfil Vessel Perfusion. *Journal of histotechnology* **35**, 180-183 (2012).

34. D. B. Berry, S. You, J. Warner, L. R. Frank, S. Chen, S. R. Ward, A 3D Tissue-Printing Approach for Validation of Diffusion Tensor Imaging in Skeletal Muscle. *Tissue Eng Part A*, (2017).

35. K. Sarveswaran, V. Kurz, Z. Dong, T. Tanaka, S. Penny, G. Timp, Synthetic Capillaries to Control Microscopic Blood Flow. *Sci Rep* **6**, 21885 (2016).

36. S. X. Vasquez, F. Gao, F. Su, V. Grijalva, J. Pope, B. Martin, J. Stinstra, M. Masner, N. Shah, D. M. Weinstein, R. Farias-Eisner, S. T. Reddy, Optimization of MicroCT Imaging and Blood Vessel Diameter Quantitation of Preclinical Specimen Vasculature with Radiopaque Polymer Injection Medium. *PLoS One* **6**, e19099 (2011).

37. B. J. Hillman, S. M. Lee, G. Wilson, In vivo barium microangiography in the mouse. *Invest Radiol* **15**, 145-147 (1980).

38. D. A. Rytand, The number and size of mammalian glomeruli as related to kidney and to body weight, with methods for their enumeration and measurement. *American Journal of Anatomy* **62**, 507-520 (1938).

39. P. Granton, M. Podesta, G. Landry, S. Nijsten, G. Bootsma, F. Verhaegen, *A combined dose calculation and verification method for a small animal precision irradiator based on onboard imaging*. (2012), vol. 39, pp. 4155-4166.

40. R. Xu, F. Franchi, B. Miller, J. A. Crane, K. M. Peterson, P. J. Psaltis, P. C. Harris, L. O. Lerman, M. Rodriguez-Porcel, Polycystic Kidneys Have Decreased Vascular Density: A Micro-CT Study. *Microcirculation* **20**, 183-189 (2013).

41. R. Savai, A. C. Langheinrich, R. T. Schermuly, S. S. Pullamsetti, R. Dumitrascu, H. Traupe, W. S. Rau, W. Seeger, F. Grimminger, G. A. Banat, Evaluation of angiogenesis using micro-computed tomography in a xenograft mouse model of lung cancer. *Neoplasia* **11**, 48-56 (2009).

42. A. Garcia-Sanz, A. Rodriguez-Barbero, M. D. Bentley, E. L. Ritman, J. C. Romero, Three-dimensional microcomputed tomography of renal vasculature in rats. *Hypertension* **31**, (1998).

43. S. You, H. Y. Jung, C. Lee, Y. H. Choe, J. Y. Heo, G. T. Gang, S. K. Byun, W. K. Kim, C. H. Lee, D. E. Kim, Y. I. Kim, Y. Kim, High-performance dendritic contrast agents for X-ray computed tomography imaging using potent tetraiodobenzene derivatives. *J Control Release* **226**, 258-267 (2016).

44. Y. Zou, Y. Wei, G. Wang, F. Meng, M. Gao, G. Storm, Z. Zhong, Nanopolymersomes with an Ultrahigh Iodine Content for High-Performance X-Ray Computed Tomography Imaging In Vivo. *Advanced Materials* **29**, 1603997-n/a (2017).

45. M. Uhrig, D. Simons, D. Bonekamp, H.-P. Schlemmer, Improved detection of melanoma metastases by iodine maps from dual energy CT. *Eur J Radiol* **90**, 27-33.

46. I. Danad, B. Ó Hartaigh, J. K. Min, Dual-energy computed tomography for detection of coronary artery disease. *Expert review of cardiovascular therapy* **13**, 1345-1356 (2015).

47. Y. H. Lee, G. G. Song, Diagnostic accuracy of dual-energy computed tomography in patients with gout: A meta-analysis. *Semin Arthritis Rheum*, (2017).

Chapter 3

3 Dual-Energy Computed Tomography for a Gantry-Based Pre-Clinical Cone-Beam Micro-CT Scanner

3.1 Introduction

Micro-computed tomography (micro-CT) is widely utilized in biological studies for its capability of providing high-resolution images of contrasting tissues. Attenuation within micro-CT images is dependent on the materials' effective atomic number (*i.e.* Z, electron density), where higher Z materials (*i.e.* higher electron density) will exhibit higher x-ray attenuation due to photoelectric absorption.[1,2] For biological samples, bone can be easily visually separated from surrounding soft tissues (*i.e.* muscle, fat, etc.) due to its composition. However, discrimination between soft tissues is difficult, due to their relatively similar electron densities.[3] To enhance the visualization of soft tissues, tissue-specific exogeneous contrast agents are commonly required.[4,5] Vascular contrast agents (*i.e.* angiography), are routinely used to facilitate the visualization and distinction of perfused vasculature from surrounding non-contrast enhanced soft tissues.[6]

Clinical angiography typically employs the use of iodine-based contrast agents.[7-9] X-ray images of perfused vasculature are markedly different – due to the increased contrast – from surrounding soft tissue, allowing for the automatic segmentation of contrasted-vessels based on greyscale values alone.[10] However, due to the dilution of injected iodine-based contrast agents and its diffusion within the blood stream, the contrast enhancement of vessels is often masked by nearby dense bone. For *in vitro* and *ex vivo* applications, more highly x-ray attenuating vascular agents such as lead-based silicone elastomers (Microfil MV-122, Flowtech, Inc., MA, USA) can be utilized.[11] Nonetheless, the mean CT signal level of perfused vessels appears similar to cortical bone, hindering their automatic separation based on greyscale values.[5,12]

Dual-energy micro-CT (DECT) is an x-ray imaging technique that can facilitate the automatic decomposition and segmentation of materials based on their elemental composition. Dual-energy CT is used clinically for angiography[13] and kidney stone

identification.[14] As the name implies, DECT involves scanning a sample at different energy spectra – achieved through differing acquisition protocols. Each material exhibits a unique elemental x-ray attenuation signature; thus, within composite samples, DECT decomposes each material based on their differential contrast at two different x-ray energies. The performance and image decomposition of DECT can be further improved if the dual-energy spectra are tailored to a material's absorption K-edge.

Every material possesses a unique absorption K-edge energy (*i.e.* the x-ray energy required to eject an inner K-shell electron), which leads to a significant increase in x-ray attenuation when x-ray energies are above the K-edge energy. Dual-energy CT performed with mean spectral x-ray energies above and below the K-edge of interest takes advantage of this increased attenuation to improve the decomposition of materials of interest. There are multiple avenues to performing DECT, whether it is through fast kV-switching,[15,16] dual-source,[15] or dual-detector CT scanners.[17] However, the large installed base of conventional pre-clinical micro-CT scanners are limited to scanning at a single x-ray energy at a time. The inherently polychromatic nature (i.e. implement with a broad x-ray spectrum) of these micro-CT scanners requires the careful selection of dual-energy acquisition protocols, as large amounts of spectral overlap will reduce the effectiveness of DECT decompositions.

Spectral separation between the low- and high-energy images can be achieved through spectral shaping with differential added filtration to optimize the performance of DECT.[18-21] This has been successfully shown in previous research,[5] where copper and lead foils were utilized to facilitate the necessary spectral separation, resulting in the DECT decomposition of a rat hindlimb (perfused with a lead-based contrast agent) into separate images of bone and vasculature. However, a limitation associated with the use of a lead-based dual-energy contrast agent is that the high K-edge energy of lead (88 keV) necessitates the use of a high x-ray tube potential (*e.g.* 140 kVp) to achieve adequate spectral separation.[5] However, many pre-clinical micro-CT scanners are limited to maximum tube potentials of approximately 80 – 90 kVp, which reduces the effectiveness of DECT with Pb-based contrast agents (due to limited photon flux above the K-edge at 88 keV).

A DECT-compatible erbium (Er)-based *ex vivo* vascular perfusion contrast agent has been previously developed and characterized.[22] The Er-based suspension is ideally suited for DECT as its absorption K-edge (*i.e.* 57.5 keV) is located close to the mean energy of micro-CT scanners (~42.7 kVp) with a 90 kVp maximum tube potential. Nonetheless, optimizing DECT for an Er-based agent requires spectral shaping tailored to erbium's K-edge, through the addition of x-ray filtration. Typically, the low- and high-energy images will be acquired sequentially, with different filters; this leads to the potential for geometric misregistration between image volumes, due to non-reproducible scanner gantry movements. It may therefore be necessary to implement a method of image co-registration between acquired low- and high-energy image volumes.

This study outlines the design, implementation, and evaluation of optimized DECT on a pre-clinical cone-beam gantry-based micro-CT scanner. In this investigation, we describe a technique for the fabrication of: (1) custom x-ray filters to facilitate the needed spectral separation on pre-clinical high-resolution gantry-based micro-CT scanners; (2) fiducial marker-based image co-registration to correct for inherent micro-CT scanner bed and gantry movement between sequential scans; and, (3) a motorized filter-exchange mechanism for automated DECT acquisition. The evaluation of DECT was visually and quantitatively confirmed through the automated decomposition of rat hindlimbs – perfused with an Er-based vascular contrast agent – into individual volumes of soft tissue, bone, and perfused vessels. The combination of the readily available techniques and materials outlined throughout this study will allow users of a large installed base of micro-CT scanners limited to scanning at a single x-ray energy at a time to perform optimized DECT.

3.2 Materials and Methods

3.2.1 Spectral Shaping and Modeling

X-ray spectra were modelled using a previously developed computational tool for x-ray spectral simulation (Spektr 2.0).[23] This model incorporated CT scanner-specific parameters, such as target angle of 15°, source-to-isocenter distance of 22.59 cm, additional anode inherent filtration equivalent to 1.0 mm Al (Dunlee, DU 404), and 2 cm

Lexan. Spectra were modelled with varying thicknesses of x-ray filtering materials and simulated at 0.5 kVp increments. All modelling and calculations were performed within Matlab (R2016b, MathWorks Inc, Natick, MA, USA).

Selection of the optimal parameters for low- and high-energy DECT scans involves the choice of x-ray energy (*i.e.* kVp), type of filtration (*i.e.* elemental composition), and thickness of filtration. The process necessarily involves a balance between optimizing x-ray photon flux while maintaining sufficient spectral separation. Added filtration is used to increase the mean energy of the spectrum and to reduce the width of the spectrum. In the absence of filtration (*i.e.* maximum photon flux), high signal-to-noise (SNR) images can be acquired; however, the lack of spectral separation between the low- and high-energy spectra will reduce the accuracy of DECT decompositions – visualized as misclassified voxels between decomposed volumes. Conversely, excessive filtration will enhance spectral separation, yet the resulting diminished photon flux will result in poor SNR images, again compromising DECT decomposition accuracy.

We chose 90 kVp as the tube potential for the high-energy spectrum, as the mean energy of the unfiltered spectrum (~42.7 kVp) is close to erbium's absorption K-edge (57.5 keV). Additionally, 90 kVp is typical the maximum tube potential of a large installed base of laboratory micro-CT scanners. The low-energy spectrum was set at 70 kVp, to provide efficient x-ray production and ensure adequate photon flux just below the absorption K-edge of Er. With the low- and high-energy tube potentials selected, it was necessary to choose materials for differential x-ray filtration to facilitate the spectral separation required for optimized DECT.

To filter the high-energy spectrum, copper (Cu) was selected to preferentially attenuate low-energy photons, thereby shifting the mean energy higher. In addition, copper is available in foil-form at varying thicknesses and low cost; it is widely used as a x-ray filter for both single-[24-26] and dual-energy CT.[5,27] To model the behavior of Cu, the x-ray cross section of Cu was obtained from the National Institute of Standards and Technology's (NIST) online database. Using the modelled output x-ray spectrum of our micro-CT scanner (GE Vision 120, GE HealthCare, London, Ontario), a total Cu path

length of 550 μm was calculated for a photon flux reduction of 70% (Figure 3.1b). Previous research with a rat hindlimb perfused with a Pb-based agent,[5] has shown that a 70% photon flux reduction (*i.e.* 30% photon transmission) resulted in sufficient spectral separation to facilitate the decomposition of DECT images into segmented bone and perfused vessel images.

To filter the low-energy spectrum, we selected an Er-based filter, as it will inherently attenuate photons above 57.5 keV. Using the cross-sectional values of Er from NIST, a calculated Er thickness of 68 μm would provide a 50% photon flux reduction, generating a photon flux similar to that of the filtered high-energy spectrum (Figure 3.1, bottom panel).

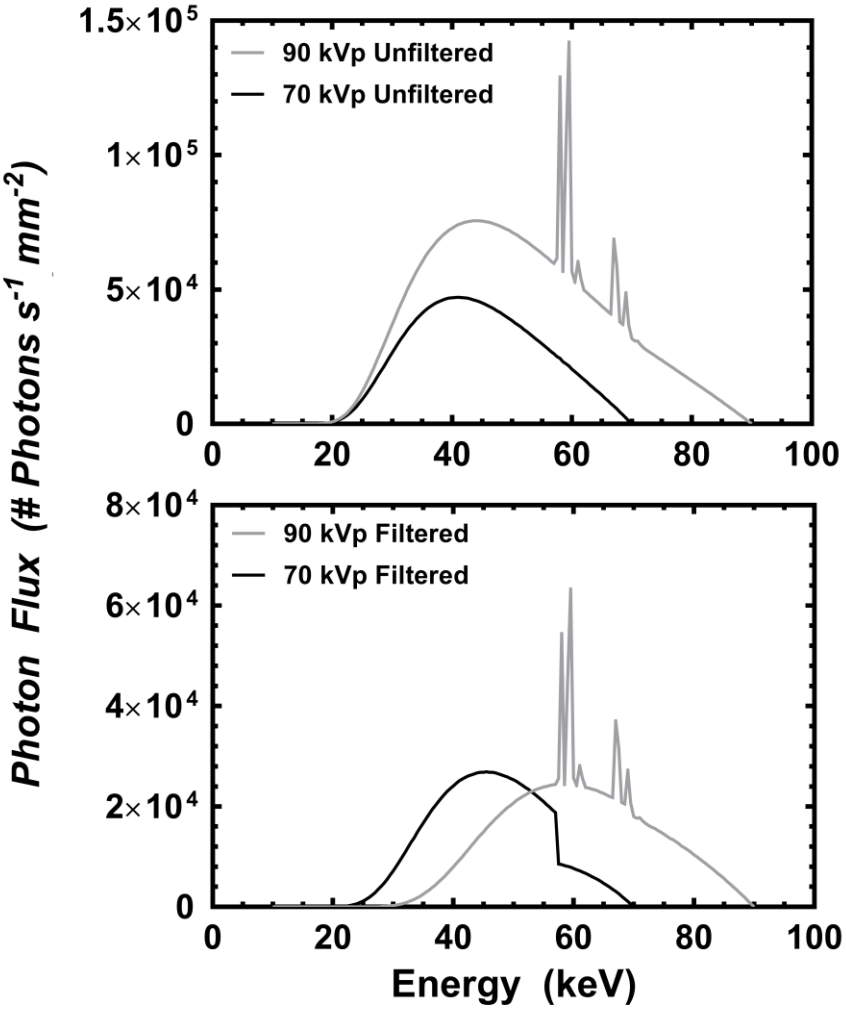

Figure 3.1: Computer modelled spectral distributions of the chosen 70 and 90 kVp low- and high-energy spectra, respectively. (**Top panel**) Results of the modelled unfiltered 70 and 90 kVp spectra. (**Bottom panel**) Modelled spectra of the 70 and 90 kVp with the addition of filtration to increase spectral separation and reduction of overall photon flux.

3.2.2 X-ray Filter Fabrication

The Cu and Er filters described above can be implemented on bench-top specimen micro-CT scanners by placing metal foils at the x-ray tube port, prior to the sample. However, for use with gantry-based micro-CT scanners, it may not be possible or practical to modify the system in this manner. The addition of a mechanism to mount the filters on the tube port – and exchange them between scans – may interfere with the normal operation of the scanner and gantry balance. For these reasons, we elected to implement

an annular cylindrical filter that surrounds the scan bed yet fits within the scanner bore. This approach to filtration avoids modifications to the scanner and is compatible with gantry-based scanners.[5] Although the annular filter acts through a combination of pre- and post-object filtration, it provides a total attenuation that is equivalent to a pre-object filter of identical path length.

A high-energy Cu x-ray filter was fabricated from readily available Cu foil. Sheets of 0.08 mm Cu foil were wrapped around an acrylic annular cylinder, with dimensions of 8.2 cm outer diameter (OD) × 6.4 cm height (H) × 0.3 cm wall thickness (WT). These dimensions were chosen to be slightly less than the maximum field-of-view (FOV) size for the selected micro-CT scanner (Vision 120, GE HealthCare, London, ON, CAN), facilitating the reconstruction of the entire x-ray filter and sample during DECT-acquisitions. A total of three individual layers of Cu foil provided a total pathlength of 0.48 mm, resulting in a photon flux reduction of 66%. However, unlike the high-energy x-ray filter, fabrication of the low-energy Er x-ray filter remained challenging, as sufficiently large sheets of Er are not readily available and may be prohibitively costly. Therefore, this led us to develop a new methodology, which allowed the creation of cast nano-powder-incorporated resin-based annular filters; in our case, inexpensive erbium oxide nanoparticles.

To craft a custom cylindrical Er x-ray filter, a master filter shape and its respective negative silicone mold were required. The master cylindrical annular shape was machined from a solid cylindrical aluminum stock (Al, Alloy 6061, McMaster-Carr, Aurora, OH) till dimensions of 8.2 OD × 6.4 cm H × 0.3 cm WT were achieved. The bottom-half of the mold was constructed by embedding the Al filter in a thin layer (~ 1 cm) of sulfur-free clay (Monster Clay, OH, USA) within an acrylic “box” (Figure 3.2b); exact box dimensions are not critical. Several registration keys, fashioned from clay, were placed throughout the mold. The silicone elastomer mixture was prepared as instructed by the manufacturer (Bluestar Silicones RTV 4420 QC, NJ, USA), poured into the acrylic box and allowed to cure (~1 hr, Figure 3.2d). The respective top-half of the mold was created by inverting the cured silicone and Al filter, removing the clay and spraying exposed surfaces with mold release (Smooth-Cast® Ease-Release, PA,

USA). Fill and evacuation ports were modelled from clay and affixed to the Al filter. A second batch of silicone elastomer mixture was poured to cover the exposed Al filter and allowed to cure (Figure 3.2de). The tight fit of the co-registered two-part mold (Figure 3.2f) would prevent leaking of the poured Er-infused resin casting mixture.

To cast the low-energy Er x-ray filter, erbium oxide (Er_2O_3, American Elements, CA, USA) nanoparticles (nominal diameter ~ 50 nm) were incorporated within a 9-minute pot-life two-part resin mixture (Smooth-Cast® 321, Smooth-On, PA, USA). To create an effective Er-foil pathlength of 68 μm, 5.27 g of Er_2O_3 was mixed thoroughly with 30 mL of Part B and placed in a vacuum chamber (~101.3 kPa) until all air bubbles had been evacuated. An equal volume of Part A (30 mL) was carefully mixed with the Part B and Er_2O_3 mixture for a total of 2.5 minutes. The resin mixture was placed back into the vacuum chamber for an additional 2.5 minutes (achieving ~ 68 kPa). To minimize introduction of air bubbles during casting, the resin mixture was poured as a slow and thin continuous stream into the fill port of the silicone mold (Figure 3.2f). The Er-infused resin was cured overnight before extraction and removal of excess resin (Figure 3.2g). The cast low-energy Er x-ray filter resulted in a 49% reduction of photon flux.

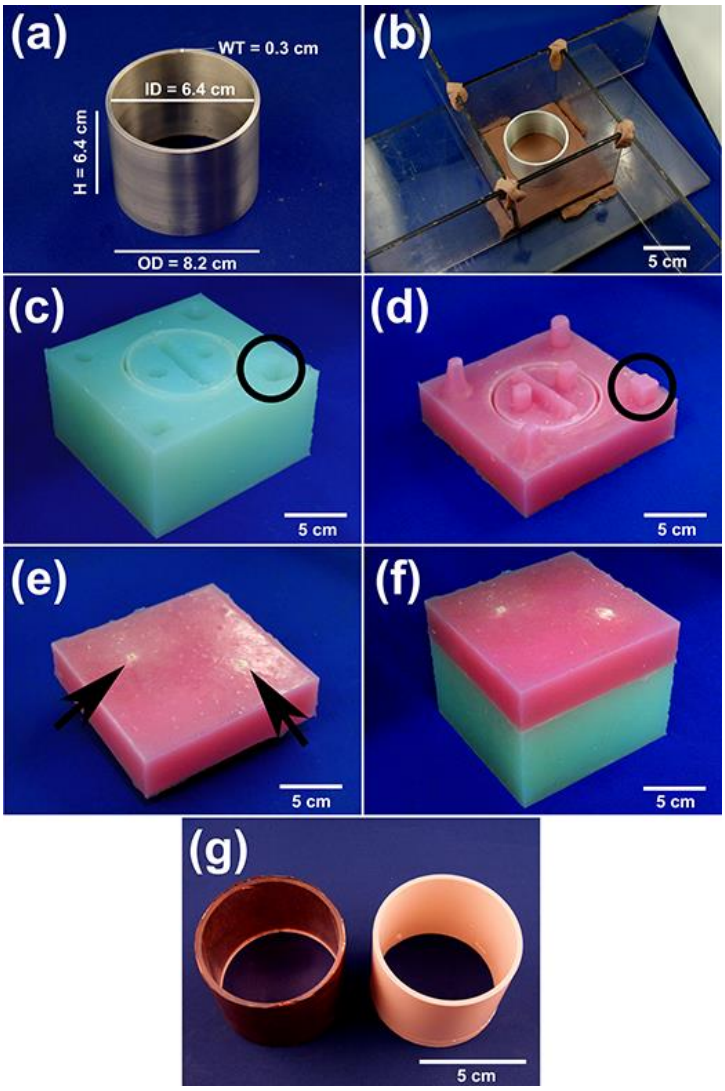

Figure 3.2: Process implemented to fabricate a custom silicone mold used to cast custom resin x-ray filters. (**a**) Master machined aluminum (Al) filter. (**b**) Assembled box, comprised of multiple acrylic pieces, to encompass the two-part silicone that is to be poured over the embedded Al filter within a layer of sulphur-free clay. (**c**) Extracted silicone mold representing the bottom-half of the silicone mold. Circle emphasizes one of the 7 registration keys that were used to ensure accurate assembling of the silicone bottom- and top-half. (**d**) Silicone mold of the top-half. Circle represents the corresponding registration key from (**c**). (**e)** Top-half of the silicone mold flipped to demonstrate the fill and evacuation ports (arrows). (**f**) Assembled silicone mold. (**g**) Fabricated custom x-ray filters, the erbium-impregnated resin casted low-energy filter (right) and the copper foil wrapped around acrylic core high-energy filter (left).

3.2.3 Dual-Energy Micro-Computed Tomography

All samples were scanned with our DECT protocols on a pre-clinical gantry-based cone-beam micro-CT scanner (Vision 120, GE Healthcare, London, ON, CAN). The low-energy scan parameters were 70 kVp, the additional Er-cast resin filter (as previously described), and 50 mA. The high-energy was acquired at 90 kVp, with the previously mentioned Cu filter, and 40 mA. Both low- and high-energy scans were acquired with 50 μm isotropic voxel spacings, 1200 projections at 0.3° increments over 360°, 10 frames averaged per projection, and 16 ms per frame. The total time required for each energy scan was approximately 1.5 hrs, which included the time required for gantry motion and recording of image projections; thus, a complete DECT scan was ~3 hrs. Reconstructed three-dimensional (3D) images were rebinned 2 × 2, resulting in 100 μm isotropic voxel spacing. Images were rescaled into Hounsfield units (HU) using vials of water and air within the field of view.

3.2.3.1.1 Image Co-Registration

Fiducial markers beads (1.6 mm polytetrafluoroethylene (PTFE), Teflon™, Figure 3.3b circles) were embedded in a distributed pattern (Figure 3.3ab) throughout a custom radiolucent polystyrene foam sample holder. Fiducial markers of PTFE were chosen as they provided sufficient contrast (making them easily segmented) and introduced minimal image artifacts. The centroid of a minimum of eight fiducial markers were used to derive a transformation matrix using a least-square fitting method;[28] wherein the high-energy image was rigidly transformed to the low-energy image with sub-voxel accuracy.

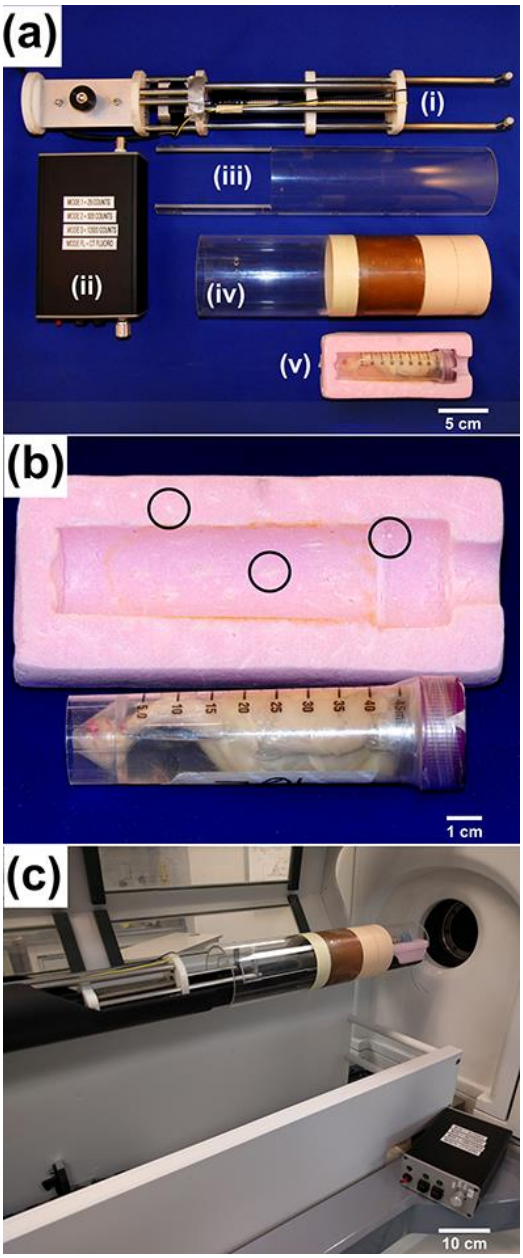

Figure 3.3: Instrumentation implemented on the micro-CT scanner, which facilitated the switching of x-ray filters and aided in image co-registration. (**a**) Individual pieces of the automated filter-exchange mechanism: (**i**) linear actuator filter-exchanger; (**ii**) control box for filter-exchange mechanism; (**iii**) clam shell which resides on the CT scan bed to support the x-ray filters; (**iv**) custom Er and Cu x-ray filters mounted to an acrylic cylinder; and, (**v**) radiolucent sample holder and sample. (**b**) Enhanced view of sample holder (**a-v**) to emphasize the many embedded fiducial markers, three of which have been encircled. (**c**) The entire setup assembled on our micro-CT scanner.

DECT Automation

To increase sample throughput and reduce operator dependencies, a motorized filter-exchange mechanism (Figure 3.3) was constructed to automate the DECT acquisition process. The filter-exchange mechanism automatically switches x-ray filters within the scanner bore, in between the low- and high-energy scans. Mounted on an acrylic cylinder (with an OD and WT identical to the master Al filter), the custom Er and Cu x-ray filters were actuated with a motor-driven lead screw (Figure 3.3ai) controlled by an embedded micro-controller (Arduino Uno, Figure 3.3aii). The filter-exchange mechanism assembly was secured on the micro-CT scan bed with a simple screw jack system.

3.2.4 Contrast Agent Preparation

The preparation of the Er-based *ex vivo* vascular perfusion contrast agent has been previously described in Chapter 2;[22] briefly, perfusion of a sample required the formulation of a catalyzing curing agent and the Er-based suspension.

The curing agent and Er-based contrast agent were prepared prior to perfusion in accordance to Chapter 2. The curing agent was comprised of 60% v/v dibutyl tin dilaurate (DBT) and 40% v/v tetraethylorthosilicate (TEOS) mixed until a homogeneous transparent pale-yellow colour was achieved. The Er-based contrast agent was comprised of a two-part silicone elastomer (Microfil 132, FlowTech Inc, MA, USA) with uniformly dispersed Er_2O_3 nanoparticles (nominal diameter 50 nm, Nanostructured and Amorphous Materials, TX, USA). To create a volume of 30 mL, sufficient for a single rat hindlimb perfusion, 4.0 g of Er_2O_3 (13.3 % w/v) was mixed within 8.73 ml of MV-132 and 17.47 ml of MV-Diluent and probe sonicated for a total of 35 minutes.[22] The remaining 3.8 mL was comprised of the curing agent, as described above, added immediately prior to perfusion.

3.2.5 Rat Hindlimb Perfusion

A custom catheter with sufficient flexibility was created to aid in its manipulation during surgery and prevention of accidental vessel tearing upon insertion. The catheter was comprised of a blunted 18 G (BD, NJ, USA) needle with 15 cm of polyethylene tubing

(#1417011F, Fisher Scientific, NH, USA) and 10 cm silicone tubing tip (#60985-724, VWR, PA, USA). To join the silicone and polyethylene tubing, the silicone tubing was placed in diethyl ether (Sigma Aldrich, MI, USA) for ~10 s, causing the tubing to swell and ease its placement over the polyethylene tubing. A bevel was introduced on the tip of the silicone tubing.

The Animal Use Subcommittee at the University of Western Ontario approved all animal experiments (protocol #2015-018). Ten male wild-type Sprague-Dawley rats (Harlan, Indianapolis, IN, USA) were anesthetized and maintained with 3% isoflurane (in 2% O_2) isoflurane (Sandoz, QC, CAN). Five minutes prior to surgery, a jugular injection of 500 µl heparin (to prevent blot clotting) was administered. An incision along the abdomen was made, and organs were parted till the aorta and inferior vena cava (IVC) were visualized. The parietal peritoneum covering the IVC and aorta was carefully separated from the underlying vessels using gauze. Two lengths of silk thread (~ 8 cm) were passed in between the separated aorta and IVC. One length of thread was used to tie off the aorta below the renal artery. Downstream of the tied-off aorta, a small incision was made in the aorta. The custom catheter (as described above) was inserted and maneuvered until the tip of the catheter was ~ 1- 2 cm above the aortic bifurcation. The second thread was gently tied off around the aorta and catheter, holding the catheter in place. The IVC was severed to allow for circulatory drainage. Hindlimbs were flushed with ~250 mL of 0.4% heparinized saline prior to perfusion of the Er-based contrast agent.

3.8 mL of the prepared curing agent was added to the Er-suspension and vortexed continuously for 8 minutes. The mixture was injected into an IV bag and suspended 175 cm above the animal, equivalent to 129 mm Hg. The contrast agent was perfused until cured (*i.e.* ~37 minutes post addition of curing agent). Rat hindlimbs were fixed in 10% formalin for at least 2 weeks prior to the excision of the left hindlimb, its embedding within agar, and scanning with the previously outlined DECT protocols.

3.2.6 Image Processing

To assess the homogeneity (*i.e.* uniform distribution of Er_2O_3 nanoparticles) of the cast Er-embedded resin filter we scanned the entire Er-filter at 90 kVp, 40 mA, 900 views, 0.4º increments over 360º, 16 ms exposure, and total scan time of 5 minutes. The resulting volume was rebinned 2 × 2 for a final resolution of 100 µm. The mean CT values from ten randomly placed 300 × 300 × 300 µm regions-of-interest (ROIs) (MicroView, v2.2.RC5, GE HealthCare, London, ON, CAN) throughout the scanned Er-filter were recorded and analyzed with a t-test, and significance was achieved if $p < 0.05$.

Decomposition of DECT images were performed *via* matrix factorization, as previously outlined by Granton *et al.*, 2008;[29] and a more detailed explanation can be found in Appendix C. However, briefly, the decomposition required six values, represented by the mean HU value of pure soft-tissue, bone, and vessel from both low- and high-energy scans. These values were obtained from 500 × 500 × 500 µm ROIs (MicroView) within the bicep femoris region (soft tissue), cortical bone (bone), and the femoral artery (vessel). The generated decomposed volumes represented quantitative maps of each individual component, with voxel values (0 – 10,000 arbitrary units) representing the volume fraction (0 – 100%, respectively) or the percent contribution of the decomposed material within each individual voxel; the remaining percentages were comprised of a mixture of the two remaining components. Note that using this approach, the volume fractions of the three basis function materials (*i.e.* soft tissue, bone, and vessel) are constrained to sum to 100%.

Quantitative evaluation on the accuracy of DECT decomposition accuracies was performed on the perfused 10 rats by quantifying the number and distribution of misclassified voxels within each decomposed volume (i.e. soft tissue, bone, and vessel). To quantify misclassified voxels, the coordinates of ROIs (500 × 500 × 500 µm, MicroView) within known areas of soft tissue (*i.e.* bicep femoris), bone (*i.e.* cortical bone), and vessel (*i.e.* femoral artery) were recorded. The three recorded ROIs were transposed within each decomposed volume of soft tissue, bone, and vessel. Mean values from each ROI within each decomposed component were recorded and averaged over the analyzed 10 samples. The sum of each tissue ROI across all decomposed volumes will

equal 10,000 arbitrary units or 100% (*e.g*. the sum of the mean values from femoral artery ROI transposed into the soft tissue, bone, and vessel decomposed volume will be 10,000 arbitrary units). Therefore, after normalizing the recorded values from all 10 samples, we can provide the percent of voxels that have been misclassified as another tissue.

All statistical analysis was performed using Prism (GraphPad, v7.03, La Jolla, CA, USA). A statistical significance was achieved if $p < 0.05$.

The use of 3D visualization software (VGStudio Max 2.0, Heidelberg, Germany) provided further visual enhancements, such as colorization and visual interactions between individual components.

3.3 Results and Discussion

3.3.1 DECT Design and Implementation on a Pre-Clinical Micro-CT Scanner

In this study, we have designed and implemented custom x-ray filtration, an automated filter-exchange mechanism, and fiducial marker-based image co-registration to successfully decompose – with high accuracy – DECT-acquired images from a pre-clinical gantry-based cone-beam micro-CT scanner.

Using simple silicone casting techniques, we created a silicone mold that facilitated the fabrication of an inexpensive and homogenous custom annular cylindrical Er-impregnated resin x-ray filter (Figure 2.2g). Excluding material costs for the production of the silicone mold (~$50 for the stock Al and silicone), the cost of materials to cast a single Er x-ray filter was ~$6, significantly cheaper than any Er-foil counterpart. The homogeneity test revealed a statistical significant, but vanishingly small (given the noise of ± 60 HU), difference of $p < 0.001$. However, the overall mean and standard deviation of 2753 ± 29 HU suggested a homogeneously cast Er x-ray filter.

The constructed motorized filter-exchange mechanism (Figure 3.3ac) successfully automated the acquisition of DECT images. This eliminated the need for operator-

dependent filter switches and possible operator errors (*i.e.* incorrect filter choice and inadvertent sample motion)

Easily segmented fiducial markers (Figure 3.3b) aided the semi-autonomous, sub-voxel image co-registration, where operator intervention was required only to choose a seed-point for the automated centroid calculation and co-registration. Together, the automated DECT acquisition and image co-registration provide a nearly automated work-flow for accurate DECT decompositions (as shown below).

3.3.2 DECT Results

The six values collected from ROIs of pure soft tissue, bone, and contrast-enhanced vessel are summarized in Table 3.1. Implementing the previously described matrix factorization,[5] these six values facilitated the DECT decomposition of an Er-perfused rat hindlimb into distinctly separate and quantitative 3D volumes of soft-tissue, bone (Figure 3.4c), and perfused vasculature (Figure 3.4d).

	Soft Tissue (HU)	**Bone (HU)**	**Contrast-Enhanced Vasculature (HU)**
Low Energy	37	2743	1659
High Energy	0	1909	2059

Table 3.1: Mean values from ROIs drawn within known pure regions of soft tissue, bone, and Er-perfused vasculature. The represented six numbers were chosen as input parameters for the automated decomposition algorithms.

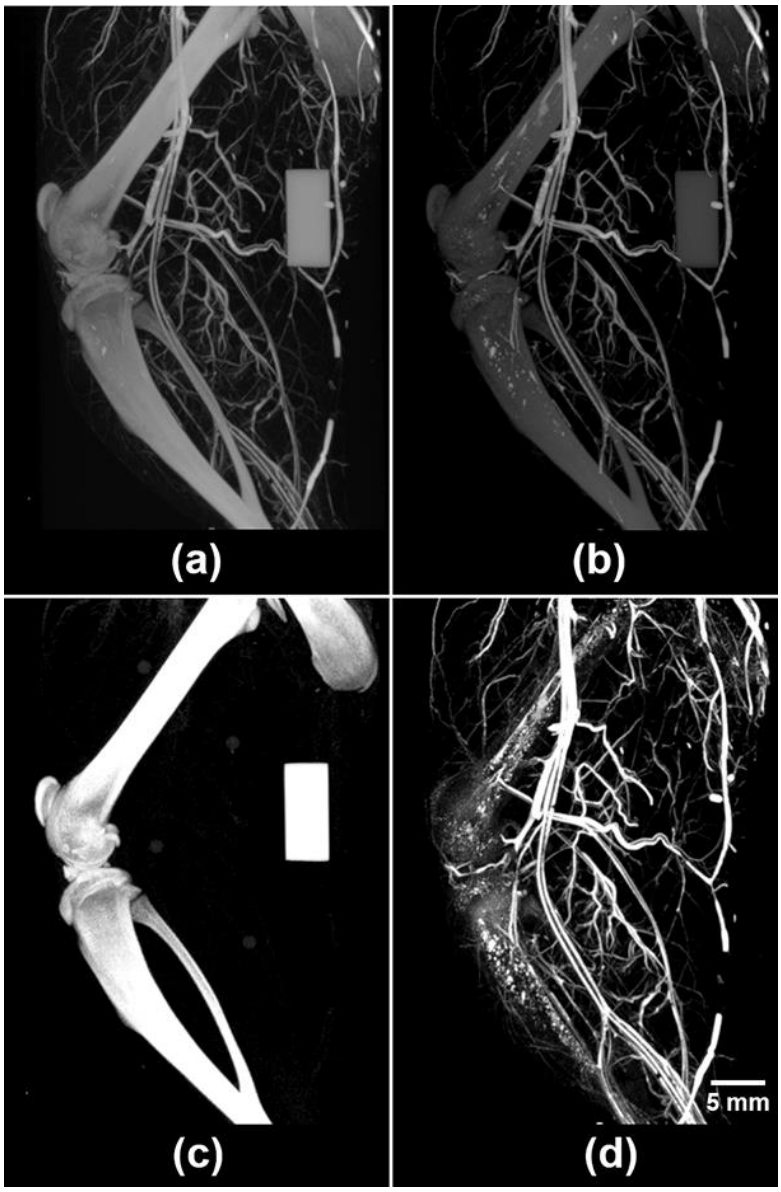

Figure 3.4: Dual-energy computed tomography (DECT) results of an Er-perfused rat hindlimb. Displayed are the low- and high-energy images acquired with the previously outlined DECT protocols and implemented automated filter-exchange mechanism and custom x-ray filtration. The acquired (**a**) low- and (**b**) high-energy images are decomposed automatically into their respective (**c**) bone- and (**d**) vessel-only components. The highly-accurate decomposition of bone and vessels facilitated the visualization of vessels within the cortical bone, in addition to the highly-vascularized sheets lining the outside and inside of each long bone, periosteum and endosteum, respectively. The ability to visualize these vessels manifests as femur- and tibia-like structures in the vessel-only image. Note the absence of the bone-mimicking calibrator from the vasculature image, emphasizing the success of the DECT decomposition.

The DECT decomposition yielded accuracies of 99.18%, 98.45%, and 99.78% in the soft tissue, bone, and vessel volumes, respectively (Table 3.2), as quantified from ten perfused rats. The visual representation of the amount and composition of misclassified voxels within each decomposed volume is illustrated within Figure 3.5.

		Known Pure Components		
		Soft Tissue (%)	**Bone (%)**	**Vessel (%)**
Decomposed Volumes	**Soft Tissue**	99.18 ± 0.44	0.26 ± 0.64	0.01 ± 0.03
	Bone	0.18 ± 0.10	98.45 ± 1.40	0.20 ± 0.38
	Vessel	0.66 ± 0.45	1.29 ± 1.03	99.78 ± 0.42

Table 3.2: DECT decomposition quantitative assessment. 500 × 500 × 500 µm ROIs were placed within known areas of soft tissue, bone, and vessels in each decomposed volume. The mean values of each ROI were recorded and normalized to 100 % within each individually decomposed volume.

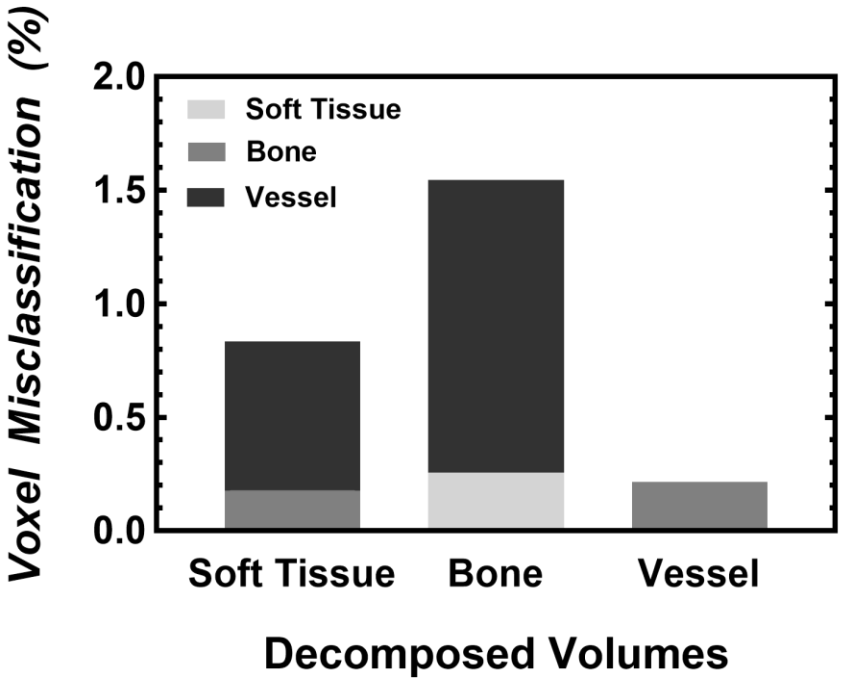

Figure 3.5: Graph depicting the percent of misclassified voxels after automatic DECT decomposition. Within each decomposed volume, misclassified voxels are comprised of the remaining two components.

Isolated visualization of the soft tissue, bone, and vessels is achieved *via* DECT decompositions. To image interactions between individual components, the decomposed data can be processed with 3D visualization software. In our case, the addition of colour to vessels (red) and bone (white) provided enhanced visualization to emphasize the vasculature surrounding and traversing within bone (Figure 3.6).

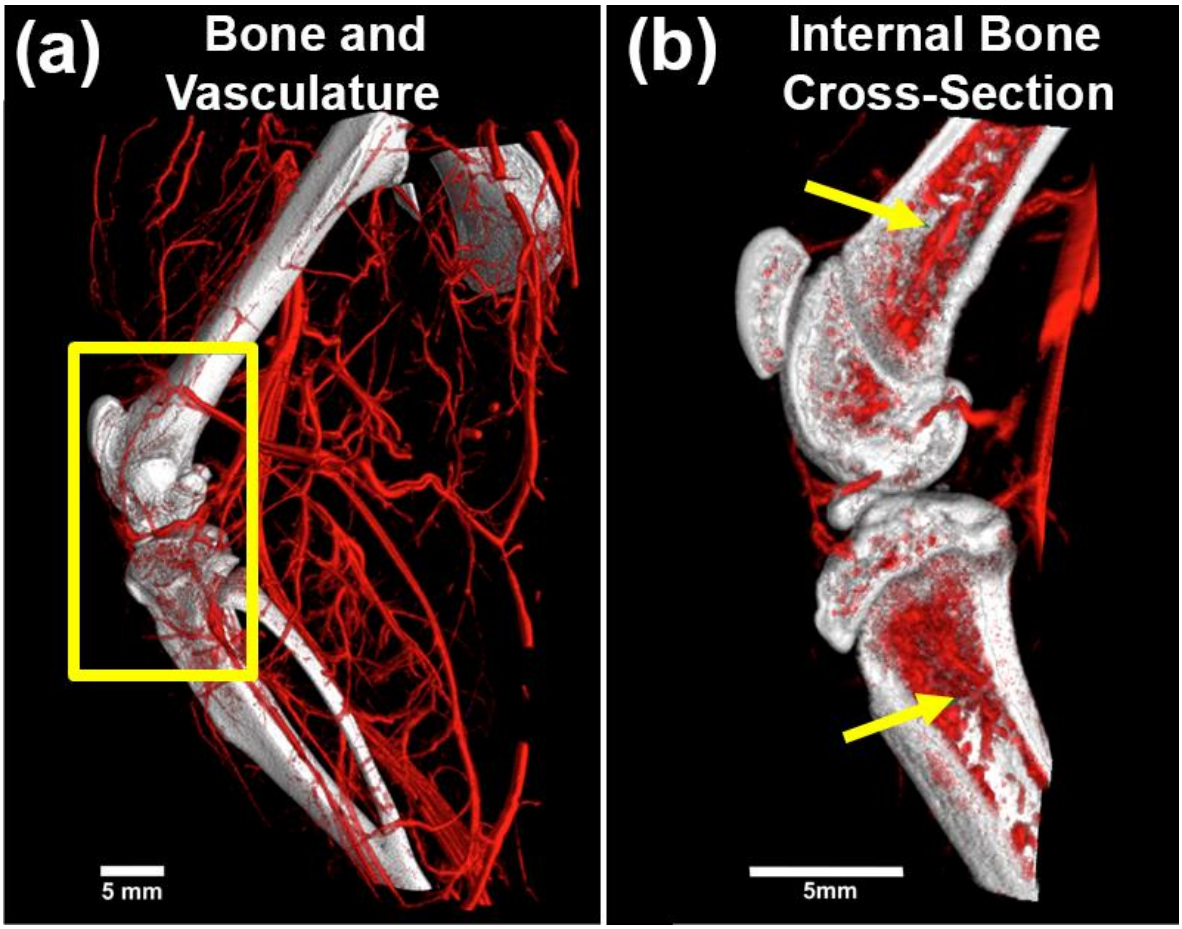

Figure 3.6: Dual-energy computed tomography (DECT) results after processed with 3D visualization software to emphasize the interactions between decomposed components – vessels (red) and bone (white). (**a**) Overall view of the vasculature outside and on the surface of the perfused rat hindlimb. (**b**) An internal cross-sectional view of the area outlined in yellow from (**a**). Note the highly vascularized internal nature of bone. Yellow arrows denote the primary nutrient vessels of the femur and tibia.

3.3.3 Importance of X-Ray Filtration and Image Co-Registration

Integration and implementation of multiple techniques (*i.e.* custom x-ray filtration, automated filter-exchange mechanism, fiducial markers, and image co-registration) are required for the optimal performance of DECT on pre-clinical gantry-based cone-beam micro-CT scanners. Any deficiency or absence in any of these techniques (*i.e.* spectral shaping and image co-registration) will result in non-ideal DECT decompositions. We demonstrated the importance of spectral shaping (*via* x-ray filtration) and image co-registration by performing the following experiments and data re-analysis.

Five Er-perfused rat hindlimbs were re-scanned (with the previously outlined DECT protocols) in the absence of customized x-ray filtration. The resulting sub-optimal spectral shaping and large spectral overlap are visualized in Figure 3.1 (top panel). Acquired low- and high-energy scans were co-registered and decomposed with a new set of six CT intensity values: low-energy soft tissue (45), bone (2930), vessel (2647), and high-energy soft tissue (45), bone (2572) and vessel (2768). The DECT decomposition resulted in a large number of misclassified voxels between decomposed volumes (Figure 3.7), visualized as “bleeding” between components. Visually, the perfused vasculature (Figure 3.7d) appears to have been decomposed properly; however, quantitative analysis revealed that only 76.23% of the vessels had been classified correctly (Table 3.3), with the majority misclassified as bone (Figure 3.7b). The remaining percentages (23.77%) and compositions of misclassified voxels are presented in Table 3.3 and visualized within Figure 3.8.

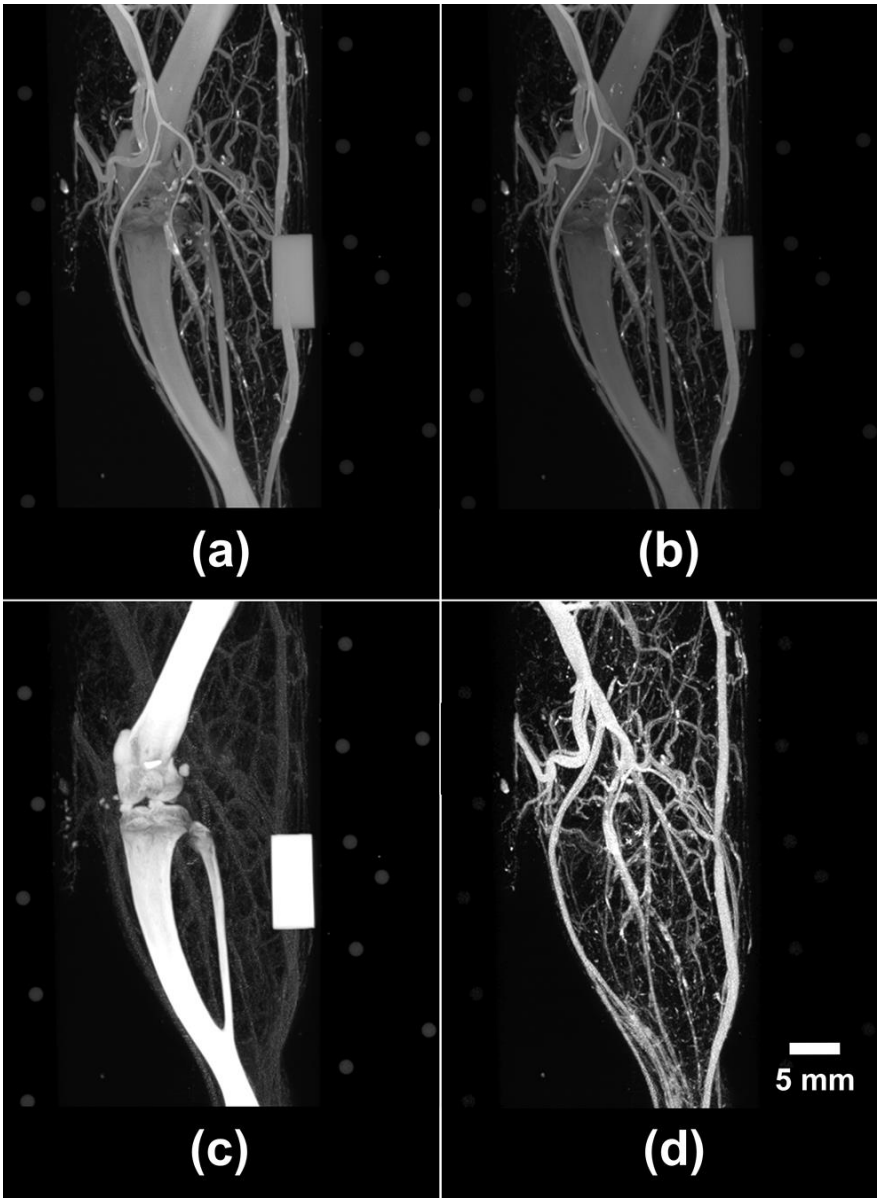

Figure 3.7: Dual-energy computed tomography (DECT) results of the Er-perfused rat hindlimb if no spectral shaping was implemented during the collection of the dual-energy images. Similar to results presented in **Figure 3.4**, DECT-acquired (**a**) low- and (**b**) high-energy images were acquired with the previously outlined DECT protocol, in the absence of the fabricated custom low- and high-energy x-ray filtration, co-registered images, and a separate set of six values (as without x-ray filtration, CT values of pure soft tissue, bone, and vessel will be different than in the presence of x-ray filtration) and were utilized for decomposition. Results of the decomposition are displayed in (**c**) bone- and (**d**) vessel-only image. Note the misclassified vessel voxels (*i.e.* "bleeding") within the bone image.

		Known Pure Components		
		Soft Tissue (%)	**Bone (%)**	**Vessel (%)**
Decomposed Volumes	**Soft Tissue**	97.33 ± 0.54	0.36 ± 0.42	6.79 ± 10.53
	Bone	2.08 ± 0.81	99.37± 0.59	16.96 ± 9.66
	Vessel	0.54 ± 0.61	0.27 ± 0.59	76.23 ± 12.61

Table 3.3: DECT decomposition quantitative assessment in the absence of proper x-ray filtration. 500 × 500 × 500 µm ROIs were placed within known areas of soft tissue, bone, and vessels in each decomposed volume. The mean values of each ROI were recorded and normalized to 100 % within each individually decomposed volume.

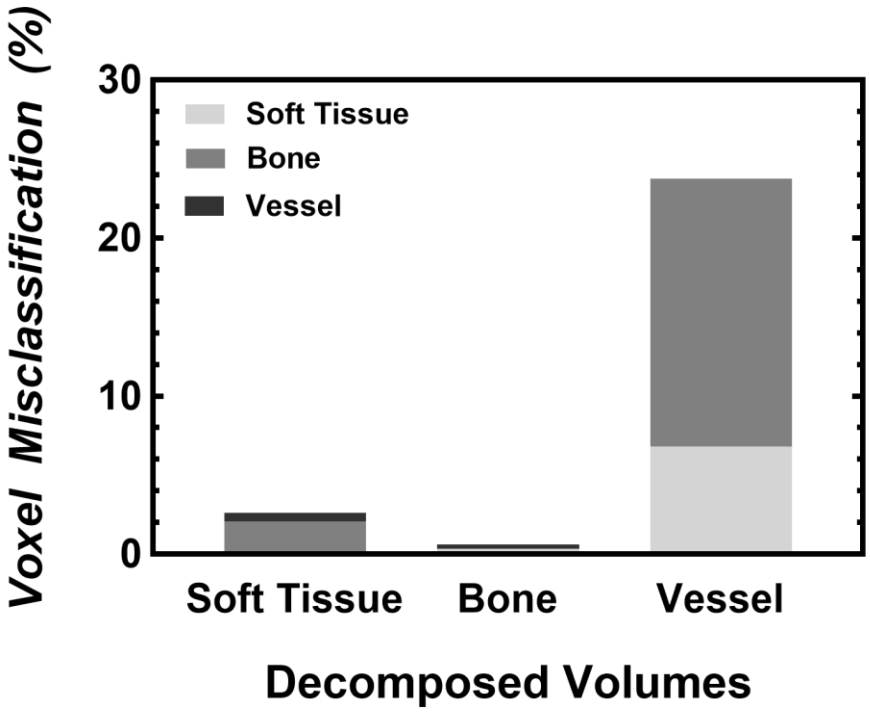

Figure 3.8: Graph depicting the percent of misclassified voxels, from **Table 3.3**, after automatic DECT decomposition. Within each decomposed volume, misclassified voxels are comprised of the remaining two components.

To establish the importance of image co-registration, data collected for Figure 3.4 was re-analyzed without co-registration prior to DECT decomposition. The decomposition results (Figure 3.9) appeared similar (*i.e.* misclassified voxels, “bleeding”) to those that have been acquired without proper spectral separation (Figure 3.7); however, the “bleeding” was more apparent across all decomposed volumes. Clearly, the sequentially acquired low- and high-energy volume images are not inherently co-registered at the sub-voxel level; this is likely due to a combination of small (and unavoidable) variations in positioning of the scanner bed and gantry between scans.

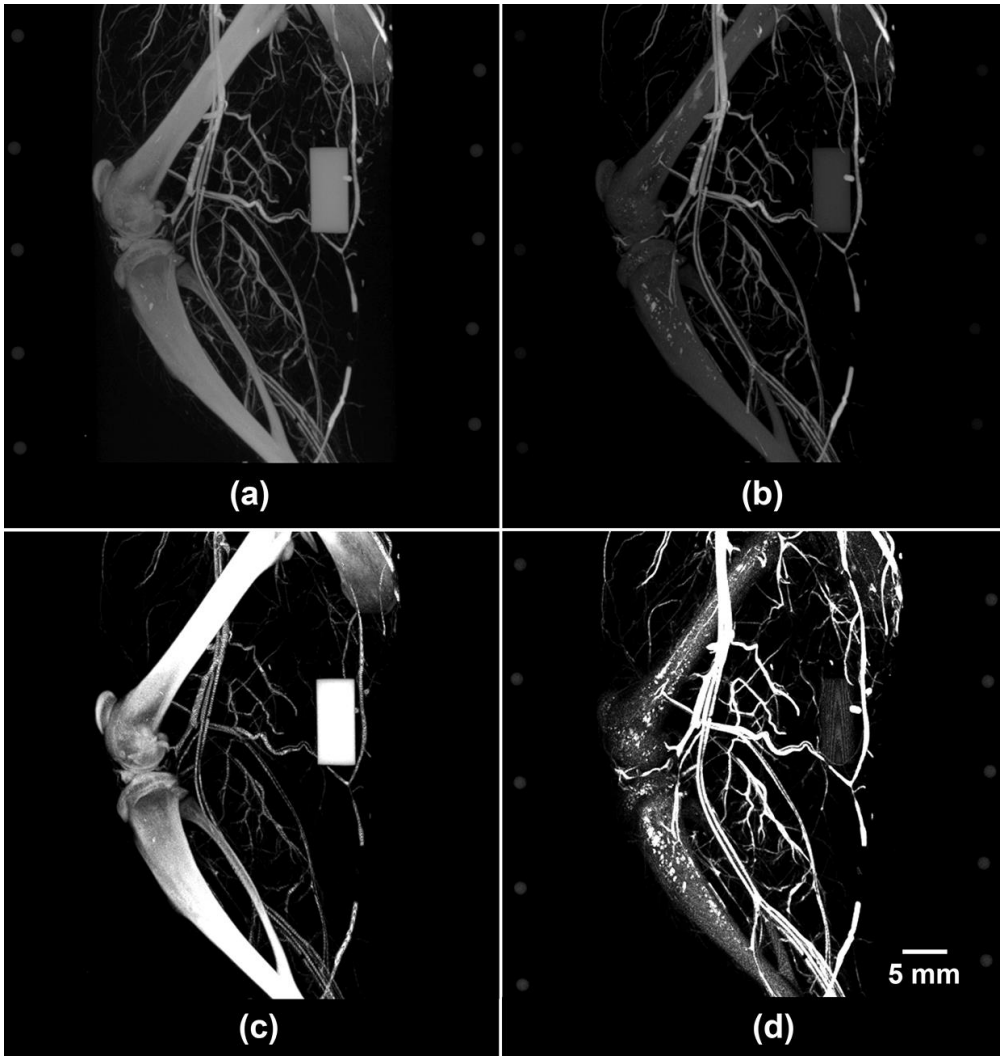

Figure 3.9: Dual-energy computed tomography (DECT) results of the same Er-perfused rat hindlimb if the low- and high-energy images were not co-registered prior to decomposition. Similar to results presented in **Figure 3.4**, DECT-acquired (**a**) low- and (**b**) high-energy images were acquired with the previously outlined DECT protocols and custom x-ray filtration; however, the fiducial markers (present on the periphery of each image) were not utilizes for image co-registration. Decomposition with these images resulted in the displayed (**c**) bone- and (**d**) vessel-only image. Mis-registration results in the misclassification of an objects' non-overlapping boundaries. As maximum intensity projections (MIP) are presented here, entire vessels and bone will appear to have been misclassified when this is in fact incorrect, and only the boundaries of these tissues have been misclassified. Note the large amount of "bleeding" of bone (and bone mimicking calibrator) within the vessel image, and *vice versa*.

Thus, it is apparent both visually (Figures 3.7 and 3.9) and quantitatively (Table 3.3) that both spectral separation and image co-registration are necessary for the proper collection and optimal decomposition of DECT-acquired images.

3.3.4 Limitations

While our work has overcome the challenges of spectral separation and image co-registration – required for the optimal implementation of DECT on pre-clinical cone-beam micro-CT scanners – several optimizations and limitations remain. The addition of our customized x-ray filtration resulted in > 98% decomposition (Table 3.2 and Figure 3.5). However, optimizations of the DECT acquisition process may be achieved with different filter concentrations. As an example, a reduction in x-ray filtration may yield similar decomposition results and the concurrent increase in CNR may allow for reduced scan times.

A limitation within our study is the limited performance of DECT to a single field-of-view (FOV), as the constructed automated filter-exchange mechanism can only actuate the filters between two hard-coded positions. However, modifications to the filter-exchange mechanism to actuate the sample holder or allow further travel distances of the x-ray filters would facilitate DECT of whole small animals.

An additional limitation is that our perfusion procedure precludes *in vivo* studies; however, there is currently research investigating an Er-based *in vivo* vascular perfusion contrast agent.[30] These future studies would also entail researching suitable DECT x-ray filtration compatible with the vascular contrast agent, in addition to balancing an acceptable x-ray dose for *in vivo* studies.

3.4 Conclusion

In this study, our implementation of DECT on a conventional pre-clinical laboratory cone-beam micro-CT scanner allowed for the automatic decomposition of Er-perfused rat hindlimbs into separate, distinct, and quantitative images of soft-tissue, bone, and perfused vasculature. This was achieved by sequential acquisition with two differential x-ray spectra, incorporating sub-voxel volumetric image co-registration between scans.

These scans were acquired with custom-fabricated x-ray filtration, an automated filter-exchange mechanism, and embedded fiducial markers that allowed for image co-registration using a rigid matrix transformation. The automated decomposition into specific tissue components was accurate to within 2%, facilitating quantitative analysis of specimen composition within 100 µm cubed voxels (*i.e.* 1 nL volume elements). The additional required hardware and software modifications did not interfere with the normal operation of a conventional commercial micro-CT scanner.

As part of this novel implementation of DECT, this study presented a methodology for the fabrication of custom x-ray filters, optimized for the spectral shaping associated with an Er-based contrast agent. In the future, this fabrication technique can be modified to create user-specified custom (*i.e.* shape, elemental composition, and concentration) resin-embedded x-ray filters of any element present in nanoparticulate powders. This range of customization would facilitate the application of DECT to take advantage of other exogenous contrast agents, or endogenous contrast within the specimen.

The methodology presented here will have applications in a range of biomedical research, including the study of cardiovascular disease, respiratory conditions, cancer, and osteoarthritis. Our approach for optimal spectral shaping using customized filters is also applicable in non-biomedical research, including earth-science applications (*e.g.* geological specimens and meteorite analysis), archaeological studies, and non-destructive testing of 3D-printed objects. Additionally, the techniques that we have described within our study are applicable to a large installed base of micro-CT scanning systems, as well as conventional multi-slice CT scanners for research applications.

3.5 References

1. R. A. Rutherford, B. R. Pullan, I. Isherwood, Measurement of effective atomic number and electron density using an EMI scanner. *Neuroradiology* **11**, 15-21 (1976).

2. E. L. Ritman, Micro-computed tomography-current status and developments. *Annu Rev Biomed Eng* **6**, 185-208 (2004).

3. R. Mizutani, Y. Suzuki, X-ray microtomography in biology. *Micron* **43**, 104-115 (2012).

4. E. Descamps, A. Sochacka, B. De Kegel, D. Van Loo, L. Van Hoorebeke, D. Adriaens, Soft tissue discrimination with contrast agents using micro-CT scanning. *Belg J Zool* **144**, 20-40 (2014).

5. P. V. Granton, S. I. Pollmann, N. L. Ford, M. Drangova, D. W. Holdsworth, Implementation of dual- and triple-energy cone-beam micro-CT for postreconstruction material decomposition. *Med Phys* **35**, 5030-5042 (2008).

6. A. Lerman, E. Ritman, Evaluation of microvascular anatomy by micro-CT. *Herz* **24**, 531-533 (1999).

7. S. Achenbach, J.-F. Paul, F. Laurent, H.-C. Becker, M. Rengo, J. Caudron, S. Leschka, O. Vignaux, G. Knobloch, G. Benea, T. Schlosser, J. Andreu, B. Cabeza, A. Jacquier, M. Souto, D. Revel, S. D. Qanadli, F. Cademartiri, X. A. C. T. S. G. on behalf of the, Comparative assessment of image quality for coronary CT angiography with iobitridol and two contrast agents with higher iodine concentrations: iopromide and iomeprol. A multicentre randomized double-blind trial. *European Radiology* **27**, 821-830 (2017).

8. M. Kayan, H. Demirtas, Y. Türker, F. Kayan, G. Çetinkaya, M. Kara, A. Orhan Çelik, A. Umul, Ö. Yılmaz, A. Recep Aktaş, Carotid and cerebral CT angiography using low volume of iodinated contrast material and low tube voltage. *Diagnostic and Interventional Imaging* **97**, 1173-1179 (2016).

9. D. Andreini, S. Mushtaq, E. Conte, C. Segurini, M. Guglielmo, M. Petullà, V. Volpato, A. Annoni, A. Baggiano, A. Formenti, A. L. Bartorelli, C. Fiorentini, M. Pepi, Coronary CT angiography with 80 kV tube voltage and low iodine concentration contrast agent in patients with low body weight. *Journal of Cardiovascular Computed Tomography* **10**, 322-326 (2016).

10. L. R. Long, G. R. Thoma. (1999), vol. 3661, pp. 1037-1046.

11. P. Blery, P. Pilet, A. V. Bossche, A. Thery, J. Guicheux, Y. Amouriq, F. Espitalier, N. Mathieu, P. Weiss, Vascular imaging with contrast agent in hard and soft tissues using microcomputed-tomography. *Journal of Microscopy* **262**, 40-49 (2016).

12. M. Ding, C. C. Danielsen, I. Hvid, S. Overgaard, Three-dimensional microarchitecture of adolescent cancellous bone. *Bone* **51**, 953-960 (2012).

13. K. Matsui, H. Machida, T. Mitsuhashi, H. Omori, T. Nakaoka, H. Sakura, E. Ueno, Analysis of coronary arterial calcification components with coronary CT angiography using single-source dual-energy CT with fast tube voltage switching. *The International Journal of Cardiovascular Imaging* **31**, 639-647 (2015).

14. R. Salvador, M. P. Luque, A. Ciudin, B. Pano, L. Bunesch, C. Sebastia, C. Nicolau, Usefulness of dual-energy computed tomography with and without

dedicated software in identifying uric acid kidney stones. *Radiologia* **58**, 120-128 (2016).

15. R. K. Kaza, J. F. Platt, R. H. Cohan, E. M. Caoili, M. M. Al-Hawary, A. Wasnik, Dual-Energy CT with Single- and Dual-Source Scanners: Current Applications in Evaluating the Genitourinary Tract. *RadioGraphics* **32**, 353-369 (2012).

16. A. So, T.-Y. Lee, in *Dual-Energy CT in Cardiovascular Imaging*, P. M. Carrascosa, R. C. Cury, M. J. García, J. A. Leipsic, Eds. (Springer International Publishing, Cham, 2015), pp. 45-60.

17. T. R. C. Johnson, Dual-Energy CT: General Principles. *American Journal of Roentgenology* **199**, S3-S8 (2012).

18. A. N. Primak, J. C. Ramirez Giraldo, X. Liu, L. Yu, C. H. McCollough, Improved dual-energy material discrimination for dual-source CT by means of additional spectral filtration. *Medical Physics* **36**, 1359-1369 (2009).

19. M. Qu, J. C. Ramirez Giraldo, S. Leng, J. C. Williams, T. J. Vrtiska, J. C. Lieske, C. H. McCollough, Dual-energy dual-source CT with additional spectral filtration can improve the differentiation of non-uric acid renal stones: An ex vivo phantom study. *AJR Am J Roentgenol* **196**, 1279-1287 (2011).

20. B. Krauss, K. L. Grant, B. T. Schmidt, T. G. Flohr, The importance of spectral separation: an assessment of dual-energy spectral separation for quantitative ability and dose efficiency. *Invest Radiol* **50**, 114-118 (2015).

21. F. Kelcz, P. M. Joseph, S. K. Hilal, Noise considerations in dual energy CT scanning. *Med Phys* **6**, 418-425 (1979).

22. J. J. Tse, J. Dunmore-Buyze, M. Drangova, D. W. Holdsworth, Erbium-based perfusion contrast agent for small-animal microvessel imaging. *Contrast Media & Molecular Imaging*, In Press (2017).

23. J. H. Siewerdsen, A. M. Waese, D. J. Moseley, S. Richard, D. A. Jaffray, Spektr: A computational tool for x-ray spectral analysis and imaging system optimization. *Medical Physics* **31**, 3057-3067 (2004).

24. M. R. Ay, A. Mehranian, A. Maleki, H. Ghadiri, P. Ghafarian, H. Zaidi, Experimental assessment of the influence of beam hardening filters on image quality and patient dose in volumetric 64-slice X-ray CT scanners. *Physica Medica* **29**, 249-260 (2013).

25. P. Brosi, A. Stuessi, F. R. Verdun, P. Vock, R. Wolf, Copper filtration in pediatric digital X-ray imaging: its impact on image quality and dose. *Radiological Physics and Technology* **4**, 148-155 (2011).

26. H. Kawashima, K. Ichikawa, D. Nagasou, M. Hattori, X-ray dose reduction using additional copper filtration for abdominal digital radiography: Evaluation using signal difference-to-noise ratio. *Physica Medica* **34**, 65-71 (2017).

27. M. M. Travieso Aja, M. Rodríguez Rodríguez, S. Alayón Hernández, V. Vega Benítez, O. P. Luzardo, Dual-energy contrast-enhanced mammography. *Radiología (English Edition)* **56**, 390-399 (2014).

28. K. S. Arun, T. S. Huang, S. D. Blostein, Least-Squares Fitting of Two 3-D Point Sets. *IEEE Transactions on Pattern Analysis and Machine Intelligence* **PAMI-9**, 698-700 (1987).

29. H. J. Vinegar, S. L. Wellington, Tomographic imaging of three-phase flow experiments. *Review of Scientific Instruments* **58**, 96 (1987).

30. C. Cruje, J. J. Tse, D. W. Holdsworth, E. R. Gillies, M. Drangova, in *SPIE Medical Imaging*. (SPIE, 2017), vol. 10132, pp. 6.

Chapter 4

4 Studying Femoral- and Tibial-Subchondral Bone and Vascular Changes Using Dual-Energy Micro-Computed Tomography in a Surgically-Induced Rat Hindlimb Model of Osteoarthritis

4.1 Introduction

Osteoarthritis, OA, is a chronic debilitating joint disease that affects millions of individuals.[1-3] This joint disease affects multiple joints (*e.g.*. hand,[4] hip,[5] knee,[6] and spine[7]) and is the result of cartilage and bone degeneration, presenting symptomatically as joint stiffening and pain. Presently, no drugs or treatments can halt or reverse the bone and cartilage degeneration resulting from the progression of OA.[8] The absence of effective OA-treatments are attributed to OA's complex and multifactorial nature; factors such as age,[9,10] pre-existing injuries,[11-13] diabetes,[14-16] and genetic predisposition[17,18] have all been shown to contribute to the development of OA. One interesting hypothesis – and of increasing interest – revolves around the role of microvessels within subchondral bone of affected joints.[19-24]

Microvessels are essential for the healthy maintenance of joint-associated bone and cartilage; these vessels facilitate the transportation of nutrients, oxygen, and inflammatory molecules to the joint, in addition to removal of cellular waste products.[25-27] Cartilage is an avascular tissue (*i.e.* does not contain any blood vessels); thus, all of its resources must be provided by the highly-vascularized neighboring synovium[28] and subchondral bone.[29,30] With cartilage's vital dependency on neighbouring tissues for its healthy maintenance, it has been hypothesized[19,21,31] that OA may stem from changes to the delicate microvascular homeostasis of naïve joints, negatively impacting the development and physiology of the local bone and cartilage environment. A decrease in blood vessel density or competency may result in diminished oxygen and nutrient supply to the joint, and a buildup of waste products. Combined, these effects may trigger an inflammatory response from the synovium or subchondral bone and cause cartilage degeneration.[19,20,32] Alternatively, an increase in blood vessel density may prompt

angiogenic factors to initiate the vascular invasion of cartilage – an otherwise avascular environment – triggering its self-degradation.[33,34] While the microvessels encapsulating the synovial joint are known to be responsible for the majority of cartilage's nutrients and oxygen,[28] there has been increasing interest in the role of subchondral bone microvessels in the maintenance[29] and degeneration[20] of cartilage. Of particular interest are the distal femoral epiphysis and proximal tibial epiphysis, due to their proximity to the cartilaginous surfaces of the joint. Thus, simultaneously studying changes in subchondral bone and microvessel densities throughout the course of OA may provide insight into whether a decrease or increase in microvessels is associated with OA.

The quantitative pre-clinical study and characterization of blood vessels within intact bone has proven challenging due to difficulties in imaging microvessels. Three properties of microvessels have impeded the simple segmentation of vessels from surrounding bone: (1) their small size (*i.e.* < 10 μm, capillaries); (2) lack of inherent contrast against surrounding tissue; and (3) proximity to dense bony structures. Currently, histology remains the gold standard for the study of microvessels; unfortunately, histology of joints requires the decalcification of bone prior to histological sectioning, an inherently destructive process, resulting in the loss of bone information. Alternatively, micro-CT is routinely used for the non-destructive imaging of bone;[35] however, visualization of blood vessels requires the addition of an exogenous contrast agent.

In Chapters 2 and 3, we characterized a highly x-ray attenuating Er-based micro-CT *ex vivo* vascular perfusion contrast agent[36] and its combination with optimized dual-energy computed tomography (DECT) on a pre-clinical, gantry-based, cone-beam micro-CT scanner,[37] respectively. Our proposed technique facilitated the automated acquisition of DECT volume images of Er-perfused samples and the subsequent volume-image decomposition, resulting in individually-segmented, co-registered, quantitative volumes of soft tissue, subchondral bone and microvessel density.[37] Implementing this previously described technique with an animal model of OA will allow for the simultaneous study of OA-associated microvessel and subchondral bone changes.

Previous research in rats has shown that the combination of an anterior cruciate ligament transection (ACLX) and partial medial meniscectomy (PMM) to cause joint instability, bone-on-bone grinding during joint loading, and the eventual cartilage loss associated with OA.[38-40] Additionally, ACLX + PMM mimics the subtle and early subchondral bone changes observed within human pathogenesis of OA.[38] Therefore, in this study, we utilize the techniques developed in Chapters 2 and 3 to quantify the subchondral bone and microvessel density changes within the distal femoral epiphysis and proximal tibial epiphysis of rats that have undergone the ACLX + PMM OA-inducing surgery. Our experimental design extended prior-to and 8-weeks post-operatively, allowing for the simultaneous visualization, characterization, and quantification of subchondral bone and microvessels throughout the initiation and progression of OA.

4.2 Materials and Methods

4.2.1 Animal Model

All animal manipulations in the following study were approved by the Animal Use Subcommittee of Western University (protocol #2015-018). Sprague-Dawley rats (N = 54, Harlan Laboratories, IN, USA) of 300 - 325g (~3 months of age) were used throughout the experiment. Six rats were perfused (as described below) for the 0-week controls, the remaining N = 48 were divided in half for the ACLX + PMM and sham surgery groups. Within each surgery group, animals were further sub-divided (N = 6) for each experimental time point: T = 0 (pre-operative), 1, 2, 4, and 8 weeks post-operatively. Previous work with this animal model of OA encompassed the 2, 4, and 8 weeks post-operatively timepoints; however, we included a 1-week post-operative timepoint as we were interested in observing possible early changes to the soft tissue, bone, and microvessels. Animals were monitored daily and weighed prior to surgery and perfusion. All animals were housed in standard cages and permitted free activity with food and water provided *ad libitum*.

4.2.1.1 Sham and OA-Induced Surgeries

Prior to surgery, animals were anesthetized and maintained with 4% isoflurane (Baxter, ON, CAN) and 2 ml/min O_2. All surgeries were performed solely on the right hindlimb

(ipsilateral), allowing the left (contralateral) hindlimb to serve as an internal control. For both OA-induced and sham surgeries, a parapatellar incision was made on the medial aspect of the joint, anterior to the medial collateral ligament. Rats that underwent the OA-induced surgery had the anterior cruciate ligament transected (ACLX) and a portion of the medial meniscus removed (PMM). Both sham and ACLX + PMM surgeries had the incisions closed in two layers with interrupted sutures using absorbable 5-0 Vicryl sutures (Ethicon, Johnson & Johnson Medical Products, ON, CAN), and the skin was closed with subcuticular sutures using 4-0 Vicryl (Ethicon, Johnson & Johnson Medical Products, ON, CAN).

All animals were given antibiotics and analgesics pre- and post-operatively. Antibiotics (17.8 mg/kg Ampicillin, Novopharm®, ON, CAN) were administered intramuscularly. In compliance with standard operating protocols set by the Animal Care and Use Committee at Western University, the analgesic buprenorphine (0.05 mg/kg, Vetergesic Multidose, Champion Alstoe Animal Health, ON, CAN) was administered subcutaneously every ~10 hours over 48 hrs post-operatively.

4.2.2 Er-Based Contrast Agent and Curing Agent Preparation

Preparation of the Er-based suspension has been previously outlined in Chapter 2.[36] Briefly, perfusion required the combination of two components: an Er-based suspension and a curing agent.

The Er-based vascular contrast agent (described in Chapter 2) is comprised of erbium oxide nanoparticles (Er_2O_3 NPs, Nanostructured and Amorphous Materials, TX, USA) suspended within a two-part clear silicone elastomer (Microfil MV-132, FlowTech Inc., MA, USA). The Er-based contrast agent was prepared in 30 mL batches, a sufficient volume for rat hindlimb perfusions. The Er-suspension was comprised of 4.0 g of mortar and pestle ground uncoated Er_2O_3 NPs mixed into MV-Diluent (17.47 mL) and MV-132 (8.73 mL) in a 2:1, respectively. The remaining 3.8 mL was comprised of the homemade curing agent, as described below, added immediately prior to perfusion. To ensure the homogeneous distribution of Er_2O_3 NPs within the silicone elastomer, the suspension was probe sonicated (Branson Digital Sonifier 450D with 13 mm tapped horn, Crystal

Electronics, ON, CAN) for a total of 35 minutes with 25% amplitude and a duty cycle of 30 s ON followed by 10 s OFF. The contrast agent was prepared at least an hour in advance and decanted just prior to use, to remove the larger settled aggregates.

To ensure the consistent curing of our Er-based suspension, the curing agent was made in-house and was comprised of 40% (w/w) dibutyltin dilaurate (Sigma Aldrich, MI, USA) and 60% (w/w) tetraethyl orthosilicate (Sigma Aldrich, MI, USA) mixed with a magnetic stirrer until a homogeneous transparent pale-yellow mixture was achieved.

4.2.3 Animal Perfusion

The perfusion of animals and fabrication of a custom catheter have been previously described in Chapter 3.[37] In brief, at the time of perfusion, animals were weighed, anesthetized and maintained on 4% isoflurane (Baxter, ON, CAN) with 2 mL/min O_2. A jugular injection of heparin (500 µL, Sandoz, QC, CAN) was administered to prevent blood clotting. Heparin circulated for 5 minutes prior to making a midline incision to expose the abdominal organs. The organs were displaced to clearly reveal the aorta and inferior vena cava (IVC). Gauze was then used to carefully separate the membrane covering the aorta and IVC. Two lengths of braided silk thread (~ 10 cm, Ethicon, Johnson & Johnson Medical Products, ON, CAN) were passed between the aorta and IVC. One length of thread was used to tie off the aorta, below the renal arteries. Fine-tipped forceps were inserted into a cut made perpendicular to the aorta; spreading the forceps allowed the insertion of the custom catheter. The catheter tip, maneuvered until ~1-2 cm upstream of the aortic bifurcation, was held securely in place with the tied-off second length of thread. The IVC was cut to allow for circulatory drainage, as the animal was exsanguinated with ~ 250 mL of 2% heparinized saline prior to perfusion of the Er-based vascular contrast agent.

Just prior to contrast agent perfusion, 3.8 mL of the homemade curing agent was added to the Er-based suspension and vortexed (VWR® Fixed Speed Vortex Mixer, PA, USA) continuously for 8 minutes. The entire mixture was injected into an empty saline bag and hung 175 cm above the animal, providing an equivalent pressure of 129 mmHg. The

contrast agent was perfused until cured, ~ 37 minutes post-addition of curing agent. The rat hindlimb region was fixed in 10% formalin for at least 2 weeks prior to DECT scans.

Following fixation, hindlimbs were dislocated at the femoral head, excised, and placed within 50 mL tubes with 10% formalin. After another week in formalin (to ensure complete fixation throughout the entire hindlimb), samples were stored in 70% ethanol until DECT-scanned.

4.2.4 Dual-Energy Micro-CT Scanning

Details regarding the entire dual-energy micro-CT (DECT) procedure (*i.e.* acquisition, image co-registration, and image analysis) have been previously described in Chapter 3.[37] Briefly, post-mortem DECT was performed on a pre-clinical, gantry-based, cone-beam, micro-CT scanner (GE eXplore Vision120, GE HealthCare, ON, CAN). High-energy scans were acquired at 90 kVp, 40 mA, with an additional annular cylindrical Cu x-ray filter of total pathlength 0.48 mm. Low-energy scans were collected at 70 kVp, 50 mA, using a custom fabricated Er-embedded resin x-ray filter with effective pathlength of 0.064 mm. Each energy scan was collected over 1200 projections, at 0.3° increments over 360°, 16 ms per view acquisition time, and an average of 10 acquisitions per view projection. Scan time at each energy was ~ 1. 5 hrs; thus, the total time required for a DECT scan of a single sample was approximately 3 hrs. All data were collected with an isotropic voxel spacing of 50 × 50 × 50 µm and subsequently rebinned 2 × 2, resulting in full three-dimensional (3D) micro-CT volumes of 100 × 100 × 100 µm isotropic voxel spacing. The reconstructed micro-CT volumes were calibrated into Hounsfield (HU) units wherein the CT value of an embedded water and air calibrator set to 0 and -1000 HU, respectively.

Fiducial marker beads (Teflon®, polytetrafluoroethylene (PTFE), Product Components Corporation, Martinez, CA, USA) within the sample holder were used to achieve sub-voxel image co-registration between the high- and low-energy acquired micro-CT volumes. Decomposition of the DECT-acquired images was performed through matrix factorization,[41] and resulted in individually segmented and quantitative volumes of soft tissue, bone, and vessel. Within each decomposed volume, signal intensity values were

scaled such that integer grey-scale voxel values (0 – 10,000) represented the voxel volume fraction (0 – 100%) of the respective component.

4.2.4.1 Partial Volume Effect (PVE)

Distinguishing between individual microvessels (*i.e.* capillaries, < 10 μm) is not possible with DECT-acquired images with (100 μm)^3 voxels due to partial volume effects (PVE). However, previous research[42-44] has suggested that DECT may be partially resistant to PVE, as DECT may still allow for the accurate detection and quantification of microvessel densities over varying spatial resolutions. To quantitatively evaluate PVE on DECT decompositions, we compared the same volume-of-interest (VOI) among five rat hindlimbs that were DECT scanned with 33 μm isotropic voxel spacing and subsequently rebinned 2 × 2, 3 × 3, and 4 × 4, resulting in isotropic voxel spacings of 66, 99, and 132 μm, respectively.

For this study of partial volume effects, DECT scans were acquired on a rotating-stage specimen scanner (GE Locus SP, GE Healthcare, London, ON, CAN). The high-energy image was acquired at 90 kVp, 90 μA, and with additional filtration of 0.254 mm Cu and 0.254 mm Al. The low-energy scans were performed at 64 kVp, 125 μA, and an additional 0.075 mm Er-foil x-ray filter. Both x-ray energy scans were collected over 720 projections, at 0.5º increments over 360º, 1600 ms exposure time per view, and an average of 20 views per projection. Images were reconstructed with isotropic voxel spacing of 33 × 33 × 33 μm subsequently rebinned to 66, 99, and 132 μm (as previously stated). Individual energy scans were approximately 8 hr each, totaling ~ 16 hrs for a DECT scan of a single sample. Reconstructed volumes were calibrated into HU units using embedded air and water calibrators prior to DECT decomposition.

4.2.5 Data Analysis

4.2.5.1 DECT and PVE Analysis

Studying the subchondral bone and microvessel density within the distal femoral epiphysis and proximal tibial epiphysis required the generation of custom volumes-of-interest (VOI). Within each high-energy volume, 2D contours were generated by an operator (MicroView v2.12, GE HealthCare, ON, CAN) by following the cortical shell

and growth plate (Figure 4.1A). This contouring process was repeated every 200 μm, until the entire joint had been encompassed. Interpolation between the individual 2D contours resulted in a 3D VOI (Figure 4.1B). The derived VOI was transposed within each inherently co-registered decomposed volume (soft tissue, bone, and vessel, Figure 4.1C and D), and mean values were recorded from both the operated and non-operated hindlimbs from all N = 54 rats.

Previous research[45] has demonstrated that inter-animal variability can be a confounding factor when analyzing statistical vascular differences between animals of differing surgery groups and timepoints. To overcome the challenge of inter-animal variability, at each timepoint the voxel volume fraction results of soft tissue, subchondral bone, and vascular density measurements have been presented as a comparison between the ipsilateral (operated) and respective contralateral (non-operated, *i.e.* control) hindlimbs. Using the mean value acquired from a 500 × 500 × 500 μm ROI within the femoral artery, a paired t-test was performed to ensure the non-significant differences in contrast enhancement between the ipsilateral and contralateral hindlimbs of each rat. Using the same data, a linear regression analysis was performed to examine whether consistent contrast enhancement was achieved across the entire 8 – week post-operative timeframe. This evaluation of contrast enhancement within a large feeding vessel was performed as part of routine quality assurance, to verify that the perfusion and scanning procedure was stable over the course of the study.

To evaluate the effects of PVE on DECT, the voxel volume fractions of identical VOIs (as described above) were compared across varying voxel spacings (*i.e.* 33, 66, 99, and 132 μm). The same six CT numbers required for DECT decomposition (*i.e.* mean values of soft tissue, bone, and vessel at both low- and high-energy) were used for each rebinned volume. To ensure that the same custom VOI, generated from the 33 μm native resolution volume, was applied to each subsequent rebinned volume, interpolation of all rebinned volumes to the native isotropic voxel spacing of 33 μm was performed. The mean values of custom VOIs transposed within bone- and vessel-only DECT decomposed images were collected from three rat hindlimbs, normalized, and analyzed within Prism (Graphpad v7.03, La Jolla, CA, USA).

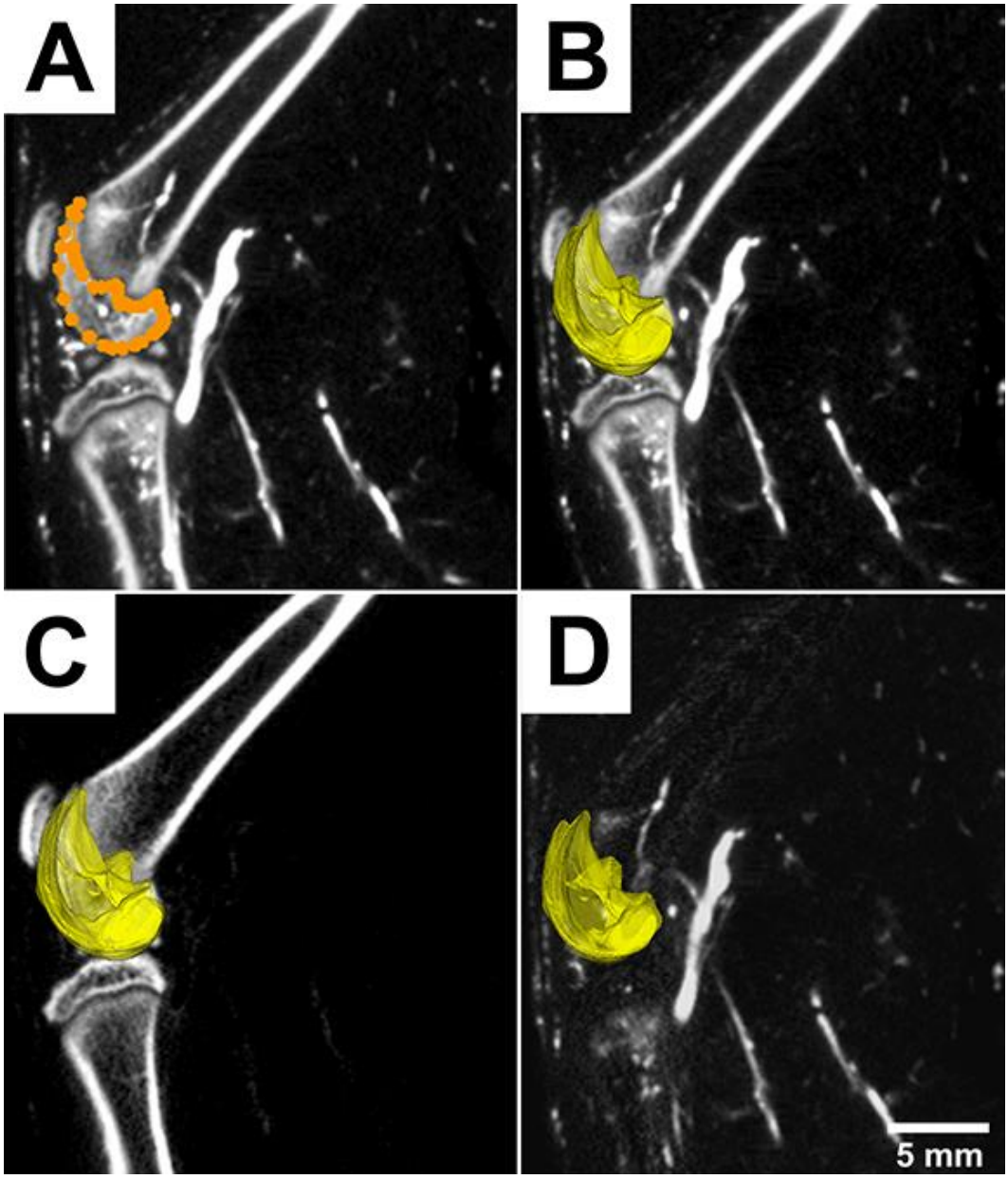

Figure 4.1: Multi-planar reformatted images of a DECT-scanned perfused rat hindlimb. (**A**) Two-dimensional (2D) contour around the distal femoral epiphysis, drawn within the DECT-acquired high-energy x-ray image. (**B**) 3D volume-of-interest (VOI) generated from the extrapolation of 2D contours drawn manually every 200 µm throughout the joint. The 3D VOI was then transposed within the co-registered, DECT-decomposed (**C**) bone-only and (**D**) vessel-only volumes. Mean values within each 3D VOI were collected and recorded.

4.2.5.2 Histological Analysis

The investigation of OA-related physiological markers (*i.e.* lesions, and cartilage loss) was performed through the histological examination of two perfused rat knee joints. To prepare samples for histological analysis, perfused hindlimbs were first decalcified prior to serial sectioning and staining.

The process of rat hindlimb decalcification encompassed a 5-day long procedure. On day 1, soft tissue and muscle surrounding the knee joint were trimmed and removed (with care taken near the joint capsule) to aid penetration of the decalcification solution. Trimmed hindlimbs were submerged within ~35 mL of decalcifying solution (Formical-2000, Fisher Scientific, NH, USA) and placed on a rocking platform overnight. On day 2, tissue and bone were further trimmed to within ~ 1 –2 cm above and below the joint capsule. Samples were placed back in the same decalcification solution and rocked overnight. On day 3, joints were bisected along the medial aspect of the tibia. To facilitate the bisection and provide clean, straight, and consistent cuts, a custom easy-to-use guillotine (Figure 4.2) was constructed. Bisected sections were submerged within fresh ~35 mL decalcification solution and rocked for a day (*i.e.* day 4). On day 5, samples were rinsed twice in distilled water for 5 minutes each and stored within 70% ethanol at 4^{o} C until histological processing.

Decalcified and bisected joints were dehydrated through a series of increasing alcohol concentrations, in preparation for paraffin embedding. Histological sectioning of embedded samples involved the collection of five 6 µm serial sections followed by a 100 µm tissue trim, until a total of ~ 120 µm of tissue had been accumulated. Selected sections were stained with Toluidine blue to assess the presence of OA. Toluidine blue preferentially stains proteoglycans and glycosaminoglycans (*i.e.* major components of cartilage), and the intensity of the Toluidine blue staining reflects cartilage health (*i.e.* weak Toluidine blue stains implies reduced proteoglycans and glycosaminoglycans or degraded cartilage health and *vice versa*).[46]

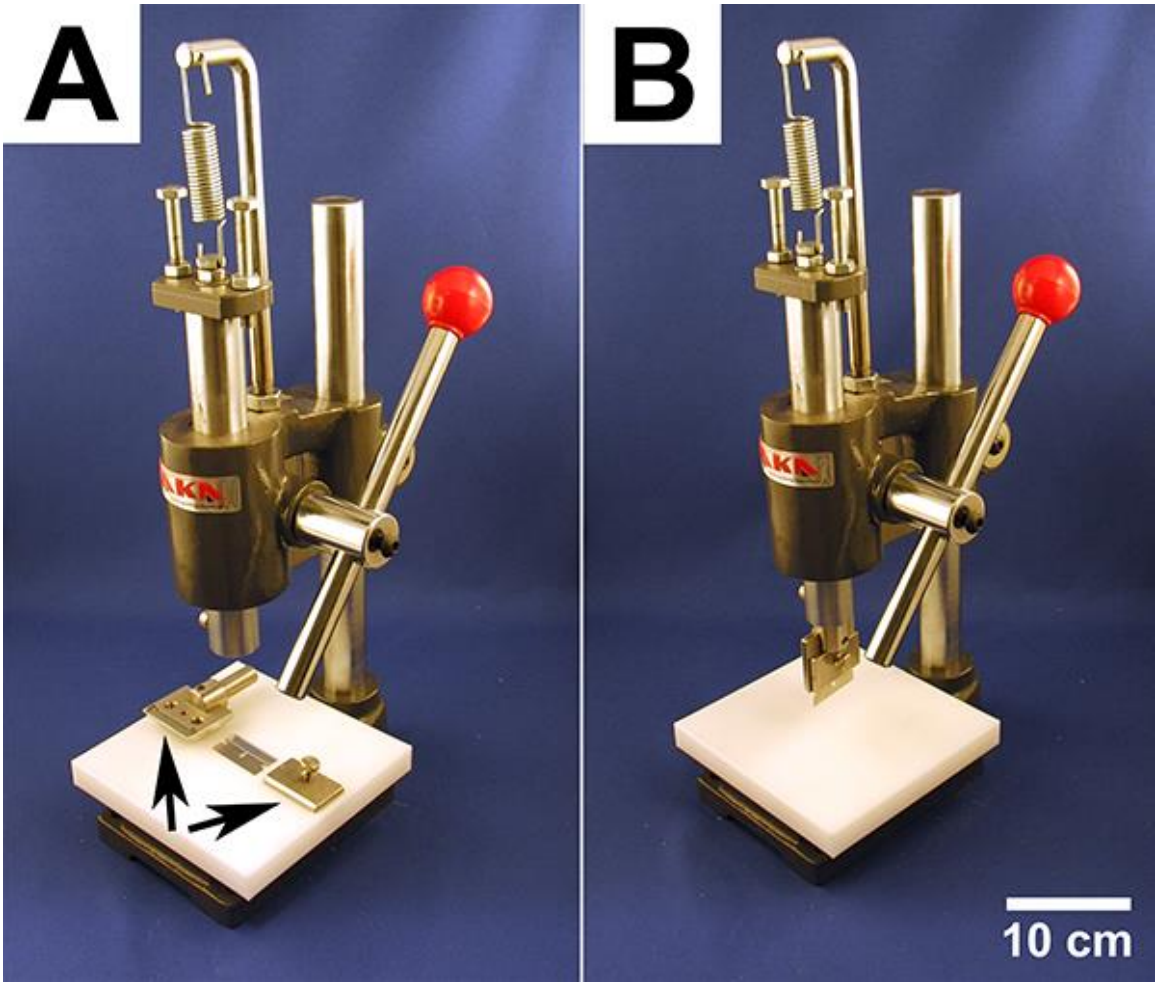

Figure 4.2: Constructed custom rat knee bisector. (**A**) Arbor press with a modified insert (black arrows) that can accommodate and hold razor blades firmly *via* a contoured clam shell design. (**B**) Assembled knee bisector. Cutting surface (polyoxymethylene, Delrin®) is removable and customizable (*i.e.* implementation of customized anatomical indentations).

4.2.5.3 Statistical Analysis

All image analysis was performed with MicroView software (v2.12, GE Healthcare, London, ON, CAN). Subsequent statistical analysis was done using Prism (Graphpad v7.03, La Jolla, CA, USA), and statistical significance was achieved if $p < 0.05$.

4.3 Results and Discussion

The successful complete perfusion of rat hindlimbs and selected ROIs (*i.e.* distal femoral epiphysis and proximal tibial epiphysis) was demonstrated *via* the contrast enhanced visualization of the epiphyseal (Figure 4.3A and B), metaphyseal (Figure 4.3C and D) and primary nutrient arteries of long bones (Figure 4.3C and D). The previously mentioned vessels represented the main blood supplies for the distal femoral epiphysis and proximal tibial epiphysis. Within our study, all N = 56 rats exhibited contrast enhanced epiphyseal, metaphyseal and primary nutrient arteries. Results of a paired t-test between the ipsilateral and contralateral hindlimbs within each rat, to evaluate uniformity of perfusion within each rat, showed no significant differences ($p = 0.9275$, Figure 4.4). With no statistical different between ipsilateral and contralateral hindlimbs, values at each time-point were averaged prior to linear regression analysis. Results of this analysis revealed a non-statistically significant deviation from a slope of zero ($p = 0.0828$, Figure 4.4).

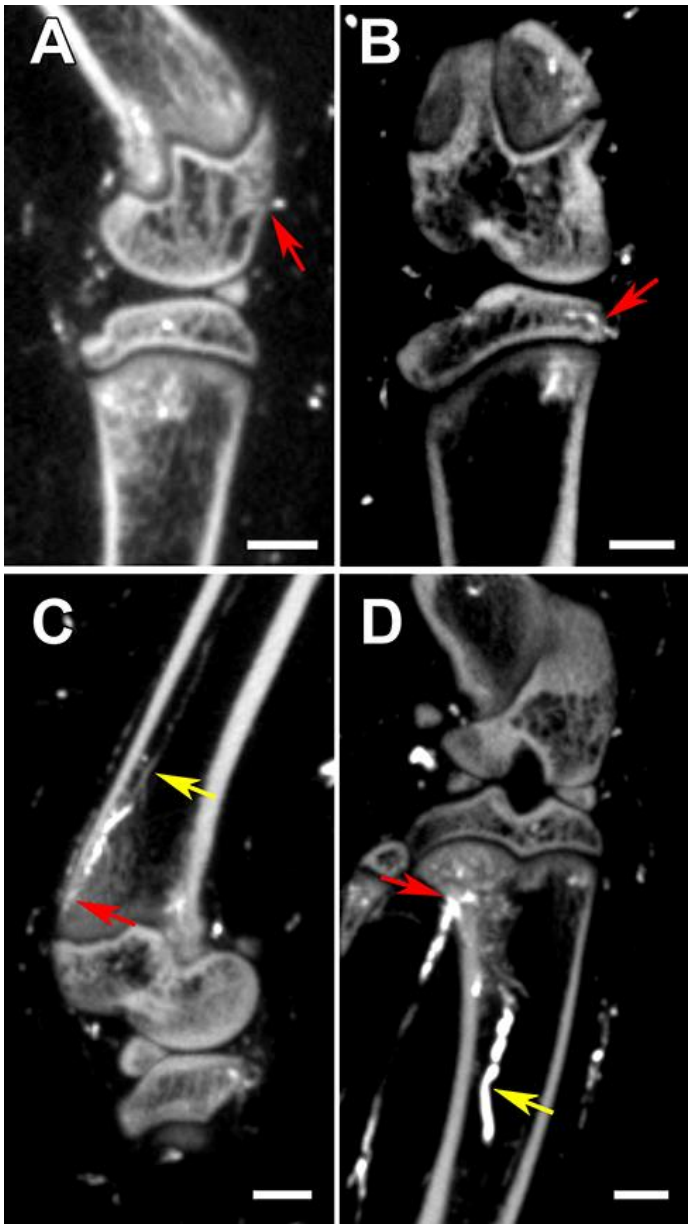

Figure 4.3: Maximum intensity projections (MIP) through a 300 μm-thick "slab" of the DECT-acquired high-energy image volume, demonstrated the success of the rat hindlimb perfusions. Epiphyseal nutrient arteries, and the associated foramen (red arrows) feeding the distal femoral epiphysis (**A**) and proximal tibial epiphysis (**B**). Another source of blood vessels can be found below the growth plate, as demonstrated in femur (**C**) and tibia (**D**), with red arrows denoting the metaphyseal nutrient arteries and their associated foramens. Yellow arrows denote the primary nutrient arteries (*i.e.* one major source of blood supply).

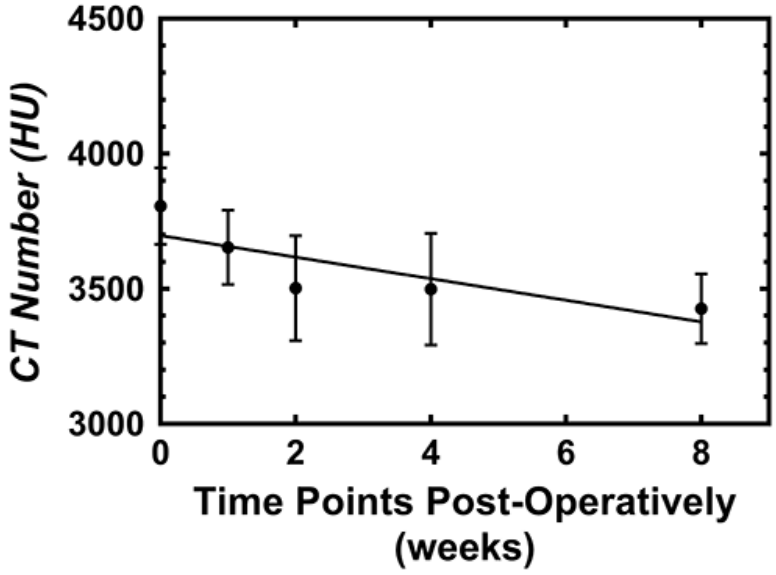

Figure 4.4: Graph depicting the contrast enhancement of the femoral artery across the entire 8-week long study. The mean femoral arterial values from 500 x 500 x 500 µm ROIs were collected from both hindlimbs of all perfused rats. A paired t-test revealed no statistical differences ($p = 0.9275$) between ipsilateral and contralateral hindlimbs. Mean values, from both hindlimbs, at each time point (T = 0 (pre-operatively), 1, 2, 4, and 8 weeks post-operatively) were averaged and plotted with their standard deviation. Linear regression analysis reported across the entire study duration revealed no statistically deviation from a slope of zero ($p = 0.0828$).

With the consistent and uniform perfusion across all rats, we acquired DECT scans of both ipsilateral (operated) and contralateral (non-operated) hindlimbs from all rats, and decomposed the acquired low- and high-energy volumes (Figure 4.5, top panels) into their respective soft tissue, bone, and vessel volumes (Figure 4.5, bottom panels). To visually emphasize the consistent success of our perfusion and DECT technique, we have also presented radiographic projections through decomposed bone-, vessel-only, and a composite image from selected samples of each surgery group and time-point (Figure 4.6).

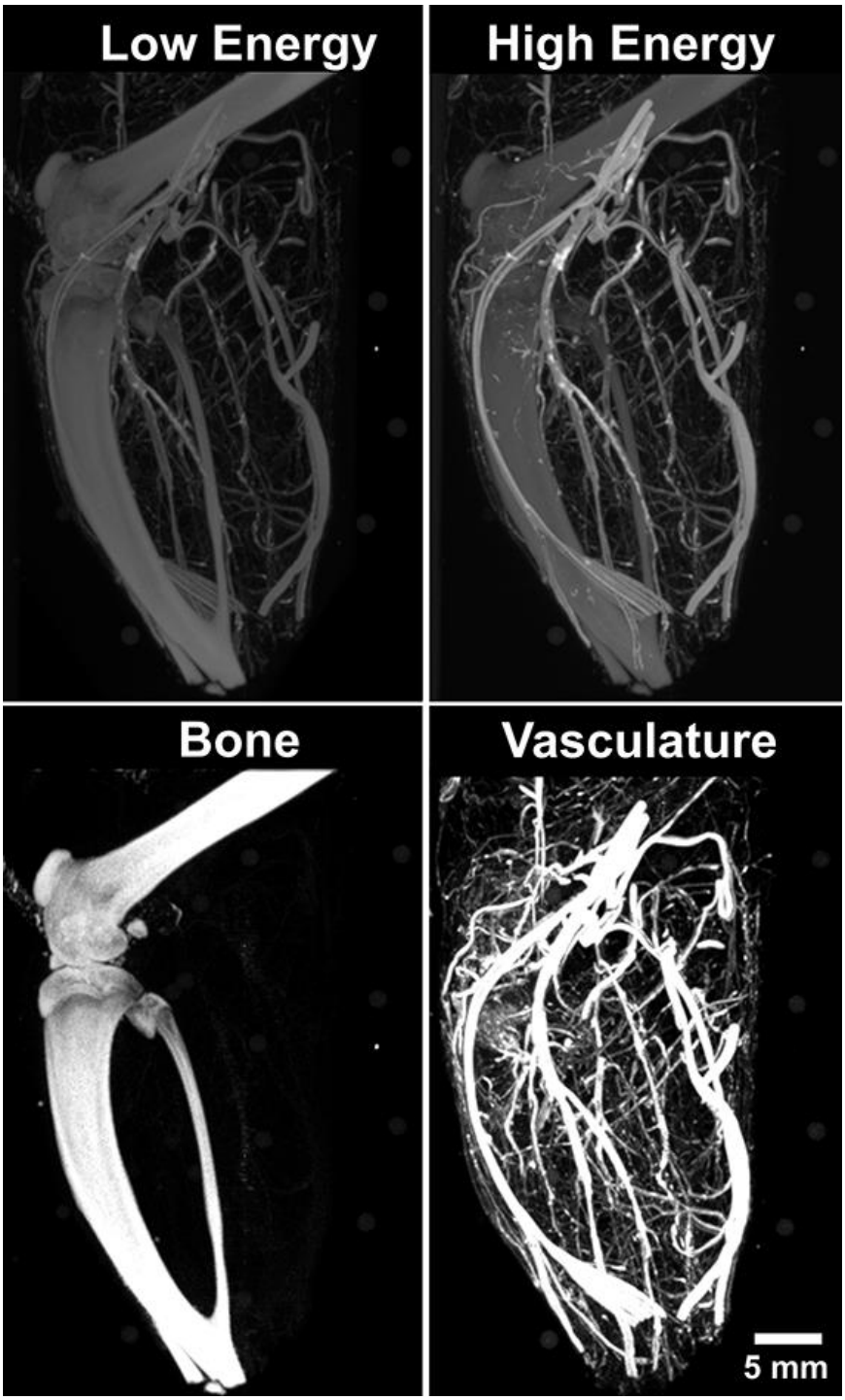

Figure 4.5: Maximum intensity projections (MIP) through a perfused rat hindlimb that has been DECT-scanned. Top panels display the DECT-acquired low- and high-energy volumes. The automated DECT decomposition results in visually distinct bone and vessel-only images (bottom panels).

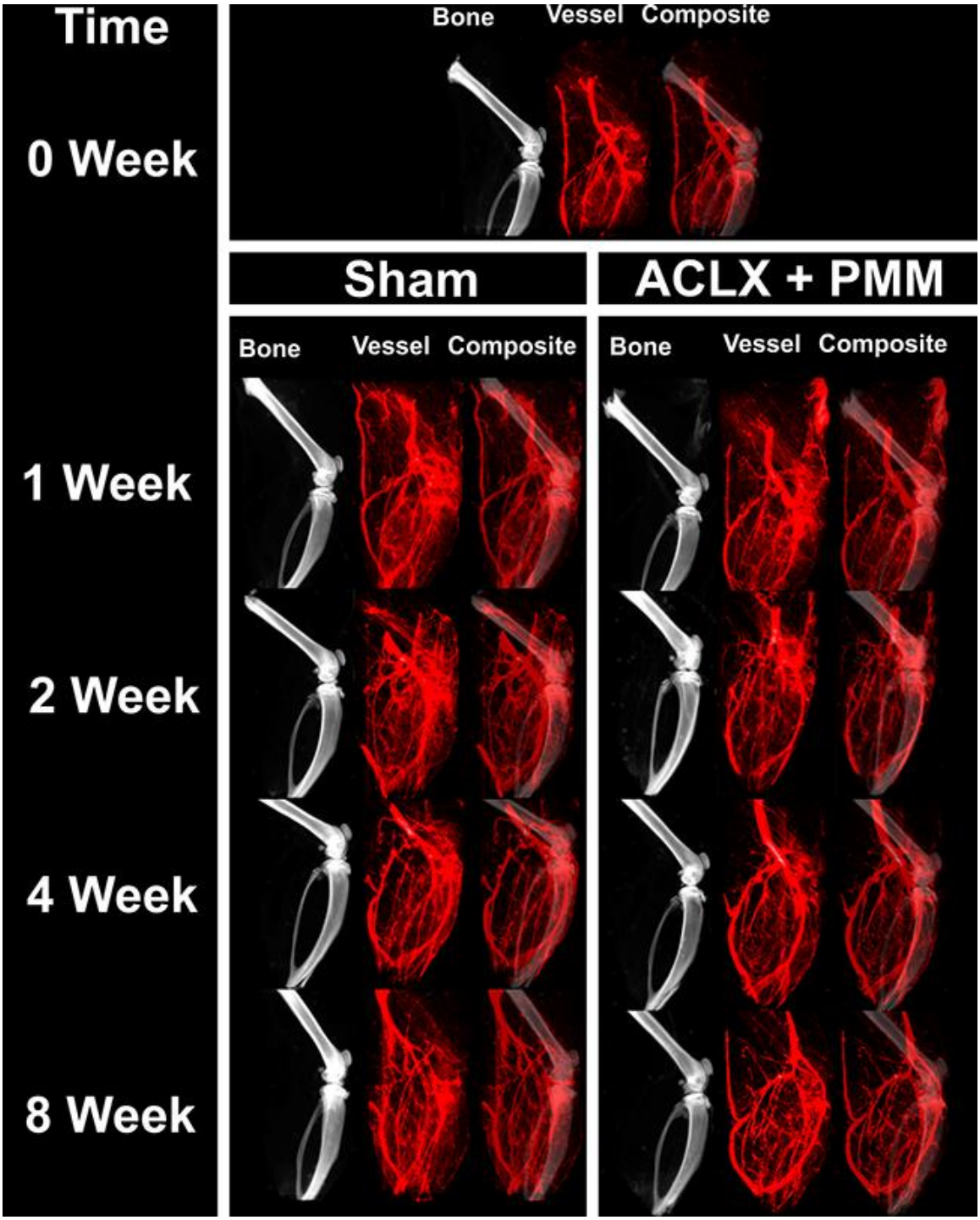

Figure 4.6: A representative figure displaying the consistent and uniform perfusion of every sample, regardless of surgery and time-point. Presented are x-ray projections through the bone-(white), vessel-only (red), and a composite overlay of the decomposed volumes of a sample from the sham or ACLX + PMM surgery group and at every time-point.

Following the successful perfusion and DECT-decomposition of all rats, five selected rats were DECT-scanned at a higher resolution (33 µm) to evaluate the effects of PVE. The results of a repeated-measures, nonparametric, one-way ANOVA, and Dunn's post-hoc multi-comparative analysis on the measured microvessel voxel volume fractions from the distal femoral epiphysis and proximal tibial epiphysis are displayed in Figure 4.7. The statistical analysis revealed significant differences ($p<0.05$) between voxel volume fractions recorded from volumes reconstructed at 33 and 132 µm, in both the femur and tibia. Thus, it is apparent from our results that DECT is affected by PVE between the extremes of the experimented rebinned voxel spacing range (*i.e.* 33 and 132 µm). However, as an assurance, all samples within this study were scanned with identical scan parameters, and identically decomposed and analyzed; thus, the results are directly comparable with one another and should not be affected by PVE.

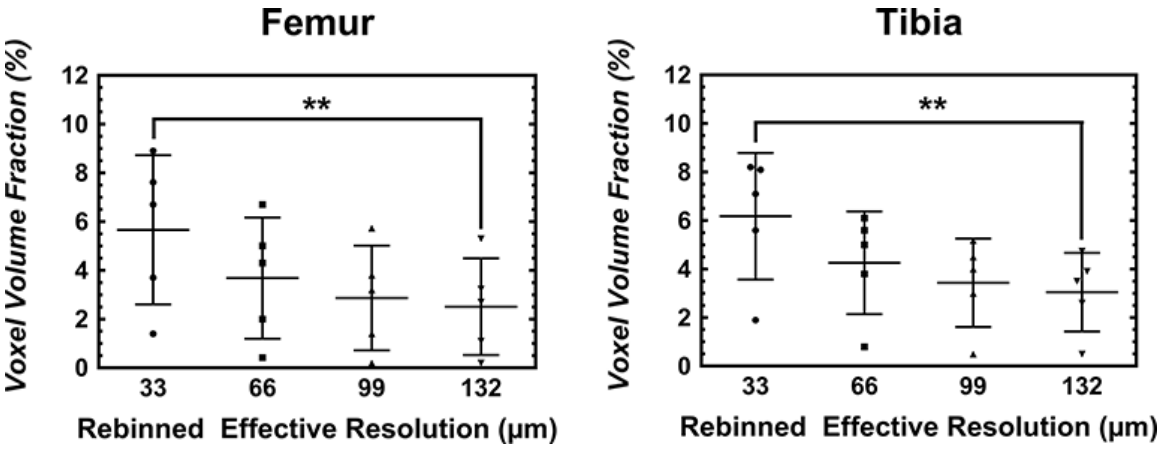

Figure 4.7: Graphs depicting the results of partial volume effects (PVE) on dual-energy micro-CT (DECT). Graphs displays the femur and tibia mean values and standard deviations of voxel volume fractions collected from ROIs (*i.e.* distal femoral epiphysis and proximal tibial epiphysis) within five perfused rats across natively-collected 33 µm and rebinned 2 × 2, 3 × 3, and 4 × 4 to provide effective voxel spacings of 66, 99, and 132 µm, respectively. Repeated-measures, nonparametric, one-way ANOVA, with Dunn's post-hoc multi-comparative analysis, revealed a statistical difference ($p<0.05$) between voxel volume fractions recorded at 33 and 132 µm in both the femur and tibia.

From each high-energy acquisition, operator-generated VOIs (Figure 4.1) of the distal femoral epiphysis and proximal tibial epiphysis were transposed within each of their respective inherently co-registered decomposed volumes (*i.e.* soft tissue, bone, and microvessel) for both ipsilateral and contralateral hindlimbs. The average mean value was collected from each individual VOI and arranged by decomposed component, anatomical location, hindlimb and surgery group and plotted against time (*i.e.* T = 0 (pre-operatively), 2, 4, and 8-weeks post-operatively). Presented are the results for the microvessels (Figure 4.8), subchondral bone (Figure 4.9), and soft tissue (Figure 4.10).

Results of a two-way ANOVA analysis on the microvessel voxel volume fractions from the ipsilateral (operated) and contralateral (non-operated) hindlimbs of the ACLX + PMM surgery group revealed a statistical increase in the ipsilateral tibia 1 – week post-operatively ($p = 0.0472$, Figure 4.8). No further significant differences ($p > 0.05$) were revealed between hindlimbs at the remaining time-points; at 2 – weeks post-operatively and for the remainder of the experimental duration, the microvessel density returned and remained at baseline levels (*i.e.* 0 – weeks, pre-operatively) (Figure 4.8). Thus, our results suggest that angiogenesis within the ipsilateral tibia may be a result of an acute inflammatory response immediately following surgery.

Analysis of subchondral bone voxel volume fractions (Figure 4.9), of the chosen ROIs, between the ipsilateral and contralateral hindlimb of the ACLX + PMM surgery group revealed no statistical differences ($p > 0.05$, two-way ANOVA, Prism) for each individual time point. Thus, it appears that the combination of ACLX + PMM may not significantly impact subchondral bone voxel volume fractions within our chosen ROIs of the distal femoral epiphysis and proximal tibial epiphysis. This was surprising, as previous research by our group using the same ACLX + PMM model has reported volumetric bone mineral density (vBMD) changes between the ipsilateral and contralateral hindlimbs.[38] In the current study, the absence of detectable significant changes in subchondral bone may be due to differences in ROIs used between the studies. McErlain *et al.*, utilized cylindrical ROIs with a 0.75 mm diameter and depth of ~ 1 mm in the subchondral bone. Conversely, in our study we included some of the cortical shell outlining the distal femoral epiphysis and proximal tibial epiphysis, in an effort to record

vessels that are known to penetrate the cortical shell and invade cartilage. Consequently, the dense cortical shell may mask subtle changes to the subchondral bone densities and provide overestimated voxel volume fractions of subchondral bone for our studied ROIs (*i.e.* distal femoral epiphysis and proximal tibial epiphysis).

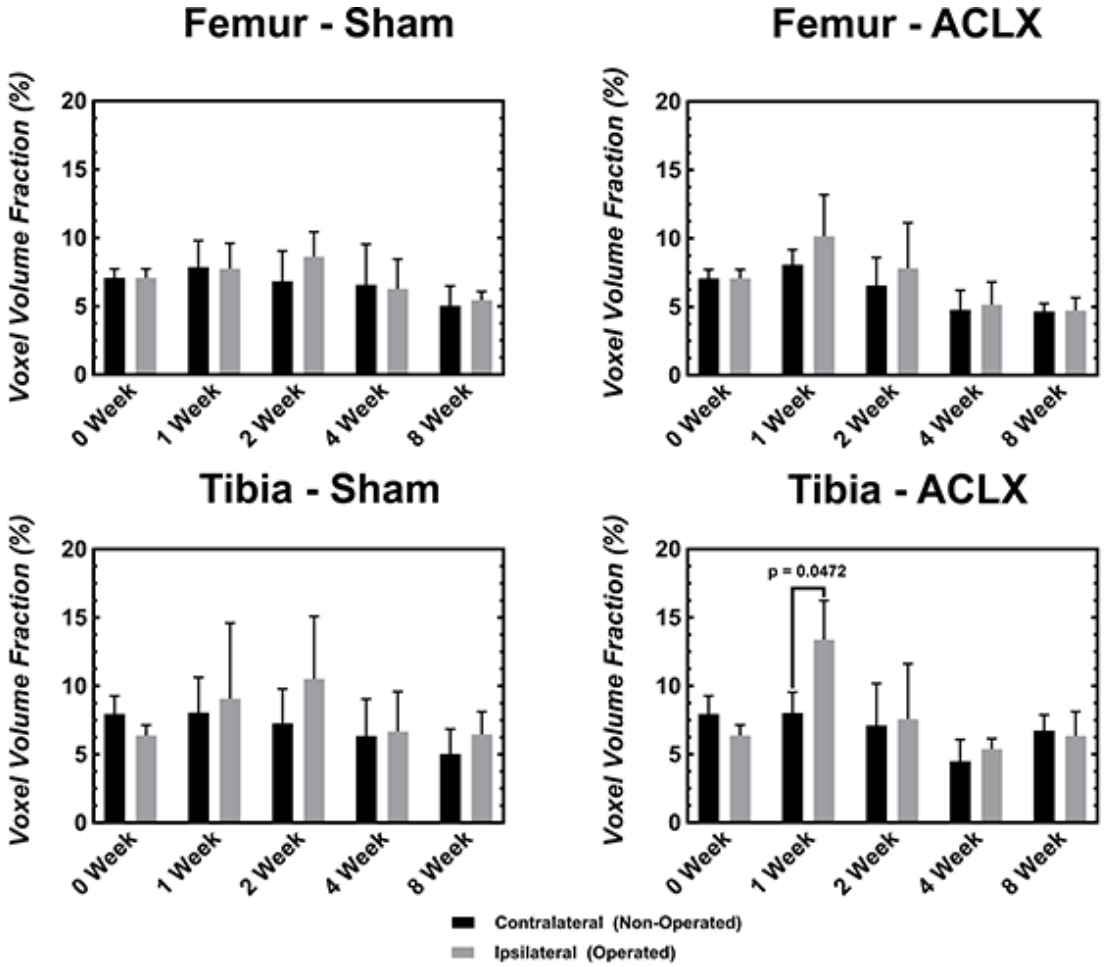

Figure 4.8: Results of the vessel voxel volumes fractions within custom 3D VOIs (**Figure 4.1**) of the ipsilateral (operated) and contralateral (non-operated) hindlimbs' distal femoral epiphysis and proximal tibial epiphysis from both sham and ACLX rats over the 8-week study period. Each bar represents the mean and standard deviation of N=6 rats per time-point.

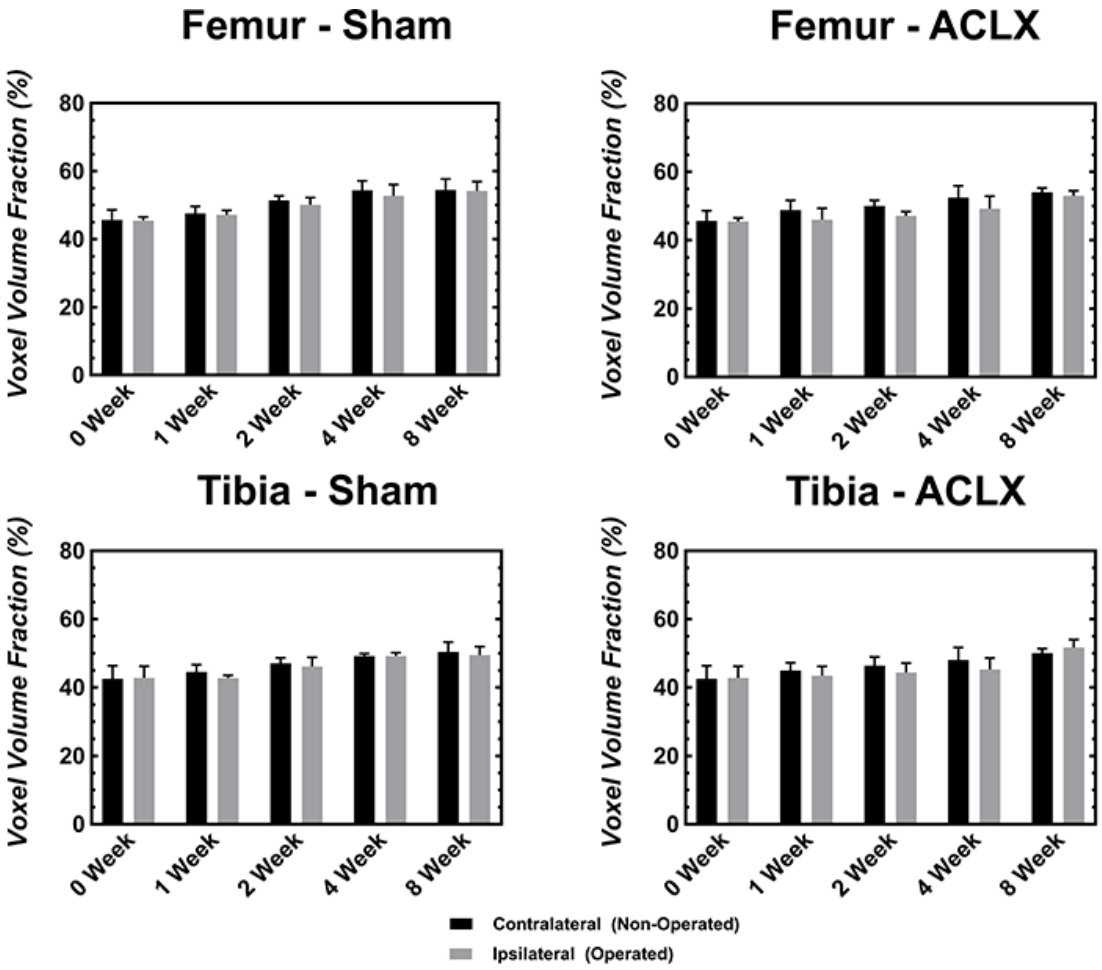

Figure 4.9: Results of the bone voxel volumes fractions within custom 3D VOIs (**Figure 4.1**) of the ipsilateral (operated) and contralateral (non-operated) hindlimbs' distal femoral epiphysis and proximal tibial epiphysis from both sham and ACLX rats over the 8-week study period. Each bar represents the mean and standard deviation of N=6 rats per time-point.

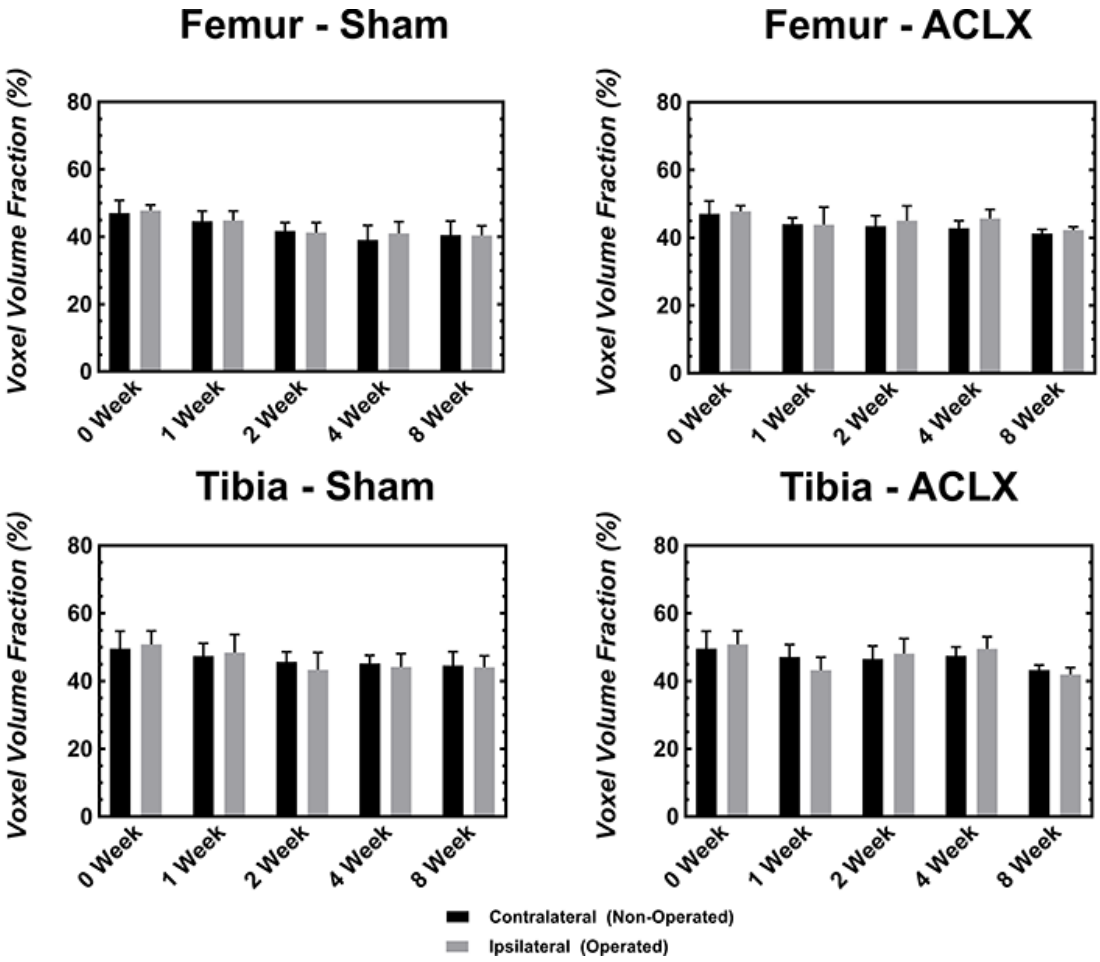

Figure 4.10: Results of the soft-tissue voxel volumes fractions within custom 3D VOIs (**Figure 4.1**) of the ipsilateral (operated) and contralateral (non-operated) hindlimbs' distal femoral epiphysis and proximal tibial epiphysis from both sham and ACLX rats over the 8-week study period. Each bar represents the mean and standard deviation of N=6 rats per time-point.

To validate the sham surgery as an external control, we also performed a two-way ANOVA statistical analysis on the voxel volumes fractions of microvessels (Figure 4.8), bone (Figure 4.9), and soft tissue (Figure 4.10) obtained from ROIs within both the ipsilateral and contralateral hindlimbs. For any of the decomposed components, our results revealed no significant differences ($p > 0.05$) between the ipsilateral (operated) and contralateral hindlimbs (non-operated) of the sham surgery group within each

individual timepoint. Therefore, the sham surgery served as an effective external control in this study.

As an additional comparison, using data collected from the ACLX + PMM surgery group, we compared the microvessel voxel volume fractions of the distal femoral epiphysis and proximal tibial epiphysis of both ipsilateral and contralateral hindlimbs against the sham control. Analysis from a two-way ANOVA revealed no statistical differences ($p > 0.05$) when comparing the ipsilateral or contralateral femurs and tibias between both surgery groups (Figure 4.11). Of interest is the lack of significance between the 1 – week ipsilateral tibias, as a significant increase was shown when comparing the ipsilateral and contralateral hindlimbs of the ACLX + PMM surgery group (Figure 4.8). This non-significance against the sham ipsilateral tibia may suggest that in the ACLX + PMM group the release of inflammatory molecules post-surgery may be systemic, causing an increase of angiogenesis in the ipsilateral hindlimb and a decrease within the respective contralateral hindlimb. These results are not surprising, as previous research has shown the increase in genetic expression,[47,48] and inflammatory factors post-surgery.[49-51]

In contrast to simple greyscale thresholds on single-energy scans, we have shown that the ability to mathematically decompose DECT-acquired volumes into individually segmented and quantitative components, is resistant to PVE. To our knowledge, this allowed our study to be the first to accurately quantify the microvessel density within the distal femoral epiphysis and proximal tibial epiphysis of intact rat knee joints. The average microvessel density of rats perfused at 0 – week (*i.e.* pre-operatively) in the distal femoral epiphysis and proximal tibial epiphysis were $7.7 \pm 1.5\%$ and $7.2 \pm 1.3\%$, respectively (Figure 4.8).

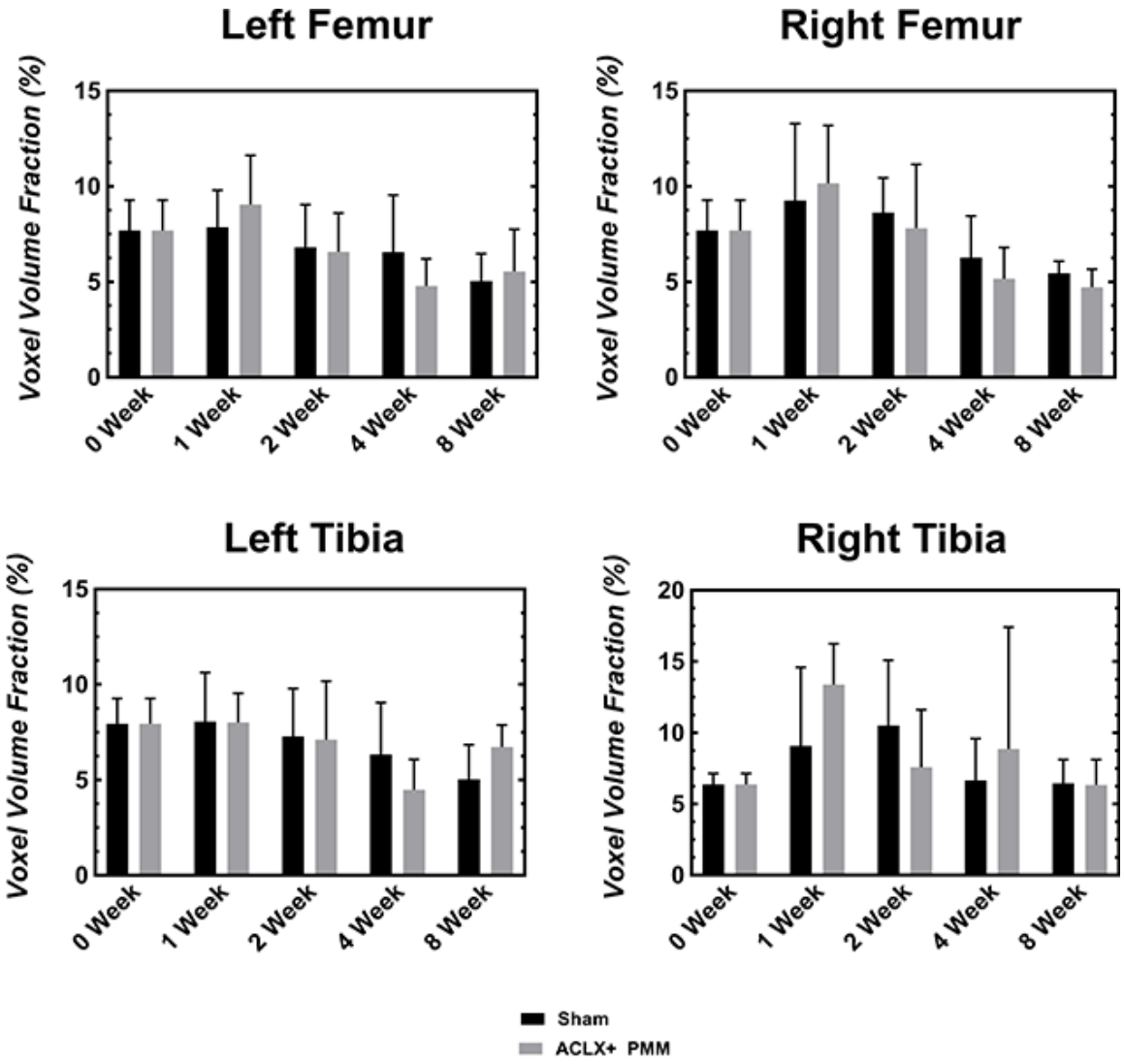

Figure 4.11: Results of a comparison between microvessel voxel volumes fractions of the ipsilateral (operated) and contralateral (non-operated) hindlimb between sham and ACLX + PMM surgery groups. Each bar represents the mean and standard deviation of N=6 rats per time-point.

Finally, histological sectioning and Toluidine blue staining confirmed the progression of OA. Degeneration of the articular cartilage, as noted by a reduction in blue staining (*i.e.* reduced proteoglycan and glycosaminoglycan concentration) was clearly present in both the femur and tibia (Figure 4.12B, D, and F) of a hindlimb that underwent the ACLX + PMM surgery. Conversely, a sample histological section taken from a 1 – week post-operative sham operation revealed healthy cartilage (Figure 4.12A, C and E).

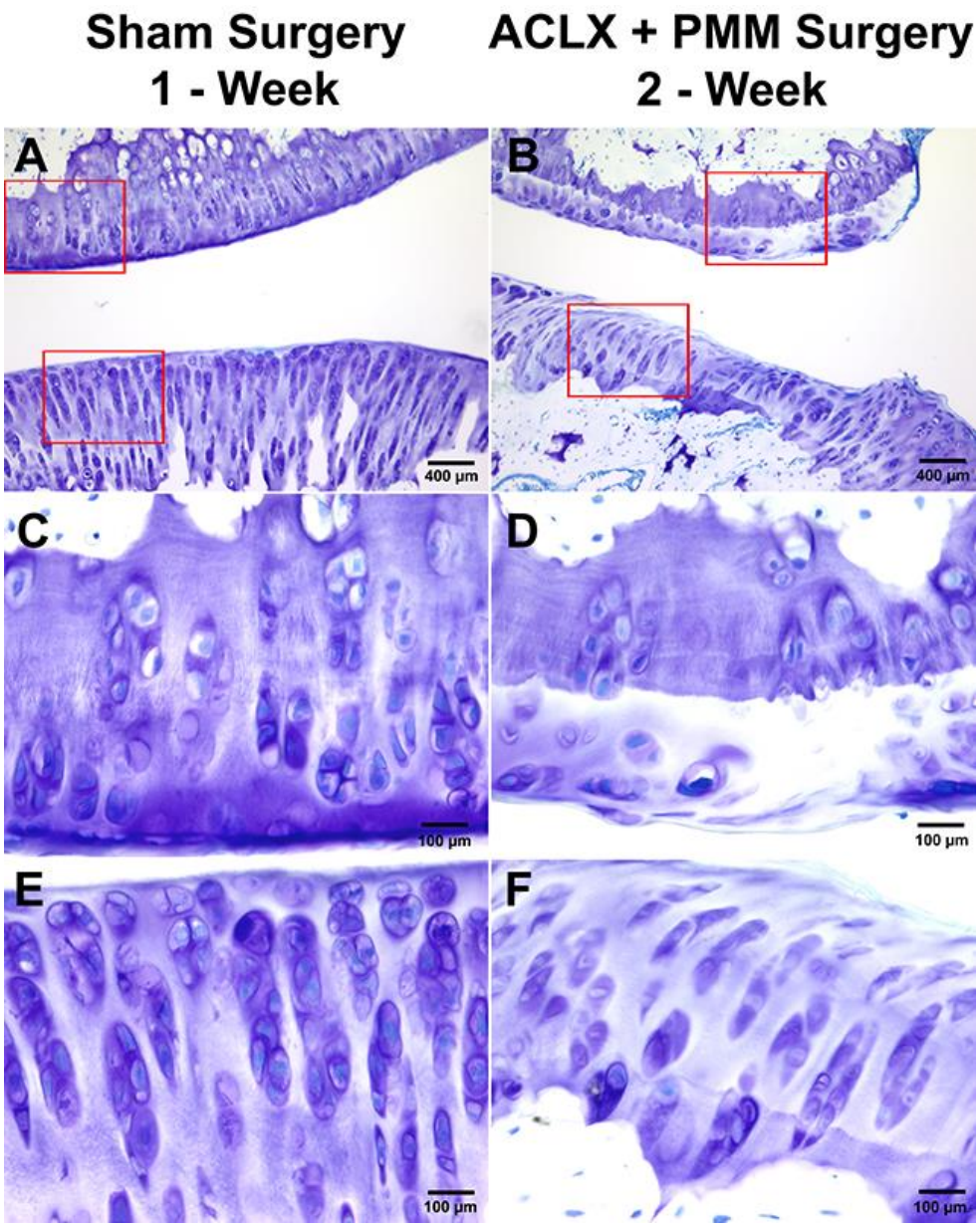

Figure 4.12: Microscopic histological staining (Toluidine Blue) results of rat hindlimbs that have undergone either a sham and ACLX + PMM surgery, 1 - week (**A**, **C**, and **E**) and 2-week (**B**, **D**, and **F**) post-operatively, respectively. 10x magnification of the medial aspect of the joint, displaying the intact (sham, **A**) or degenerated (ACLX + PMM, **B**) cartilaginous surfaces of the femur (top) and tibia (bottom) of rats. 40x magnification of outlined regions-of-interest (ROI) within the femur of sham (**C**) and ACLX + PMM (**D**) rats. 40x magnification of outlined ROIs within the tibia of sham (**E**) and ACLX + PMM (**F**) rats. Note the loss of consistent Toluidine Blue staining throughout the entire cartilage layer in (**D**) and (**F**), as well as a reduction in chondrocyte organization, both indicative of cartilage degeneration.

4.3.1 Limitations

The main limitation of our study lies in fact that the Er-based vascular perfusion contrast agent is strictly limited for use with post-mortem samples.[36] This limitation inhibits the study of changes within the same vascular- and bone-networks within an animal, for extended periods of time (*i.e*. longitudinal studies). However, current developments into an *in vivo* vascular contrast agent,[52] and corresponding optimized DECT protocols, can overcome this challenge and is the topic of future studies within our group.

While the results of our statistical analysis of partial volume effects (PVE) on DECT revealed a significant difference ($p<0.05$) between voxel volume fractions recorded from a 33 µm and 132 µm reconstructed volume, a general downward trend can be observed in Figure 4.7. Thus, it may be possible that results derived from our data (which was reconstructed with 100 µm voxel spacing) may slightly underestimate the true microvessel volume fractions. Acquiring DECT scans at 33 µm would provide a more accurate representation of the vessel density (Figure 4.4); however, the time required to scan all 100+ samples within this study would be significantly increased (*i.e.* 16 hr DECT scan at 33 µm in comparison to 3 hr DECT scan at 100 µm per sample).

An additional limitation is the lack of an OARSI score within the rat hindlimbs. The osteoarthritis research society international (OARSI) score is a standardized measurement of OA severity within a rat joint. In this study, a small subset of rat joints was processed for histological evaluation due to the large amount of time required to prepare all 108 samples for decalcification, histological sectioning, staining, and OARSI grading. However, the surgical model of OA used in this study that has been previously well-characterized,[38,39] and additional histological analysis can be carried out on the remaining decalcified specimens.

In this study, the VOIs were limited to the distal femoral epiphysis and proximal tibial epiphysis, due to their proximity to articular cartilage, known importance in nutrient and oxygen supply to cartilage, and well-defined contours. However, the synovium[53-55] and patellofemoral region[56-58] are also known to be required for the healthy maintenance of the joint.[53-55] As DECT-decomposition of the synovial membrane and patellofemoral

regions were simultaneously acquired with the data presented in this study, research into the associated bone and microvessel changes within these regions is a topic of further research.

4.4 Conclusion

In an ACLX + PMM surgical model of OA, 8-week post-operative study period, and chosen ROIs directly underlying the articular cartilage of the knee joint (*i.e.* distal femoral epiphysis and proximal tibial epiphysis), we did not observe any significant overall changes to the microvessel voxel volume fraction, suggesting that the subchondral microvasculature did not play a significant role in our study of OA. Thus, future studies using the same OA model and timeline as proposed in this study may benefit by examining the microvessel changes within the neighbouring vascularized synovial membrane and patellofemoral region.

Overall, in this study, we utilized a previously characterized combination technique – a highly attenuating x-ray contrast agent[36] with compatible, optimized DECT[37] – to non-destructively, automatically and objectively segment individual quantitative volumes of soft tissue, subchondral bone, and microvessels within a surgically-induced rat hindlimb model of OA. While the current implementation of this combination imaging technique cannot facilitate the visualization and resolution of individual microvessels (*i.e.* capillaries, < 10μm), it provided quantitative measurements of tissue volume from 1 nL voxels (*i.e.* 100 μm cubic voxels). This high degree of sensitivity allowed us to detect an inflammatory or dilatory response 1-week post-ACLX + PMM surgery within the tibias of operated hindlimbs, represented as a significant increase ($p=0.0472$) in microvessel voxel volume fraction

The combination technique (*i.e.* contrast agent and optimized DECT) utilized within this study provided the first-of-its kind ability to simultaneously study the soft tissue, bone, and perfused vessels within an intact sample. However, the imaging and analysis methodologies presented in this study are not limited to OA, but can be advantageous for the examination of interactions between different tissues in vascular-related diseases: neurological,[59] cardiovascular,[60,61] musculoskeletal,[60,62,63] and oncological.[64-66]

4.5 References

1. A. Litwic, M. Edwards, E. Dennison, C. Cooper, Epidemiology and Burden of Osteoarthritis. *British Medical Bulletin* **105**, 185-199 (2013).

2. T. Neogi, The epidemiology and impact of pain in osteoarthritis. *Osteoarthritis Cartilage* **21**, (2013).

3. J. H. Salmon, A. C. Rat, J. Sellam, M. Michel, J. P. Eschard, F. Guillemin, D. Jolly, B. Fautrel, Economic impact of lower-limb osteoarthritis worldwide: a systematic review of cost-of-illness studies. *Osteoarthritis and Cartilage* **24**, 1500-1508 (2016).

4. F. V. Wilder, J. P. Barrett, E. J. Farina, Joint-specific prevalence of osteoarthritis of the hand. *Osteoarthritis and Cartilage* **14**, 953-957 (2006).

5. L. Solomon, C. M. Schnitzler, J. P. Browett, Osteoarthritis of the hip: the patient behind the disease. *Annals of the Rheumatic Diseases* **41**, 118-125 (1982).

6. A. J. Baliunas, D. E. Hurwitz, A. B. Ryals, A. Karrar, J. P. Case, J. A. Block, T. P. Andriacchi, Increased knee joint loads during walking are present in subjects with knee osteoarthritis. *Osteoarthritis and Cartilage* **10**, 573-579 (2002).

7. A. P. Goode, T. S. Carey, J. M. Jordan, Low Back Pain and Lumbar Spine Osteoarthritis: How Are They Related? *Current Rheumatology Reports* **15**, 305 (2013).

8. A. Anandacoomarasamy, L. March, Current evidence for osteoarthritis treatments. *Therapeutic Advances in Musculoskeletal Disease* **2**, 17-28 (2010).

9. A. S. Anderson, R. F. Loeser, Why is Osteoarthritis an Age-Related Disease? *Best Pract Res Clin Rheumatol* **24**, 15 (2010).

10. M. Blagojevic, C. Jinks, A. Jeffery, K. P. Jordan, Risk factors for onset of osteoarthritis of the knee in older adults: a systematic review and meta-analysis. *Osteoarthritis Cartilage* **18**, 24-33 (2010).

11. E. M. Roos, Joint injury causes knee osteoarthritis in young adults. *Curr Opin Rheumatol* **17**, 195-200 (2005).

12. J. T. Badlani, C. Borrero, S. Golla, C. D. Harner, J. J. Irrgang, The effects of meniscus injury on the development of knee osteoarthritis: data from the osteoarthritis initiative. *Am J Sports Med* **41**, 1238-1244 (2013).

13. J. A. Buckwalter, Articular Cartilage Injuries. *Clinical Orthopaedics and Related Research* **402**, 21-37 (2002).

14. R. Pandey, N. Kumar, S. Paroha, R. Prasad, M. Yadav, S. Jain, H. Yadav, Impact of obesity and diabetes on arthritis: An update. *Health* **Vol.05No.01**, 14 (2013).

15. G. Schett, A. Kleyer, C. Perricone, E. Sahinbegovic, A. Iagnocco, J. Zwerina, R. Lorenzini, F. Aschenbrenner, F. Berenbaum, M. A. D'Agostino, J. Willeit, S. Kiechl, Diabetes is an independent predictor for severe osteoarthritis: results from a longitudinal cohort study. *Diabetes Care* **36**, 403-409 (2013).

16. M. M. Rahman, J. A. Kopec, J. Cibere, C. H. Goldsmith, A. H. Anis, The relationship between osteoarthritis and cardiovascular disease in a population health survey: a cross-sectional study. *BMJ Open* **3**, (2013).

17. T. D. Spector, A. J. MacGregor, Risk factors for osteoarthritis: genetics. *Osteoarthritis Cartilage* **12, Supplement**, (2004).

18. T. D. Spector, F. Cicuttini, J. Baker, J. Loughlin, D. Hart, Genetic influences on osteoarthritis in women: a twin study. *Bmj* **312**, 940-943 (1996).

19. D. M. Findlay, Vascular pathology and osteoarthritis. *Rheumatology (Oxford)* **46**, 1763-1768 (2007).

20. D. M. Findlay, J. S. Kuliwaba, Bone–cartilage crosstalk: a conversation for understanding osteoarthritis. *Bone Research* **4**, 16028 (2016).

21. J. Liu, J. Dai, Y. Wang, S. Lai, S. Wang, Significance of new blood vessels in the pathogenesis of temporomandibular joint osteoarthritis. *Experimental and Therapeutic Medicine* **13**, 2325-2331 (2017).

22. P. Suri, J. N. Katz, J. Rainville, L. Kalichman, A. Guermazi, D. J. Hunter, Vascular disease is associated with facet joint osteoarthritis. *Osteoarthritis Cartilage* **18**, 1127-1132 (2010).

23. M. Murata, K. Yudoh, K. Masuko, The potential role of vascular endothelial growth factor (VEGF) in cartilage. *Osteoarthritis and Cartilage* **16**, 279-286 (2008).

24. R. D. Prisby, Mechanical, hormonal and metabolic influences on blood vessels, blood flow and bone. *J Endocrinol*, (2017).

25. R. A. D. Carano, E. H. Filvaroff, Angiogenesis and bone repair. *Drug Discovery Today* **8**, 980-989 (2003).

26. J. R. Levick, *An Introduction to Cardiovascular Physiology*. (Elsevier Science, 2013).

27. P. Carmeliet, Angiogenesis in health and disease. *Nat Med* **9**, 653-660 (2003).

28. Y. Wang, L. Wei, L. Zeng, D. He, X. Wei, Nutrition and degeneration of articular cartilage. *Knee Surgery, Sports Traumatology, Arthroscopy* **21**, 1751-1762 (2013).

29. H. Imhof, Zulzbacher, I., Grampp, S., Czerny, C., Youssefzadeh, S., and Kainberger, F., Subchondral Bone and Cartilage Disease A Rediscovered Functional Unit. *Investigative Radiology* **35**, 581-588 (2000).

30. H. Imhof, M. Breitenseher, F. Kainberger, T. Rand, S. Trattnig, Importance of subchondral bone to articular cartilage in health and disease. *Top Magn Reson Imaging* **10**, (1999).

31. Q. Yuan, L. Sun, J.-J. Li, C.-H. An, Elevated VEGF levels contribute to the pathogenesis of osteoarthritis. *BMC Musculoskelet Disord* **15**, 437 (2014).

32. W. D. Burnett, S. A. Kontulainen, C. E. McLennan, D. Hazel, C. Talmo, D. J. Hunter, D. R. Wilson, J. D. Johnston, Knee osteoarthritis patients with severe nocturnal pain have altered proximal tibial subchondral bone mineral density. *Osteoarthritis and Cartilage* **23**, 1483-1490 (2015).

33. P. R. Odgren, H. Witwicka, P. Reyes-Gutierrez, The cast of clasts: catabolism and vascular invasion during bone growth, repair, and disease by osteoclasts, chondroclasts, and septoclasts. *Connect Tissue Res* **57**, 161-174 (2016).

34. T. M. Campbell, K. Reilly, O. Laneuville, H. Uhthoff, G. Trudel, Bone replaces articular cartilage in the rat knee joint after prolonged immobilization. *Bone* **106**, 42-51 (2018).

35. D. W. Holdsworth, M. M. Thornton, Micro-CT in small animal and specimen imaging. *Trends in Biotechnology* **20**, S34-S39 (2002).

36. J. J. Tse, J. Dunmore-Buyze, M. Drangova, D. W. Holdsworth, Erbium-based perfusion contrast agent for small-animal microvessel imaging. *Contrast Media & Molecular Imaging*, In Press (2017).

37. J. J. Tse, J. Dunmore-Buyze, M. Drangova, D. W. Holdsworth, Dual-Energy Computed Tomography for a Gantry-Based Pre-Clinical Cone Beam Micro-CT Scanner. *SPIE Medical Imaging* **Submitted**, (2017).

38. D. D. McErlain, C. T. Appleton, R. B. Litchfield, V. Pitelka, J. L. Henry, S. M. Bernier, F. Beier, D. W. Holdsworth, Study of subchondral bone adaptations in a rodent surgical model of OA using in vivo micro-computed tomography. *Osteoarthritis Cartilage* **16**, 458-469 (2008).

39. C. T. Appleton, D. D. McErlain, J. L. Henry, D. W. Holdsworth, F. Beier, Molecular and histological analysis of a new rat model of experimental knee osteoarthritis. *Ann N Y Acad Sci* **1117**, 165-174 (2007).

40. C. T. Appleton, D. D. McErlain, V. Pitelka, N. Schwartz, S. M. Bernier, J. L. Henry, D. W. Holdsworth, F. Beier, Forced mobilization accelerates pathogenesis: characterization of a preclinical surgical model of osteoarthritis. *Arthritis Res Ther* **9**, R13 (2007).

41. P. V. Granton, S. I. Pollmann, N. L. Ford, M. Drangova, D. W. Holdsworth, Implementation of dual- and triple-energy cone-beam micro-CT for postreconstruction material decomposition. *Med Phys* **35**, 5030-5042 (2008).

42. A. N. Primak, J. G. Fletcher, T. J. Vrtiska, O. P. Dzyubak, J. C. Lieske, M. E. Jackson, J. C. Williams, Jr., C. H. McCollough, Noninvasive differentiation of uric acid versus non-uric acid kidney stones using dual-energy CT. *Acad Radiol* **14**, 1441-1447 (2007).

43. D. N. Tran, M. Straka, J. E. Roos, S. Napel, D. Fleischmann, Dual-energy CT Discrimination of Iodine and Calcium: Experimental Results and Implications for Lower Extremity CT Angiography. *Academic Radiology* **16**, 160-171 (2009).

44. C. A. Coursey, R. C. Nelson, D. T. Boll, E. K. Paulson, L. M. Ho, A. M. Neville, D. Marin, R. T. Gupta, S. T. Schindera, Dual-Energy Multidetector CT: How Does It Work, What Can It Tell Us, and When Can We Use It in Abdominopelvic Imaging? *RadioGraphics* **30**, 1037-1055 (2010).

45. S. Zbinden, L. C. Clavijo, B. Kantor, H. Morsli, G. A. Cortes, J. A. Andrews, G. J. Jang, M. S. Burnett, S. E. Epstein, Interanimal variability in preexisting collaterals is a major factor determining outcome in experimental angiogenesis trials. *American Journal of Physiology - Heart and Circulatory Physiology* **292**, H1891-H1897 (2007).

46. N. Schmitz, S. Laverty, V. B. Kraus, T. Aigner, Basic methods in histopathology of joint tissues. *Osteoarthr Cartil OARS Osteoarthr Res Soc* **18**, (2010).

47. C. T. G. Appleton, V. Pitelka, J. Henry, F. Beier, Global analyses of gene expression in early experimental osteoarthritis. *Arthritis & Rheumatism* **56**, 1854-1868 (2007).

48. J. C. Chang, A. Sebastian, D. K. Murugesh, S. Hatsell, A. N. Economides, B. A. Christiansen, G. G. Loots, Global molecular changes in a tibial compression induced ACL rupture model of post-traumatic osteoarthritis. *Journal of Orthopaedic Research* **35**, 474-485 (2017).

49. D. H. Sohn, J. Sokolove, O. Sharpe, J. C. Erhart, P. E. Chandra, L. J. Lahey, T. M. Lindstrom, I. Hwang, K. A. Boyer, T. P. Andriacchi, W. H. Robinson, Plasma proteins present in osteoarthritic synovial fluid can stimulate cytokine production via Toll-like receptor 4. *Arthritis Res Ther* **14**, R7 (2012).

50. P. Fernandez-Puente, J. Mateos, C. Fernandez-Costa, N. Oreiro, C. Fernandez-Lopez, C. Ruiz-Romero, F. J. Blanco, Identification of a panel of novel serum osteoarthritis biomarkers. *J Proteome Res* **10**, 5095-5101 (2011).

51. G. R. Wohl, R. C. Shymkiw, J. R. Matyas, R. Kloiber, R. F. Zernicke, Periarticular cancellous bone changes following anterior cruciate ligament injury. *Journal of Applied Physiology* **91**, 336-342 (2001).

52. C. Cruje, J. J. Tse, D. W. Holdsworth, E. R. Gillies, M. Drangova, in *SPIE Medical Imaging*. (SPIE, 2017), vol. 10132, pp. 6.

53. D. T. Felson, J. Niu, T. Neogi, Synovitis and the risk of knee osteoarthritis: the MOST Study. *Osteoarthritis Cartilage* **24**, (2016).

54. T. Hügle, J. Geurts, What drives osteoarthritis?—synovial versus subchondral bone pathology. *Rheumatology (Oxford)* **56**, 1461-1471 (2017).

55. R. K. June, R. Liu-Bryan, F. Long, T. M. Griffin, Emerging role of metabolic signaling in synovial joint remodeling and osteoarthritis. *Journal of Orthopaedic Research* **34**, 2048-2058 (2016).

56. D. T. Felson, Challenges of identifying and treating patellofemoral osteoarthritis. *Br J Sports Med* **50**, 832 (2016).

57. N. Wyndow, N. Collins, B. Vicenzino, K. Tucker, K. Crossley, Is There a Biomechanical Link Between Patellofemoral Pain and Osteoarthritis? A Narrative Review. *Sports Medicine* **46**, 1797-1808 (2016).

58. S. Kobayashi, E. Pappas, M. Fransen, K. Refshauge, M. Simic, The prevalence of patellofemoral osteoarthritis: a systematic review and meta-analysis. *Osteoarthritis and Cartilage* **24**, 1697-1707 (2016).

59. C. K. Firoz, N. R. Jabir, M. S. Khan, M. Mahmoud, S. Shakil, G. A. Damanhouri, S. K. Zaidi, S. Tabrez, M. A. Kamal, An overview on the correlation of neurological disorders with cardiovascular disease. *Saudi Journal of Biological Sciences* **22**, 19-23 (2015).

60. M. Laroche, V. Pécourneau, H. Blain, V. Breuil, R. Chapurlat, B. Cortet, B. Sutter, Y. Degboe, Osteoporosis and ischemic cardiovascular disease. *Joint Bone Spine* **84**, 427-432 (2017).

61. I. Danad, B. Ó Hartaigh, J. K. Min, Dual-energy computed tomography for detection of coronary artery disease. *Expert review of cardiovascular therapy* **13**, 1345-1356 (2015).

62. J. B. Cannata-Andia, P. Roman-Garcia, K. Hruska, The connections between vascular calcification and bone health. *Nephrology Dialysis Transplantation* **26**, 3429-3436 (2011).

63. K. Alagiakrishnan, A. Juby, D. Hanley, W. Tymchak, A. Sclater, Role of vascular factors in osteoporosis. *J Gerontol A Biol Sci Med Sci* **58**, 362-366 (2003).

64. P. M. Hoff, K. K. Machado, Role of angiogenesis in the pathogenesis of cancer. *Cancer Treatment Reviews* **38**, 825-833 (2012).

65. H. Nyangoga, P. Mercier, H. Libouban, M. F. Basle, D. Chappard, Three-dimensional characterization of the vascular bed in bone metastasis of the rat by microcomputed tomography (MicroCT). *PLoS One* **6**, e17336 (2011).

66. M. R. Lowerison, J. J. Tse, M. N. Hague, A. F. Chambers, D. W. Holdsworth, J. C. Lacefield, Compound speckle model detects anti-angiogenic tumor response in preclinical nonlinear contrast-enhanced ultrasonography. *Medical Physics* **44**, 99-111 (2017).

Chapter 5

5 Conclusion and Future Directions

5.1 Summary of Results

Osteoarthritis (OA) affects ~10% of Canadians over the age of 15,[1] making it a disease no longer just a concern among the aging population. Currently, there are no therapeutic treatments or disease modifying osteoarthritic drugs (DMOADs) that can halt and reverse the bone and cartilage damage caused by OA.[2,3] The absence of preventative and reversing treatments is due to a lack in knowledge regarding the initiation and progression of OA. Multiple confounding factors such as age,[4,5] diabetes,[6-8] obesity,[4,6,9] and prior injuries[10-12] are responsible for the complexity surrounding OA. Therefore, research into OA is beneficial towards understanding the disease and revealing new targets for drug development.

Recently, a re-emerging OA hypothesis revolves around subtle changes to the delicate microvascular environment surrounding joints.[13,14] Due to the avascular (*i.e.* lack of vessels) nature of cartilage, it is known that their nutrient and oxygen must be supplied from the highly-vascularized neighbouring synovium and subchondral bone.[15] Therefore, slight variations (*i.e.* a decrease or increase) in the homeostatic vascular density of these critical structures (*i.e.* synovium and subchondral bone) may negatively impact and promote their degeneration and the degeneration of cartilage.[16] Nutrients and oxygen from the synovium are known to play an important role in the maintenance of cartilage; however, there is a lack of research in understanding the role of subchondral bone microvessels, more specifically, the distal femoral epiphysis and proximal tibial epiphysis as they neighbor cartilage.

Unfortunately, the small size of microvessels (*i.e.* 5 – 10 μm for capillaries), lack of contrast against surrounding tissues, and proximity to dense bony structures, have hindered their segmentation, characterization, and quantification. Pre-clinical micro-CT is already widely available and routinely used for the visualization and characterization of dense objects, such as bone;[17,18] in combination with an exogenous vascular contrast

agent,[19,20] simultaneous visualization of bone and vessels can be achieved. However, commercially contrast agents provide bone-like greyscale values – hindering their automatic segmentation from one another.[21] Thus, we created a custom *ex vivo* vascular perfusion contrast agent that provides significantly higher contrast than commercially available agents, and is compatible with dual-energy micro-computed tomography (DECT). The advantageous use of DECT allows us to automatically decompose DECT-acquired volumes into separate and quantifiable 3D volumes of soft tissue, subchondral bone, and vessels.

With a highly x-ray attenuating contrast agent and optimized DECT, we combined them with a well-characterized surgically induced rat hindlimb model of OA.[22,23] The combination of an anterior cruciate ligament transection (ACLX) and partial medial meniscectomy (PMM) has been shown to mimic the subtle subchondral bone changes exhibited in early-onset OA within humans, making it ideally suited for the study of microvessel changes. The combination of a custom vascular contrast agent and DECT with a surgically-induced rat hindlimb model of OA (*i.e.* ACLX + PMM) and observational period of 8 – weeks post-surgery, facilitated the simultaneous study of subchondral bone and microvessel density changes during the initiation and progression of OA.

In Chapter 2, titled “Erbium-Based Perfusion Contrast Agent for Small Animal Microvessel Imaging”, a methodology was described to facilitate the fabrication of a custom *ex vivo* vascular perfusion contrast agent comprised of homogeneously incorporated erbium oxide (Er_2O_3) nanoparticles within a two-part silicone elastomer carrier media. Erbium, a lanthanide, was chosen as the base of the contrast agent due to its high x-ray absorption and optimally placed absorption K-edge energy (57.5 keV) for DECT. To break up naturally large aggregates of Er_2O_3, ultrasonic cavitations was employed to facilitate the suspension of nano-sized Er_2O_3 aggregates within the prepared media. Particle sizes were confirmed with transmission electron microscopy (TEM) and dynamic light scattering (DLS, 64.8 ± 11.1 nm). A measured viscosity of 19.2 mPa·s ensured the perfusion of the prepared suspension into microvessels (*i.e* < 10 μm). To demonstrate the efficacy of the custom contrast agent, whole intact mice were perfused

and subsequently scanned with micro-CT. The results of multiple scanned mice revealed perfused vasculature with significantly higher contrast (> 4000 HU) in comparison to surrounding skeletal structures (2359 ± 207 HU) and a commercially available lead-based contrast agent (MV-122, 2683 ± 77.6 HU). The significantly enhanced contrast allowed for the easier visualization of vessels running through foramens (*i.e.* passages that allow vessels to enter bone), and within long bones (*i.e.* femur and tibia). Micro-CT scans of a perfused mouse kidney at a higher resolution (*i.e.* ~ 5 μm) revealed perfused glomeruli (*i.e.* capillary beds) and afferent arterioles (~ 13 μm), validating the ability of the custom Er-based contrast agent to perfuse microvessels.

Dual-energy micro-CT facilitates the automatic segmentation of materials-of-interest based on the change in their x-ray attenuation coefficient between two x-ray energies. The ability to differentiate components can be further enhanced by shifting the CT scanners' mean energy above and below the absorption K-edge of the material of interest. However, the lack of preferential x-ray filtration on pre-clinical cone-beam laboratory-based micro-CT scanners results in poor spectral separation. The addition of metal foils, acting as x-ray filters, can vastly improve spectral separation; yet, this requires opening and modifying the gantry. To avoid machine modifications, in Chapter 3, entitled "Dual-Energy Computed Tomography for a Gantry-Based Pre-Clinical Cone-Beam Micro-CT Scanner", we developed techniques to fabricate customizable in-bore x-ray filters, automate DECT-acquisition, image co-registration, and decomposition algorithms for conventional pre-clinical cone-beam micro-CT scanners. As previously outlined in Chapter 2, Er has an absorption K-edge energy (57.5 keV) located near the mean x-ray energy of micro-CT scanners (~42.7 keV) that operate at maximum x-ray tube potential of 90 kVp. Using Er_2O_3 nano-powder and simple silicone molding techniques, we successfully fabricated a custom cylindrical annular low-energy Er-embedded resin x-ray filter. A removable cylindrical annular-shaped filter would negate the need of modifying the scanner, and would provide x-ray filtration irrespective to gantry rotation. Combined with an identically shaped high-energy Cu filter, these x-ray filters would provide the necessary spectral separation for DECT. We mounted the x-ray filters on a custom automated filter-exchange mechanism that automatically switches x-ray filters within the scanner bore in between low- and high-energy scans. To correct for inherent gantry

motions and non-reproducible bed movements, fiducial marker beads embedded within the sample holder aided in the sub-voxel co-registration between the low- and high-energy volumes. The combination of all the previously outlined developments resulted in the successful implementation of optimized DECT for an Er-based contrast agent on a pre-clinical cone-beam micro-CT scanner. The success of the DECT setup was demonstrated *via* the highly accurate automatic decomposition of Er-perfused rat hindlimbs into separate, distinct, and quantifiable 3D volumes of soft tissue, bone, and perfused vasculature. Statistical analysis of measurements from known pure areas (100 μm^3) of soft tissue, bone, and perfused vessels within each decomposed volume revealed decomposition accuracies of > 98.5%.

In Chapter 4, titled "Studying femoral- and tibial-subchondral bone and vascular changes using dual-energy micro-computed tomography in a surgically-induced rat hindlimb model of osteoarthritis", the combination of an Er-based vascular perfusion contrast agent (Chapter 2) and optimized DECT (Chapter 3) were utilized for the simultaneous investigation into subchondral bone and microvessel density changes during the initiation and progression of OA. For this study we used rats that were divided into various time points (*i.e.* T = 0, 1, 2, 4, and 8 weeks post-operatively) and OA-surgery was performed solely on the right hindlimb. As a control, we utilized both a sham surgery and the contralateral (non-operated) hindlimb from each rat. Due to the avascular nature of cartilage (*i.e.* absence of blood vessels), we chose to study the microvessel network of the neighbouring distal femoral epiphysis and proximal tibial epiphysis. Due to the proximity of the chosen ROIs to cartilage, the microvessels within the ROIs may be responsible for delivering nutrients and oxygen to cartilage. Statistical analysis of microvessel volume fractions revealed a significant increase ($p = 0.0472$) in microvessel density within the ipsilateral tibia 1 – week post-operatively, in comparison to the contralateral hindlimb. This change in vessel density is most likely due to an acute inflammatory response and subsequent angiogenesis. 2 – weeks post-operatively, and till the end of the experiment, the microvessel density returned to baseline (*i.e.* 0 – week). With regards to the subchondral bone and soft tissue, the inflammatory response did not significantly affect these tissues within the chosen ROIs for the entire duration of the study.

5.2 Future Directions

The accumulation of results from the chapters presented within this thesis have demonstrated our ability to (1) produce customized elemental composition vascular contrast agent; (2) fabricate customized shape and composition x-ray filtration for element specific DECT; and (3) combine the previously mentioned techniques to simultaneously study subchondral bone and perfused microvessels within a rat hindlimb model of OA. While our accomplishments have been applied in the study of OA, the advancements achieved within each Chapter can be beneficially adapted for a wide range of applications and studies.

5.2.1 Customized Contrast Agents

We have demonstrated the capabilities of using Er as the basis of a vascular perfusion contrast agent (Chapter 2). An Er-based agent provides significantly higher x-ray contrast than commercially available contrast agents, and its absorption K-edge energy is optimally located for its use with DECT. Recent research, has adapted the base of our Er-based contrast agent for *in vivo* experiments,[24] facilitating the study of the same microvessel networks over time in response to various external challenges (*i.e.* induction of vascular-related diseases, angiogenic, anti-angiogenic drugs, *etc*). In addition to demonstrating the effectiveness of an Er-based contrast agent, the techniques implemented for the fabrication of our contrast agent can be applied to customizing a wide variety of contrast agents.

Un-coated or un-treated nanopowders will tend to clump together due to van der Waals forces.[25,26] However, in Chapter 2, we have shown that ultrasonic cavitation is effective in breaking down larger aggregates of nanoparticulate Er_2O_3 into nano-sized aggregates.[27] Thus, the application of ultrasonic cavitations for the incorporation of nanoparticles within a media can lead to the fabrication of vascular contrast agents of customizable elemental compositions, concentrations, and carrier media.

The ability to customize the vascular contrast agent may lead to the development of more multimodal imaging contrast agents.[28] With respect to micro-CT, as high-energy (*i.e.* >120 kVp) x-ray scanners become more available, contrast agents of higher-Z elements

(*i.e.* higher electron density) would be more favourable[29] for greater contrast (*i.e.* increased x-ray attenuation) within images. Furthermore, vascular contrast agents exhibiting higher-energy absorption K-edge energies can be advantageous for DECT, as the increased photon flux above and below the K-edge will require shorter scan times, and subsequently reduced x-ray dose.

5.2.2 Customizable DECT

The ability to customize the vascular perfusion contrast agent (Chapter 2) combined with our results from Chapter 3 (*i.e.* the fabrication of a large variety of custom sized, shape, and composition x-ray filters) opens the door for DECT to be customized for specific elements-of-interest. We provided the basic technique for the creation of a custom Er-based x-ray filter using inexpensive materials and simple molding techniques. This process allows other researchers to craft custom shaped molds (*i.e.* cylindrical,[30] wedge,[31] or bowtie filters[32,33]) to cast x-ray filters impregnated any element available in nano-powder form – tailoring the output x-ray spectra of the micro-CT scanner to optimize contrast and DECT performance for any material-of-interest.

In Chapter 3 we also presented a custom filter-exchanger that fit within the bore of the micro-CT scanner and allowed for the automated acquisition of DECT images – preventing the need to open and modify the x-ray scanner. Additionally, an automated co-registration software utilized fiducial marker beads surrounding the sample to provide sub-voxel co-registered DECT-acquired volumes. This method of co-registration allowed for the correction in inherent gantry motions and non-reproducible bed movements. Together, we provided an effective implementation of DECT on a large installed base of pre-clinical cone-beam micro-CT scanners.

5.2.3 Vascular Disease Research

In the previous Chapters, we have demonstrated the effectiveness of the combination of our Er-based contrast agent (Chapter 2) and automated DECT technique (Chapter 3) in facilitating the distinct segmentation, visualization, and highly specific quantification of the individual decomposed volumes of soft tissue, bone, and perfused vessels. The results from Chapter 2 and 3 facilitated the simultaneous visualization and quantification of

subchondral bone and microvessels in the distal femoral epiphysis and proximal tibial epiphysis of rats that have undergone an OA-induced surgery. Our results showed an acute inflammatory response 1 – week post-operatively that resulted in a significant increase ($p = 0.0472$) of microvessel density within the ipsilateral tibia, compared to the contralateral (non-operated) hindlimb. However, 2 – weeks post-operatively the microvessel density returned to and remained at baseline levels (*i.e.* 0 – week) for the remainder of the experimental timeframe. Thus, our results suggest that the microvessel density changes within the studied ROIs (*i.e.* distal femoral epiphysis and proximal tibial epiphysis) may not indicate substantial changes with the current OA model (*i.e.* ACLX + PMM). As mentioned in the discussion of limitations in Chapter 4, there is growing interest in the role of the synovial membrane with respect to the supply of oxygen and nutrients to articular cartilage. Some recent papers suggest that the majority of nutrients to cartilage is provided from the synovium.[34-36] In this case, it would be of potential interest to apply our new DECT analytic technique to study concurrent changes in the vasculature of the synovium. In the present study, the synovium of rats was not analyzed, mainly due to the difficulty in defining a consistent 3D volume of interest within this complex structure. However, it is interesting to note that the data acquired in Chapter 4 includes quantitative information about the vascular density within the synovium; this could be studied through retrospective analysis, using operator-defined synovial VOIs. We have performed some preliminary work in this regard, and Figure 5.1 shows a representative contour, 3D-generated VOI, and maximum-intensity projection through a vessel-only DECT-decomposed volume. This preliminary data demonstrates the highly vascularized synovial membrane, consistent with current theories about the role of the synovium in cartilage health and disease. All of the raw 3D images for each rat in this study have been digitally archived, facilitating a retrospective analysis of changes in synovial vascular density as part of a future study.

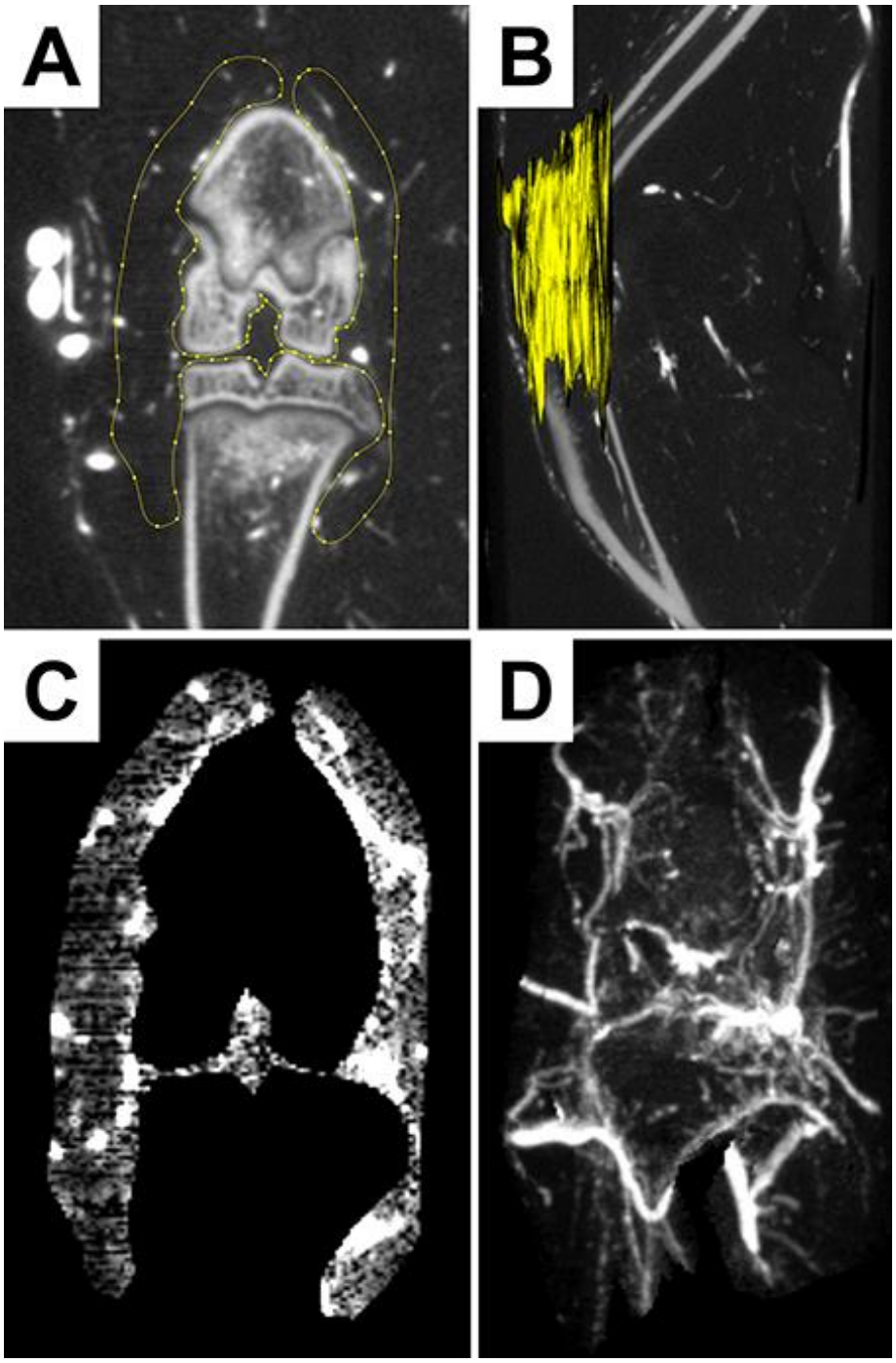

Figure 5.1: Results displaying the contouring process and resulting DECT-decomposed vessels of the synovium from a representative Er-perfused rat hindlimb. (**A**) An operator-generated 2D contour was iterated every 200 µm. (**B**) Interpolation of these 2D contours resulted in a 3D VOI. (**C**) A thick slice maximum intensity projection (MIP), representing the contour in (**A**), through the DECT-decomposed vessel-only volume displaying the highly vascularized synovium. (**D**) A maximum intensity projection through the entire 3D VOI (anterior – posterior).

Apart from our use of an Er-based contrast agent and DECT for the study of bone and vessel changes within a model of OA, the characterization and quantification of bone and vessels can be applicable to a large variety of vascular-related research: cardiac,[37] musculoskeletal,[38,39] oncogenic,[40] and neurological.[41] To emphasize this strength of our novel technique, we sought out collaborations to study vascular changes within oncogenic and musculoskeletal diseases.

Our first collaboration involved the investigation of tumour angiogenesis following treatment with an anti-vascular endothelial growth factor (VEGF) and within control (*i.e.* non-treated) tumours.[42] The cancer cell line used within this study (*i.e.* MDA-MB-231-D3H2-LNluc) can calcify and appear like bone within micro-CT scans. Our role in this collaboration was to provide a technique that would facilitate the visualization of microvessels even in the presence of tumour calcification. The application of our highly x-ray attenuating Er-based contrast agent and optimized DECT will provide the ability to distinguish between vessels permeating possible calcified regions of the tumour. The results of the our micro-CT scans revealed the entire perfused vascular system of a mouse (Figure 5.2A), the tumors encapsulating microvasculature (Figure 5.2B), and blood supply within the tumour mass (Figure 5.2C).[42]

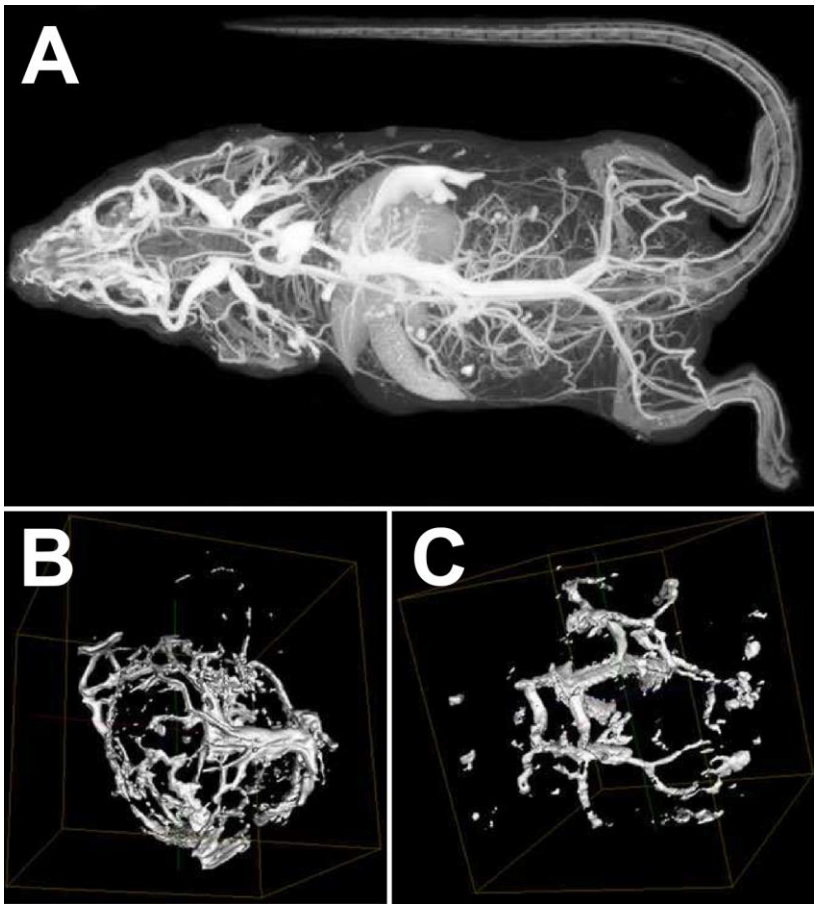

Figure 5.2: Micro-CT results of a mouse and its associated tumour mass perfused with a custom Er-based vascular perfusion contrast agent. (**A**) Maximum intensity projection (MIP) demonstrating the perfusion of a whole mouse perfused with our Er-based contrast agent. (**B**) A segmented control tumour mass with a simple threshold isosurface to display its vascular encapsulation. (**C**) A segmented tumour mass treated with an anti-VEGF drug with a simple threshold isosurface displaying the affected vascular encapsulation. Taken and modified from Lowerison *et al.*, 2017.[42]

In addition to studying angiogenesis within a tumour, we also had the opportunity to study the effects of vessel growth within the spine of genetically modified mice (CCN2-deficient) that undergo accelerated age-related intervertebral disc degeneration (IVD) (Bedore et al., submitted 2017 to Scientific Reports). Our role in the collaboration was to examine the presence of vascular invasion into the IVDs of CCN2-deficient mice. Like cartilage, IVDs are an avascular tissue requiring nutrients and oxygen through diffusion from surrounding vascularized tissues. The proximity and known function of nearby endplates to provide nutrient and oxygen[43] necessitated the need of our Er-based contrast agent and DECT to ensure the visualization of perfused vessels. However, in this case DECT was not required as vascular invasion into the IVDs originated from the spinal cord rather than the underlying bone (Figure 5.3).

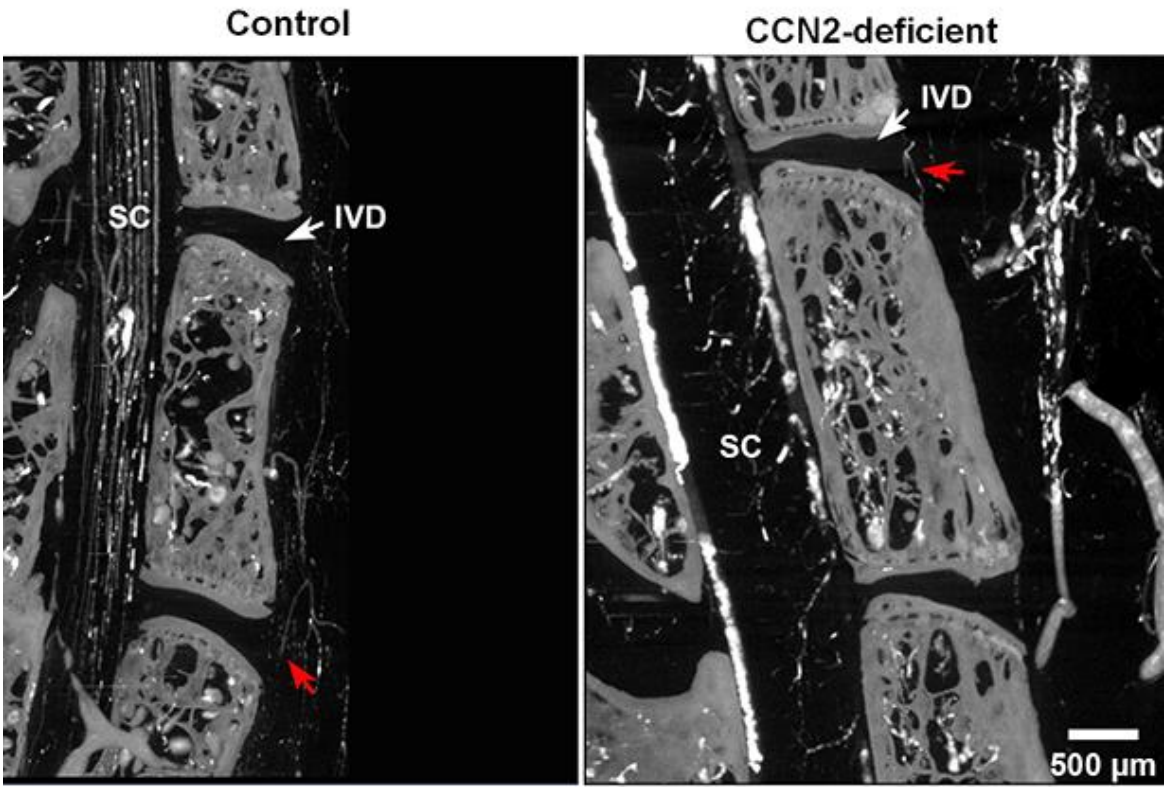

Figure 5.3: Representative thick-slice (300 µm) maximum intensity projections (MIP) of a single-energy micro-CT scan displaying the (IVD) and adjacent spinal cord (SC). A control (left) and CCN2-deficient (right) mouse were perfused with our Er-based vascular perfusion contrast agent, vertebral body microvasculature and microvasculature adjacent to the IVD space (red arrows). No overt differences in vascularity were observed within the IVD space between both the control and CCN2-deficient mice, with microvasculature at the immediate periphery of the IVD space and absence of vasculature within the IVD space. Modified from data submitted as part of a manuscript (Bedore *et al.*, 2017, Scientific Reports).

5.3 Summary

In conclusion, this thesis has described the development and implementation of a new type of endogenous vascular contrast agent for *ex vivo* use with small-animal models. The contrast agent exhibits a number of advantageous properties, including the ability to perfuse the smallest vessels, high-contrast relative to other tissues and bone, and x-ray attenuation properties that are ideally suited to dual-energy CT on laboratory scanners. This new technique has been used in a study of vascular changes in a rat model of osteoarthritis, and has also been adopted quickly in collaborative studies of the vasculature near tumours and within the spine. The combination of the erbium-based contrast agent and dual-energy scanning facilitates the automated segmentation of vessels from other tissue types (including bone), providing a potentially powerful tool for future research involving the micro-vasculature of small-animal models.

5.4 References

1. K. V. MacDonald, C. Sanmartin, K. Langlois, D. A. Marshall, Symptom onset, diagnosis and management of osteoarthritis. *Health Rep* **25**, 10-17 (2014).

2. M. A. Karsdal, M. Michaelis, C. Ladel, A. S. Siebuhr, A. R. Bihlet, J. R. Andersen, H. Guehring, C. Christiansen, A. C. Bay-Jensen, V. B. Kraus, Disease-modifying treatments for osteoarthritis (DMOADs) of the knee and hip: lessons learned from failures and opportunities for the future. *Osteoarthritis and Cartilage* **24**, 2013-2021 (2016).

3. A. Mobasheri, M. Batt, An update on the pathophysiology of osteoarthritis. *Ann Phys Rehabil Med* **59**, 333-339 (2016).

4. M. Blagojevic, C. Jinks, A. Jeffery, K. P. Jordan, Risk factors for onset of osteoarthritis of the knee in older adults: a systematic review and meta-analysis. *Osteoarthritis Cartilage* **18**, 24-33 (2010).

5. A. Shane Anderson, R. F. Loeser, Why is osteoarthritis an age-related disease? *Best Pract Res Clin Rheumatol* **24**, (2010).

6. R. Pandey, N. Kumar, S. Paroha, R. Prasad, M. Yadav, S. Jain, H. Yadav, Impact of obesity and diabetes on arthritis: An update. *Health* **5**, 14 (2013).

7. G. Schett, A. Kleyer, C. Perricone, E. Sahinbegovic, A. Iagnocco, J. Zwerina, R. Lorenzini, F. Aschenbrenner, F. Berenbaum, M. A. D'Agostino, J. Willeit, S. Kiechl, Diabetes is an independent predictor for severe osteoarthritis: results from a longitudinal cohort study. *Diabetes Care* **36**, 403-409 (2013).

8. M. M. Rahman, J. A. Kopec, J. Cibere, C. H. Goldsmith, A. H. Anis, The relationship between osteoarthritis and cardiovascular disease in a population health survey: a cross-sectional study. *BMJ Open* **3**, (2013).

9. R. Birtwhistle, R. Morkem, G. Peat, T. Williamson, M. E. Green, S. Khan, K. P. Jordan, Prevalence and management of osteoarthritis in primary care: an epidemiologic cohort study from the Canadian Primary Care Sentinel Surveillance Network. *CMAJ Open* **3**, E270-E275 (2015).

10. J. A. Buckwalter, Articular Cartilage Injuries. *Clinical Orthopaedics and Related Research* **402**, 21-37 (2002).

11. J. T. Badlani, C. Borrero, S. Golla, C. D. Harner, J. J. Irrgang, The effects of meniscus injury on the development of knee osteoarthritis: data from the osteoarthritis initiative. *Am J Sports Med* **41**, 1238-1244 (2013).

12. E. M. Roos, Joint injury causes knee osteoarthritis in young adults. *Curr Opin Rheumatol* **17**, 195-200 (2005).

13. D. M. Findlay, Vascular pathology and osteoarthritis. *Rheumatology (Oxford)* **46**, 1763-1768 (2007).

14. G. Li, J. Yin, J. Gao, T. S. Cheng, N. J. Pavlos, C. Zhang, M. H. Zheng, Subchondral bone in osteoarthritis: insight into risk factors and microstructural changes. *Arthritis Res Ther* **15**, 223-223 (2013).

15. S. Zhou, Z. Cui, J. P. Urban, Factors influencing the oxygen concentration gradient from the synovial surface of articular cartilage to the cartilage-bone interface: a modeling study. *Arthritis Rheum* **50**, 3915-3924 (2004).

16. C. Ziskoven, M. Jager, C. Zilkens, W. Bloch, K. Brixius, R. Krauspe, Oxidative stress in secondary osteoarthritis: from cartilage destruction to clinical presentation? *Orthop Rev (Pavia)* **2**, e23 (2010).

17. D. L. Batiste, A. Kirkley, S. Laverty, L. M. F. Thain, A. R. Spouge, D. W. Holdsworth, Ex vivo characterization of articular cartilage and bone lesions in a rabbit ACL transection model of osteoarthritis using MRI and micro-CT. *Osteoarthritis Cartilage* **12**, (2004).

18. D. W. Holdsworth, M. M. Thornton, Micro-CT in small animal and specimen imaging. *Trends in Biotechnology* **20**, S34-S39 (2002).

19. P. Blery, P. Pilet, A. V. Bossche, A. Thery, J. Guicheux, Y. Amouriq, F. Espitalier, N. Mathieu, P. Weiss, Vascular imaging with contrast agent in hard and soft tissues using microcomputed-tomography. *Journal of Microscopy* **262**, 40-49 (2016).

20. D. Sarhaddi, B. Poushanchi, M. Merati, C. Tchanque-Fossuo, A. Donneys, J. Baker, S. R. Buchman, Validation of Histologic Bone Analysis Following Microfil Vessel Perfusion. *Journal of histotechnology* **35**, 180-183 (2012).

21. P. V. Granton, S. I. Pollmann, N. L. Ford, M. Drangova, D. W. Holdsworth, Implementation of dual- and triple-energy cone-beam micro-CT for postreconstruction material decomposition. *Med Phys* **35**, 5030-5042 (2008).

22. D. D. McErlain, C. T. Appleton, R. B. Litchfield, V. Pitelka, J. L. Henry, S. M. Bernier, F. Beier, D. W. Holdsworth, Study of subchondral bone adaptations in a rodent surgical model of OA using in vivo micro-computed tomography. *Osteoarthritis Cartilage* **16**, 458-469 (2008).

23. C. T. Appleton, D. D. McErlain, J. L. Henry, D. W. Holdsworth, F. Beier, Molecular and histological analysis of a new rat model of experimental knee osteoarthritis. *Ann N Y Acad Sci* **1117**, 165-174 (2007).

24. C. Cruje, J. J. Tse, D. W. Holdsworth, E. R. Gillies, M. Drangova, in *SPIE Medical Imaging*. (SPIE, 2017), vol. 10132, pp. 6.

25. H.-Y. Kim, J. O. Sofo, D. Velegol, M. W. Cole, A. A. Lucas, Van der Waals Dispersion Forces between Dielectric Nanoclusters. *Langmuir* **23**, 1735-1740 (2007).

26. N. M. Kovalchuk, V. M. Starov, Aggregation in colloidal suspensions: Effect of colloidal forces and hydrodynamic interactions. *Advances in Colloid and Interface Science* **179–182**, 99-106 (2012).

27. J. J. Tse, J. Dunmore-Buyze, M. Drangova, D. W. Holdsworth, Erbium-based perfusion contrast agent for small-animal microvessel imaging. *Contrast Media & Molecular Imaging*, In Press (2017).

28. S. R. Cherry, Multimodality Imaging: Beyond PET/CT and SPECT/CT. *Seminars in Nuclear Medicine* **39**, 348-353 (2009).

29. H. N. Cardinal, D. W. Holdsworth, M. Drangova, B. B. Hobbs, A. Fenster, Experimental and theoretical x-ray imaging performance comparison of iodine and lanthanide contrast agents. *Medical Physics* **20**, 15-31 (1993).

30. J. J. Tse, J. Dunmore-Buyze, M. Drangova, D. W. Holdsworth, Dual-Energy Computed Tomography for a Gantry-Based Pre-Clinical Cone Beam Micro-CT Scanner. *SPIE Medical Imaging* **Submitted**, (2017).

31. L. Li, R. Li, S. Zhang, T. Zhao, Z. Chen, A dynamic material discrimination algorithm for dual MV energy X-ray digital radiography. *Applied Radiation and Isotopes* **114**, 188-195 (2016).

32. F. Liu, Q. Yang, W. Cong, G. Wang, Dynamic Bowtie Filter for Cone-Beam/Multi-Slice CT. *PLoS One* **9**, e103054 (2014).

33. J. M. Boone, Method for evaluating bow tie filter angle-dependent attenuation in CT: Theory and simulation results. *Medical Physics* **37**, 40-48 (2010).

34. D. T. Felson, J. Niu, T. Neogi, Synovitis and the risk of knee osteoarthritis: the MOST Study. *Osteoarthritis Cartilage* **24**, (2016).

35. T. Hügle, J. Geurts, What drives osteoarthritis?—synovial versus subchondral bone pathology. *Rheumatology (Oxford)* **56**, 1461-1471 (2017).

36. R. K. June, R. Liu-Bryan, F. Long, T. M. Griffin, Emerging role of metabolic signaling in synovial joint remodeling and osteoarthritis. *Journal of Orthopaedic Research* **34**, 2048-2058 (2016).

37. M. Montgomery, B. Zhang, M. Radisic, Cardiac Tissue Vascularization. *Journal of Cardiovascular Pharmacology and Therapeutics* **19**, 382-393 (2014).

38. M. Laroche, V. Pécourneau, H. Blain, V. Breuil, R. Chapurlat, B. Cortet, B. Sutter, Y. Degboe, Osteoporosis and ischemic cardiovascular disease. *Joint Bone Spine* **84**, 427-432 (2017).

39. A. Jazwa, U. Florczyk, A. Grochot-Przeczek, B. Krist, A. Loboda, A. Jozkowicz, J. Dulak, Limb ischemia and vessel regeneration: Is there a role for VEGF? *Vascular Pharmacology* **86**, 18-30 (2016).

40. P. M. Hoff, K. K. Machado, Role of angiogenesis in the pathogenesis of cancer. *Cancer Treatment Reviews* **38**, 825-833 (2012).

41. D. A. Greenberg, K. Jin, From angiogenesis to neuropathology. *Nature* **438**, 954-959 (2005).

42. M. R. Lowerison, J. J. Tse, M. N. Hague, A. F. Chambers, D. W. Holdsworth, J. C. Lacefield, Compound speckle model detects anti-angiogenic tumor response in preclinical nonlinear contrast-enhanced ultrasonography. *Medical Physics* **44**, 99-111 (2017).

43. J. P. Urban, S. Smith, J. C. Fairbank, Nutrition of the intervertebral disc. *Spine (Phila Pa 1976)* **29**, 2700-2709 (2004).

Appendix A

Additional Analysis for the Resuspension of a Two-Year Old Er-Based Vascular Perfusion Contrast Agent

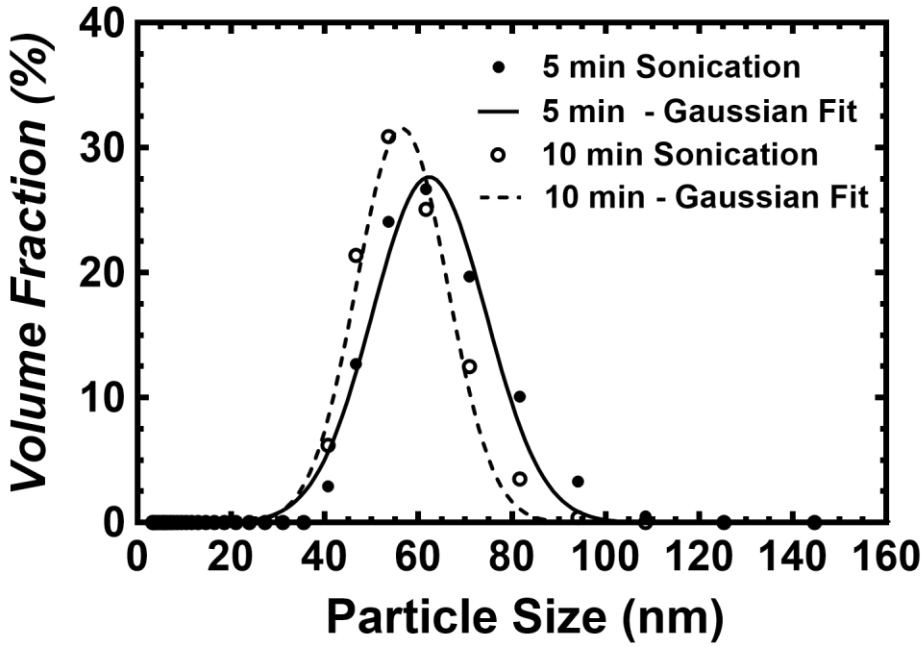

Figure A.1: DLS measurements of particle size distribution of a two-year old prepared Er-based suspension that was sonicated for either 5 or 10 minutes prior to measurement.

Appendix B

Animal Ethics Approval

Western

2015-018::1:

AUP Number: 2015-018
AUP Title: TGFα/EGFR signaling in osteoarthritis
Yearly Renewal Date: 07/01/2016

The YEARLY RENEWAL to Animal Use Protocol (AUP) 2015-018 has been approved, and will be approved for one year following the above review date.

1. This AUP number must be indicated when ordering animals for this project.
2. Animals for other projects may not be ordered under this AUP number.
3. Purchases of animals other than through this system must be cleared through the ACVS office.
   Health certificates will be required.

REQUIREMENTS/COMMENTS
Please ensure that individual(s) performing procedures on live animals, as described in this protocol, are familiar with the contents of this document.

The holder of this Animal Use Protocol is responsible to ensure that all associated safety components (biosafety, radiation safety, general laboratory safety) comply with institutional safety standards and have received all necessary approvals. Please consult directly with your institutional safety officers.

Submitted by: Kinchlea, Will D
on behalf of the Animal Use Subcommittee

The University *of* Western Ontario
Animal Use Subcommittee / University Council on Animal Care
Health Sciences Centre, ● London, Ontario ● CANADA – N6A 5C1
PH: 519-661-2111 ext. 86768 ● FL 519-661-2028
Email: auspc@uwo.ca ● http://www.uwo.ca/animal/website/

Appendix C

Dual-Energy Computed Tomography Decomposition Algorithm Detailed Explanation

The implementation of dual-energy computed tomography (DECT) decompositions within this Ph.D. thesis has been previously outlined and described in greater detail by Granton *et al*., 2008. However, briefly, the decomposition algorithm relies on the solution of the following three equations:

eq. 1 $$\mu_{Soft\ Tissue(HighE)} f_{Soft\ Tissue} + \mu_{Bone(HighE)} f_{Bone} + \mu_{Vessel(HighE)} f_{Vessel} = \mu_{HighE}$$

eq. 2 $$\mu_{Soft\ Tissue(LowE)} f_{Soft\ Tissue} + \mu_{Bone(LowE)} f_{Bone} + \mu_{Vessel(LowE)} f_{Vessel} = \mu_{LowE}$$

eq. 3 $$f_{Soft\ Tissue} + f_{Bone} + f_{Vessel} = \mu_{HighE}$$

From *eq. 1* and *eq. 2*, the observed attenuation coefficient recorded within each individual voxel in the acquired low- (μ_{LowE}) and high- (μ_{HighE}) energy volumes is comprised of the fractional contribution of three materials of interest (*i.e*. $f_{Soft\ Tissue}$, f_{Bone} , and f_{Vessel}) and their respective attenuation coefficient at that acquired x-ray energy (*i.e*. $\mu_{Soft\ Tissue(Low/HighE).}$ $\mu_{Bone(Low/HighE)}$, and $\mu_{Vessel(Low/HighE)}$). In *eq. 3* we assume that a voxel can only be comprised of the fractional contribution from either soft tissue, bone, or vessel and that the sum of their fractional contribution must equal 1 (*i.e*. 100%).

The μ values, within *eq. 1* and *eq. 2*, for each tissue were acquired from the mean CT value in Hounsfield units (HU) from 500 × 500 × 500 μm regions-of-interest (ROI), in both low- and high-energy acquired volumes, from areas of pure soft tissue, bone, and vessel. The mean CT value was used, as this value is linearly proportional to the tissue's respective attenuation coefficient. The initial six CT values (*i.e*. "seed values") inputted into *eq. 1* and *2* are highly dependent on known areas of pure tissues. Using improper seed values will result in non-ideal decompositions (*i.e*. misclassified voxels, Fig. 3.5 and 3.8), visualized as components bleeding into one another (Fig. 3.7 and 3.9). To optimize the six seed values – resulting in a highly accurate decomposition – an iterative approach was taken.

The initial six seed values were chosen by recording the mean value from 500 × 500 × 500 μm ROIs within areas of known soft tissue (bicep femoris), bone (cortical bone), and vessel (femoral artery). Unfortunately, as Er-perfused microvessels are located

throughout the bicep femoris and cortical bone, the recorded CT values will be higher than expected. The resulting automatically decomposed volumes will contain many misclassified voxels. Thus, to further finetune the seed values and obtain more accurate CT values for non-vascularized soft tissue and bone, a mask for each tissue was generated for each decomposed volume. The separate "tissue masks" were obtained by choosing a threshold value within each decomposed volume above the value of tissues "bleeding" into that volume. A custom in-house Unix-based script would then provide a mean value of all the voxels within each decomposed value that was above the threshold value, providing a new seed value for said tissue component. This iterative approach was performed a max number of ten times for each tissue at both low- and high-energy until an ideal set of six seed values was obtained (Table 3.1), resulting in decomposed volumes of solely soft tissue, bone, and vessel were obtained (Fig. 3.4). Therefore, all that remains from *eq. 1-3* are the voxel volume fractions of soft tissue, bone, and vessel (*i.e.* $f_{Soft\ Tissue}$, f_{Bone}, and f_{Vessel}).

To determine the voxel volume fractions of each tissue, we employed a matrix factorization approach to solve a system of linear equations (*i.e. eq. 1-3*). The results of these calculations (performed for each voxel within the acquired low- and high-energy volumes), are individual volumes of the three materials-of-interest (*i.e.* soft tissue, bone, and vessel). Within each decomposed volume, greyscale values (0 – 10,000) of individual voxels represented the voxel volume fraction or percent contribution (0 – 100%) of said component to that specific voxel. Thus, the decomposition algorithm resulted in three tissue-distinct 3D volumes, where greyscale values represented the percent contribution of a tissue on a voxel.

Appendix D

Copyright Permissions

SPRINGER NATURE LICENSE
TERMS AND CONDITIONS

Dec 13, 2017

This Agreement between Robarts Research Institute ("You") and Springer Nature ("Springer Nature") consists of your license details and the terms and conditions provided by Springer Nature and Copyright Clearance Center.

License Number	4247210107509
License date	Dec 13, 2017
Licensed Content Publisher	Springer Nature
Licensed Content Publication	Nature Reviews Rheumatology
Licensed Content Title	The individual and socioeconomic impact of osteoarthritis
Licensed Content Author	David J. Hunter, Deborah Schofield, Emily Callander
Licensed Content Date	Mar 25, 2014
Licensed Content Volume	10
Licensed Content Issue	7
Type of Use	Thesis/Dissertation
Requestor type	academic/university or research institute
Format	print and electronic
Portion	figures/tables/illustrations
Number of figures/tables/illustrations	1
High-res required	no
Will you be translating?	no
Circulation/distribution	<501
Author of this Springer Nature content	no
Title	Mr.
Instructor name	Justin Tse
Institution name	Western University
Expected presentation date	Dec 2017
Portions	Figure 3: Distribution of direct costs of OA by type. To be used in my thesis / dissertation
Requestor Location	Robarts Research Institute 1151 Richmond Street North Dock 50 London, ON N6A5B7 Canada Attn: Robarts Research Institute
Billing Type	Invoice
Billing Address	Robarts Research Institute 1151 Richmond Street North Dock 50

London, ON N6A5B7
Canada
Attn: Robarts Research Institute

Total 0.00 CAD

Terms and Conditions

Springer Nature Terms and Conditions for RightsLink Permissions

Springer Customer Service Centre GmbH (the Licensor) hereby grants you a non-exclusive, world-wide licence to reproduce the material and for the purpose and requirements specified in the attached copy of your order form, and for no other use, subject to the conditions below:

1. The Licensor warrants that it has, to the best of its knowledge, the rights to license reuse of this material. However, you should ensure that the material you are requesting is original to the Licensor and does not carry the copyright of another entity (as credited in the published version).

   If the credit line on any part of the material you have requested indicates that it was reprinted or adapted with permission from another source, then you should also seek permission from that source to reuse the material.

2. Where **print only** permission has been granted for a fee, separate permission must be obtained for any additional electronic re-use.

3. Permission granted **free of charge** for material in print is also usually granted for any electronic version of that work, provided that the material is incidental to your work as a whole and that the electronic version is essentially equivalent to, or substitutes for, the print version.

4. A licence for 'post on a website' is valid for 12 months from the licence date. This licence does not cover use of full text articles on websites.

5. Where **'reuse in a dissertation/thesis'** has been selected the following terms apply: Print rights for up to 100 copies, electronic rights for use only on a personal website or institutional repository as defined by the Sherpa guideline (www.sherpa.ac.uk/romeo/).

6. Permission granted for books and journals is granted for the lifetime of the first edition and does not apply to second and subsequent editions (except where the first edition permission was granted free of charge or for signatories to the STM Permissions Guidelines http://www.stm-assoc.org/copyright-legal-affairs/permissions/permissions-guidelines/), and does not apply for editions in other languages unless additional translation rights have been granted separately in the licence.

7. Rights for additional components such as custom editions and derivatives require additional permission and may be subject to an additional fee. Please apply to Journalpermissions@springernature.com/bookpermissions@springernature.com for these rights.

8. The Licensor's permission must be acknowledged next to the licensed material in print. In electronic form, this acknowledgement must be visible at the same time as the figures/tables/illustrations or abstract, and must be hyperlinked to the journal/book's homepage. Our required acknowledgement format is in the Appendix below.

9. Use of the material for incidental promotional use, minor editing privileges (this does not include cropping, adapting, omitting material or any other changes that affect the meaning, intention or moral rights of the author) and copies for the disabled are permitted under this licence.

10. Minor adaptations of single figures (changes of format, colour and style) do not require the Licensor's approval. However, the adaptation should be credited as shown in Appendix below.

Appendix — Acknowledgements:

For Journal Content:
Reprinted by permission from [**the Licensor**]: [**Journal Publisher** (e.g. Nature/Springer/Palgrave)] [**JOURNAL NAME**] [**REFERENCE CITATION** (Article name, Author(s) Name), [**COPYRIGHT**] (year of publication)

For **Advance Online Publication papers:**
Reprinted by permission from [**the Licensor**]: [**Journal Publisher** (e.g. Nature/Springer/Palgrave)] [**JOURNAL NAME**] [**REFERENCE CITATION** (Article name, Author(s) Name), [**COPYRIGHT**] (year of publication), advance online publication, day month year (doi: 10.1038/sj.[JOURNAL ACRONYM].)

For Adaptations/Translations:
Adapted/Translated by permission from [**the Licensor**]: [**Journal Publisher** (e.g. Nature/Springer/Palgrave)] [**JOURNAL NAME**] [**REFERENCE CITATION** (Article name, Author(s) Name), [**COPYRIGHT**] (year of publication)

Note: For any republication from the British Journal of Cancer, the following credit line style applies:

Reprinted/adapted/translated by permission from [**the Licensor**]: on behalf of Cancer Research UK: : [**Journal Publisher** (e.g. Nature/Springer/Palgrave)] [**JOURNAL NAME**] [**REFERENCE CITATION** (Article name, Author(s) Name), [**COPYRIGHT]** (year of publication)

For **Advance Online Publication** papers:
Reprinted by permission from The [**the Licensor**]: on behalf of Cancer Research UK: [**Journal Publisher** (e.g. Nature/Springer/Palgrave)] [**JOURNAL NAME**] [**REFERENCE CITATION** (Article name, Author(s) Name), [**COPYRIGHT**] (year of publication), advance online publication, day month year (doi: 10.1038/sj.[JOURNAL ACRONYM])

For Book content:
Reprinted/adapted by permission from [**the Licensor**]: [**Book Publisher** (e.g. Palgrave Macmillan, Springer etc) [**Book Title**] by [**Book author**(s)] [**COPYRIGHT**] (year of publication)

Other Conditions:

Version 1.0

OXFORD UNIVERSITY PRESS LICENSE TERMS AND CONDITIONS

Dec 13, 2017

This Agreement between Robarts Research Institute ("You") and Oxford University Press ("Oxford University Press") consists of your license details and the terms and conditions provided by Oxford University Press and Copyright Clearance Center.

License Number	4247210741486
License date	Dec 13, 2017
Licensed content publisher	Oxford University Press
Licensed content publication	Rheumatology
Licensed content title	Vascular pathology and osteoarthritis
Licensed content author	Findlay, D. M.
Licensed content date	Aug 10, 2007
Type of Use	Thesis/Dissertation
Institution name	
Title of your work	Mr.
Publisher of your work	Western University
Expected publication date	Dec 2017
Permissions cost	0.00 CAD
Value added tax	0.00 CAD
Total	0.00 CAD
Requestor Location	Robarts Research Institute 1151 Richmond Street North Dock 50 London, ON N6A5B7 Canada Attn: Robarts Research Institute
Publisher Tax ID	GB125506730
Billing Type	Invoice
Billing Address	Robarts Research Institute 1151 Richmond Street North Dock 50 London, ON N6A5B7 Canada Attn: Robarts Research Institute
Total	0.00 CAD
Terms and Conditions	

STANDARD TERMS AND CONDITIONS FOR REPRODUCTION OF MATERIAL FROM AN OXFORD UNIVERSITY PRESS JOURNAL

1. Use of the material is restricted to the type of use specified in your order details.
2. This permission covers the use of the material in the English language in the following territory: world. If you have requested additional permission to translate this material, the

terms and conditions of this reuse will be set out in clause 12.
3. This permission is limited to the particular use authorized in (1) above and does not allow you to sanction its use elsewhere in any other format other than specified above, nor does it apply to quotations, images, artistic works etc that have been reproduced from other sources which may be part of the material to be used.
4. No alteration, omission or addition is made to the material without our written consent. Permission must be re-cleared with Oxford University Press if/when you decide to reprint.
5. The following credit line appears wherever the material is used: author, title, journal, year, volume, issue number, pagination, by permission of Oxford University Press or the sponsoring society if the journal is a society journal. Where a journal is being published on behalf of a learned society, the details of that society must be included in the credit line.
6. For the reproduction of a full article from an Oxford University Press journal for whatever purpose, the corresponding author of the material concerned should be informed of the proposed use. Contact details for the corresponding authors of all Oxford University Press journal contact can be found alongside either the abstract or full text of the article concerned, accessible from www.oxfordjournals.org Should there be a problem clearing these rights, please contact journals.permissions@oup.com
7. If the credit line or acknowledgement in our publication indicates that any of the figures, images or photos was reproduced, drawn or modified from an earlier source it will be necessary for you to clear this permission with the original publisher as well. If this permission has not been obtained, please note that this material cannot be included in your publication/photocopies.
8. While you may exercise the rights licensed immediately upon issuance of the license at the end of the licensing process for the transaction, provided that you have disclosed complete and accurate details of your proposed use, no license is finally effective unless and until full payment is received from you (either by Oxford University Press or by Copyright Clearance Center (CCC)) as provided in CCC's Billing and Payment terms and conditions. If full payment is not received on a timely basis, then any license preliminarily granted shall be deemed automatically revoked and shall be void as if never granted. Further, in the event that you breach any of these terms and conditions or any of CCC's Billing and Payment terms and conditions, the license is automatically revoked and shall be void as if never granted. Use of materials as described in a revoked license, as well as any use of the materials beyond the scope of an unrevoked license, may constitute copyright infringement and Oxford University Press reserves the right to take any and all action to protect its copyright in the materials.
9. This license is personal to you and may not be sublicensed, assigned or transferred by you to any other person without Oxford University Press's written permission.
10. Oxford University Press reserves all rights not specifically granted in the combination of (i) the license details provided by you and accepted in the course of this licensing transaction, (ii) these terms and conditions and (iii) CCC's Billing and Payment terms and conditions.
11. You hereby indemnify and agree to hold harmless Oxford University Press and CCC, and their respective officers, directors, employs and agents, from and against any and all claims arising out of your use of the licensed material other than as specifically authorized pursuant to this license.
12. Other Terms and Conditions:
v1.4

ELSEVIER LICENSE
TERMS AND CONDITIONS

Dec 14, 2017

This Agreement between Robarts Research Institute ("You") and Elsevier ("Elsevier") consists of your license details and the terms and conditions provided by Elsevier and Copyright Clearance Center.

License Number	4247691316341
License date	Dec 14, 2017
Licensed Content Publisher	Elsevier
Licensed Content Publication	Clinical Radiology
Licensed Content Title	Dual-energy CT angiography of pelvic and lower extremity arteries: dual-energy bone subtraction versus manual bone subtraction
Licensed Content Author	S. Yamamoto,J. McWilliams,C. Arellano,W. Marfori,W. Cheng,T. Mcnamara,W.J. Quinones-Baldrich,S.G. Ruehm
Licensed Content Date	Nov 1, 2009
Licensed Content Volume	64
Licensed Content Issue	11
Licensed Content Pages	9
Start Page	1088
End Page	1096
Type of Use	reuse in a thesis/dissertation
Intended publisher of new work	other
Portion	figures/tables/illustrations
Number of figures/tables/illustrations	2
Format	both print and electronic
Are you the author of this Elsevier article?	No
Will you be translating?	No
Original figure numbers	Figure 1a and 2a
Title of your thesis/dissertation	Mr.
Publisher of new work	Western University
Author of new work	Justin Tse
Expected completion date	Dec 2017
Estimated size (number of pages)	1
Requestor Location	Robarts Research Institute 1151 Richmond Street North Dock 50 London, ON N6A5B7

Canada
Attn: Robarts Research Institute

Total 0.00 CAD

Terms and Conditions

INTRODUCTION

1. The publisher for this copyrighted material is Elsevier. By clicking "accept" in connection with completing this licensing transaction, you agree that the following terms and conditions apply to this transaction (along with the Billing and Payment terms and conditions established by Copyright Clearance Center, Inc. ("CCC"), at the time that you opened your Rightslink account and that are available at any time at http://myaccount.copyright.com).

GENERAL TERMS

2. Elsevier hereby grants you permission to reproduce the aforementioned material subject to the terms and conditions indicated.
3. Acknowledgement: If any part of the material to be used (for example, figures) has appeared in our publication with credit or acknowledgement to another source, permission must also be sought from that source. If such permission is not obtained then that material may not be included in your publication/copies. Suitable acknowledgement to the source must be made, either as a footnote or in a reference list at the end of your publication, as follows:
"Reprinted from Publication title, Vol /edition number, Author(s), Title of article / title of chapter, Pages No., Copyright (Year), with permission from Elsevier [OR APPLICABLE SOCIETY COPYRIGHT OWNER]." Also Lancet special credit - "Reprinted from The Lancet, Vol. number, Author(s), Title of article, Pages No., Copyright (Year), with permission from Elsevier."
4. Reproduction of this material is confined to the purpose and/or media for which permission is hereby given.
5. Altering/Modifying Material: Not Permitted. However figures and illustrations may be altered/adapted minimally to serve your work. Any other abbreviations, additions, deletions and/or any other alterations shall be made only with prior written authorization of Elsevier Ltd. (Please contact Elsevier at permissions@elsevier.com). No modifications can be made to any Lancet figures/tables and they must be reproduced in full.
6. If the permission fee for the requested use of our material is waived in this instance, please be advised that your future requests for Elsevier materials may attract a fee.
7. Reservation of Rights: Publisher reserves all rights not specifically granted in the combination of (i) the license details provided by you and accepted in the course of this licensing transaction, (ii) these terms and conditions and (iii) CCC's Billing and Payment terms and conditions.
8. License Contingent Upon Payment: While you may exercise the rights licensed immediately upon issuance of the license at the end of the licensing process for the transaction, provided that you have disclosed complete and accurate details of your proposed use, no license is finally effective unless and until full payment is received from you (either by publisher or by CCC) as provided in CCC's Billing and Payment terms and conditions. If full payment is not received on a timely basis, then any license preliminarily granted shall be deemed automatically revoked and shall be void as if never granted. Further, in the event that you breach any of these terms and conditions or any of CCC's Billing and Payment terms and conditions, the license is automatically revoked and shall be void as if never granted. Use of materials as described in a revoked license, as well as any use of the materials beyond the scope of an unrevoked license, may constitute copyright infringement and publisher reserves the right to take any and all action to protect its copyright in the materials.
9. Warranties: Publisher makes no representations or warranties with respect to the licensed material.

10. Indemnity: You hereby indemnify and agree to hold harmless publisher and CCC, and their respective officers, directors, employees and agents, from and against any and all claims arising out of your use of the licensed material other than as specifically authorized pursuant to this license.
11. No Transfer of License: This license is personal to you and may not be sublicensed, assigned, or transferred by you to any other person without publisher's written permission.
12. No Amendment Except in Writing: This license may not be amended except in a writing signed by both parties (or, in the case of publisher, by CCC on publisher's behalf).
13. Objection to Contrary Terms: Publisher hereby objects to any terms contained in any purchase order, acknowledgment, check endorsement or other writing prepared by you, which terms are inconsistent with these terms and conditions or CCC's Billing and Payment terms and conditions. These terms and conditions, together with CCC's Billing and Payment terms and conditions (which are incorporated herein), comprise the entire agreement between you and publisher (and CCC) concerning this licensing transaction. In the event of any conflict between your obligations established by these terms and conditions and those established by CCC's Billing and Payment terms and conditions, these terms and conditions shall control.
14. Revocation: Elsevier or Copyright Clearance Center may deny the permissions described in this License at their sole discretion, for any reason or no reason, with a full refund payable to you. Notice of such denial will be made using the contact information provided by you. Failure to receive such notice will not alter or invalidate the denial. In no event will Elsevier or Copyright Clearance Center be responsible or liable for any costs, expenses or damage incurred by you as a result of a denial of your permission request, other than a refund of the amount(s) paid by you to Elsevier and/or Copyright Clearance Center for denied permissions.

LIMITED LICENSE

The following terms and conditions apply only to specific license types:
15. **Translation**: This permission is granted for non-exclusive world **English** rights only unless your license was granted for translation rights. If you licensed translation rights you may only translate this content into the languages you requested. A professional translator must perform all translations and reproduce the content word for word preserving the integrity of the article.
16. **Posting licensed content on any Website**: The following terms and conditions apply as follows: Licensing material from an Elsevier journal: All content posted to the web site must maintain the copyright information line on the bottom of each image; A hyper-text must be included to the Homepage of the journal from which you are licensing at http://www.sciencedirect.com/science/journal/xxxxx or the Elsevier homepage for books at http://www.elsevier.com; Central Storage: This license does not include permission for a scanned version of the material to be stored in a central repository such as that provided by Heron/XanEdu.
Licensing material from an Elsevier book: A hyper-text link must be included to the Elsevier homepage at http://www.elsevier.com . All content posted to the web site must maintain the copyright information line on the bottom of each image.

Posting licensed content on Electronic reserve: In addition to the above the following clauses are applicable: The web site must be password-protected and made available only to bona fide students registered on a relevant course. This permission is granted for 1 year only. You may obtain a new license for future website posting.
17. **For journal authors:** the following clauses are applicable in addition to the above:
Preprints:
A preprint is an author's own write-up of research results and analysis, it has not been peer-reviewed, nor has it had any other value added to it by a publisher (such as formatting, copyright, technical enhancement etc.).

Authors can share their preprints anywhere at any time. Preprints should not be added to or enhanced in any way in order to appear more like, or to substitute for, the final versions of articles however authors can update their preprints on arXiv or RePEc with their Accepted Author Manuscript (see below).
If accepted for publication, we encourage authors to link from the preprint to their formal publication via its DOI. Millions of researchers have access to the formal publications on ScienceDirect, and so links will help users to find, access, cite and use the best available version. Please note that Cell Press, The Lancet and some society-owned have different preprint policies. Information on these policies is available on the journal homepage.
Accepted Author Manuscripts: An accepted author manuscript is the manuscript of an article that has been accepted for publication and which typically includes author-incorporated changes suggested during submission, peer review and editor-author communications.
Authors can share their accepted author manuscript:

- immediately
    - via their non-commercial person homepage or blog
    - by updating a preprint in arXiv or RePEc with the accepted manuscript
    - via their research institute or institutional repository for internal institutional uses or as part of an invitation-only research collaboration work-group
    - directly by providing copies to their students or to research collaborators for their personal use
    - for private scholarly sharing as part of an invitation-only work group on commercial sites with which Elsevier has an agreement
- After the embargo period
    - via non-commercial hosting platforms such as their institutional repository
    - via commercial sites with which Elsevier has an agreement

In all cases accepted manuscripts should:

- link to the formal publication via its DOI
- bear a CC-BY-NC-ND license - this is easy to do
- if aggregated with other manuscripts, for example in a repository or other site, be shared in alignment with our hosting policy not be added to or enhanced in any way to appear more like, or to substitute for, the published journal article.

Published journal article (JPA): A published journal article (PJA) is the definitive final record of published research that appears or will appear in the journal and embodies all value-adding publishing activities including peer review co-ordination, copy-editing, formatting, (if relevant) pagination and online enrichment.
Policies for sharing publishing journal articles differ for subscription and gold open access articles:
Subscription Articles: If you are an author, please share a link to your article rather than the full-text. Millions of researchers have access to the formal publications on ScienceDirect, and so links will help your users to find, access, cite, and use the best available version.
Theses and dissertations which contain embedded PJAs as part of the formal submission can be posted publicly by the awarding institution with DOI links back to the formal publications on ScienceDirect.
If you are affiliated with a library that subscribes to ScienceDirect you have additional private sharing rights for others' research accessed under that agreement. This includes use for classroom teaching and internal training at the institution (including use in course packs and courseware programs), and inclusion of the article for grant funding purposes.
Gold Open Access Articles: May be shared according to the author-selected end-user license and should contain a CrossMark logo, the end user license, and a DOI link to the

formal publication on ScienceDirect.
Please refer to Elsevier's posting policy for further information.
18. **For book authors** the following clauses are applicable in addition to the above: Authors are permitted to place a brief summary of their work online only. You are not allowed to download and post the published electronic version of your chapter, nor may you scan the printed edition to create an electronic version. **Posting to a repository:** Authors are permitted to post a summary of their chapter only in their institution's repository.
19. **Thesis/Dissertation**: If your license is for use in a thesis/dissertation your thesis may be submitted to your institution in either print or electronic form. Should your thesis be published commercially, please reapply for permission. These requirements include permission for the Library and Archives of Canada to supply single copies, on demand, of the complete thesis and include permission for Proquest/UMI to supply single copies, on demand, of the complete thesis. Should your thesis be published commercially, please reapply for permission. Theses and dissertations which contain embedded PJAs as part of the formal submission can be posted publicly by the awarding institution with DOI links back to the formal publications on ScienceDirect.

Elsevier Open Access Terms and Conditions
You can publish open access with Elsevier in hundreds of open access journals or in nearly 2000 established subscription journals that support open access publishing. Permitted third party re-use of these open access articles is defined by the author's choice of Creative Commons user license. See our open access license policy for more information.
Terms & Conditions applicable to all Open Access articles published with Elsevier:
Any reuse of the article must not represent the author as endorsing the adaptation of the article nor should the article be modified in such a way as to damage the author's honour or reputation. If any changes have been made, such changes must be clearly indicated.
The author(s) must be appropriately credited and we ask that you include the end user license and a DOI link to the formal publication on ScienceDirect.
If any part of the material to be used (for example, figures) has appeared in our publication with credit or acknowledgement to another source it is the responsibility of the user to ensure their reuse complies with the terms and conditions determined by the rights holder.
Additional Terms & Conditions applicable to each Creative Commons user license:
CC BY: The CC-BY license allows users to copy, to create extracts, abstracts and new works from the Article, to alter and revise the Article and to make commercial use of the Article (including reuse and/or resale of the Article by commercial entities), provided the user gives appropriate credit (with a link to the formal publication through the relevant DOI), provides a link to the license, indicates if changes were made and the licensor is not represented as endorsing the use made of the work. The full details of the license are available at http://creativecommons.org/licenses/by/4.0.
CC BY NC SA: The CC BY-NC-SA license allows users to copy, to create extracts, abstracts and new works from the Article, to alter and revise the Article, provided this is not done for commercial purposes, and that the user gives appropriate credit (with a link to the formal publication through the relevant DOI), provides a link to the license, indicates if changes were made and the licensor is not represented as endorsing the use made of the work. Further, any new works must be made available on the same conditions. The full details of the license are available at http://creativecommons.org/licenses/by-nc-sa/4.0.
CC BY NC ND: The CC BY-NC-ND license allows users to copy and distribute the Article, provided this is not done for commercial purposes and further does not permit distribution of the Article if it is changed or edited in any way, and provided the user gives appropriate credit (with a link to the formal publication through the relevant DOI), provides a link to the license, and that the licensor is not represented as endorsing the use made of the work. The full details of the license are available at http://creativecommons.org/licenses/by-nc-nd/4.0.
Any commercial reuse of Open Access articles published with a CC BY NC SA or CC BY NC ND license requires permission from Elsevier and will be subject to a fee.

Commercial reuse includes:

- Associating advertising with the full text of the Article
- Charging fees for document delivery or access
- Article aggregation
- Systematic distribution via e-mail lists or share buttons

Posting or linking by commercial companies for use by customers of those companies.

20. **Other Conditions**:

v1.9

JOHN WILEY AND SONS LICENSE TERMS AND CONDITIONS

Dec 13, 2017

This Agreement between Robarts Research Institute ("You") and John Wiley and Sons ("John Wiley and Sons") consists of your license details and the terms and conditions provided by John Wiley and Sons and Copyright Clearance Center.

License Number	4247220161951
License date	Dec 13, 2017
Licensed Content Publisher	John Wiley and Sons
Licensed Content Publication	Medical Physics
Licensed Content Title	Compound speckle model detects anti-angiogenic tumor response in preclinical nonlinear contrast-enhanced ultrasonography
Licensed Content Author	Matthew R. Lowerison,Justin J. Tse,M. Nicole Hague,Ann F. Chambers,David W. Holdsworth,James C. Lacefield
Licensed Content Date	Jan 19, 2017
Licensed Content Pages	13
Type of use	Dissertation/Thesis
Requestor type	University/Academic
Format	Print and electronic
Portion	Figure/table
Number of figures/tables	1
Original Wiley figure/table number(s)	Figure 2a-d
Will you be translating?	No
Title of your thesis / dissertation	Mr.
Expected completion date	Dec 2017
Expected size (number of pages)	1
Requestor Location	Robarts Research Institute 1151 Richmond Street North Dock 50 London, ON N6A5B7 Canada Attn: Robarts Research Institute
Publisher Tax ID	EU826007151
Billing Type	Invoice
Billing Address	Robarts Research Institute 1151 Richmond Street North Dock 50 London, ON N6A5B7 Canada Attn: Robarts Research Institute

Total 0.00 CAD

Terms and Conditions

TERMS AND CONDITIONS

This copyrighted material is owned by or exclusively licensed to John Wiley & Sons, Inc. or one of its group companies (each a"Wiley Company") or handled on behalf of a society with which a Wiley Company has exclusive publishing rights in relation to a particular work (collectively "WILEY"). By clicking "accept" in connection with completing this licensing transaction, you agree that the following terms and conditions apply to this transaction (along with the billing and payment terms and conditions established by the Copyright Clearance Center Inc., ("CCC's Billing and Payment terms and conditions"), at the time that you opened your RightsLink account (these are available at any time at http://myaccount.copyright.com).

Terms and Conditions

- The materials you have requested permission to reproduce or reuse (the "Wiley Materials") are protected by copyright.

- You are hereby granted a personal, non-exclusive, non-sub licensable (on a stand-alone basis), non-transferable, worldwide, limited license to reproduce the Wiley Materials for the purpose specified in the licensing process. This license, **and any CONTENT (PDF or image file) purchased as part of your order,** is for a one-time use only and limited to any maximum distribution number specified in the license. The first instance of republication or reuse granted by this license must be completed within two years of the date of the grant of this license (although copies prepared before the end date may be distributed thereafter). The Wiley Materials shall not be used in any other manner or for any other purpose, beyond what is granted in the license. Permission is granted subject to an appropriate acknowledgement given to the author, title of the material/book/journal and the publisher. You shall also duplicate the copyright notice that appears in the Wiley publication in your use of the Wiley Material. Permission is also granted on the understanding that nowhere in the text is a previously published source acknowledged for all or part of this Wiley Material. Any third party content is expressly excluded from this permission.

- With respect to the Wiley Materials, all rights are reserved. Except as expressly granted by the terms of the license, no part of the Wiley Materials may be copied, modified, adapted (except for minor reformatting required by the new Publication), translated, reproduced, transferred or distributed, in any form or by any means, and no derivative works may be made based on the Wiley Materials without the prior permission of the respective copyright owner.**For STM Signatory Publishers clearing permission under the terms of the STM Permissions Guidelines only, the terms of the license are extended to include subsequent editions and for editions in other languages, provided such editions are for the work as a whole in situ and does not involve the separate exploitation of the permitted figures or extracts,** You may not alter, remove or suppress in any manner any copyright, trademark or other notices displayed by the Wiley Materials. You may not license, rent, sell, loan, lease, pledge, offer as security, transfer or assign the Wiley Materials on a stand-alone basis, or any of the rights granted to you hereunder to any other person.

- The Wiley Materials and all of the intellectual property rights therein shall at all times remain the exclusive property of John Wiley & Sons Inc, the Wiley Companies, or their respective licensors, and your interest therein is only that of having possession of and the right to reproduce the Wiley Materials pursuant to Section 2 herein during the

continuance of this Agreement. You agree that you own no right, title or interest in or to the Wiley Materials or any of the intellectual property rights therein. You shall have no rights hereunder other than the license as provided for above in Section 2. No right, license or interest to any trademark, trade name, service mark or other branding ("Marks") of WILEY or its licensors is granted hereunder, and you agree that you shall not assert any such right, license or interest with respect thereto

- NEITHER WILEY NOR ITS LICENSORS MAKES ANY WARRANTY OR REPRESENTATION OF ANY KIND TO YOU OR ANY THIRD PARTY, EXPRESS, IMPLIED OR STATUTORY, WITH RESPECT TO THE MATERIALS OR THE ACCURACY OF ANY INFORMATION CONTAINED IN THE MATERIALS, INCLUDING, WITHOUT LIMITATION, ANY IMPLIED WARRANTY OF MERCHANTABILITY, ACCURACY, SATISFACTORY QUALITY, FITNESS FOR A PARTICULAR PURPOSE, USABILITY, INTEGRATION OR NON-INFRINGEMENT AND ALL SUCH WARRANTIES ARE HEREBY EXCLUDED BY WILEY AND ITS LICENSORS AND WAIVED BY YOU.

- WILEY shall have the right to terminate this Agreement immediately upon breach of this Agreement by you.

- You shall indemnify, defend and hold harmless WILEY, its Licensors and their respective directors, officers, agents and employees, from and against any actual or threatened claims, demands, causes of action or proceedings arising from any breach of this Agreement by you.

- IN NO EVENT SHALL WILEY OR ITS LICENSORS BE LIABLE TO YOU OR ANY OTHER PARTY OR ANY OTHER PERSON OR ENTITY FOR ANY SPECIAL, CONSEQUENTIAL, INCIDENTAL, INDIRECT, EXEMPLARY OR PUNITIVE DAMAGES, HOWEVER CAUSED, ARISING OUT OF OR IN CONNECTION WITH THE DOWNLOADING, PROVISIONING, VIEWING OR USE OF THE MATERIALS REGARDLESS OF THE FORM OF ACTION, WHETHER FOR BREACH OF CONTRACT, BREACH OF WARRANTY, TORT, NEGLIGENCE, INFRINGEMENT OR OTHERWISE (INCLUDING, WITHOUT LIMITATION, DAMAGES BASED ON LOSS OF PROFITS, DATA, FILES, USE, BUSINESS OPPORTUNITY OR CLAIMS OF THIRD PARTIES), AND WHETHER OR NOT THE PARTY HAS BEEN ADVISED OF THE POSSIBILITY OF SUCH DAMAGES. THIS LIMITATION SHALL APPLY NOTWITHSTANDING ANY FAILURE OF ESSENTIAL PURPOSE OF ANY LIMITED REMEDY PROVIDED HEREIN.

- Should any provision of this Agreement be held by a court of competent jurisdiction to be illegal, invalid, or unenforceable, that provision shall be deemed amended to achieve as nearly as possible the same economic effect as the original provision, and the legality, validity and enforceability of the remaining provisions of this Agreement shall not be affected or impaired thereby.

- The failure of either party to enforce any term or condition of this Agreement shall not constitute a waiver of either party's right to enforce each and every term and condition of this Agreement. No breach under this agreement shall be deemed waived or excused by either party unless such waiver or consent is in writing signed by the party granting such waiver or consent. The waiver by or consent of a party to a breach of any provision of this Agreement shall not operate or be construed as a waiver of or

consent to any other or subsequent breach by such other party.

- This Agreement may not be assigned (including by operation of law or otherwise) by you without WILEY's prior written consent.

- Any fee required for this permission shall be non-refundable after thirty (30) days from receipt by the CCC.

- These terms and conditions together with CCC's Billing and Payment terms and conditions (which are incorporated herein) form the entire agreement between you and WILEY concerning this licensing transaction and (in the absence of fraud) supersedes all prior agreements and representations of the parties, oral or written. This Agreement may not be amended except in writing signed by both parties. This Agreement shall be binding upon and inure to the benefit of the parties' successors, legal representatives, and authorized assigns.

- In the event of any conflict between your obligations established by these terms and conditions and those established by CCC's Billing and Payment terms and conditions, these terms and conditions shall prevail.

- WILEY expressly reserves all rights not specifically granted in the combination of (i) the license details provided by you and accepted in the course of this licensing transaction, (ii) these terms and conditions and (iii) CCC's Billing and Payment terms and conditions.

- This Agreement will be void if the Type of Use, Format, Circulation, or Requestor Type was misrepresented during the licensing process.

- This Agreement shall be governed by and construed in accordance with the laws of the State of New York, USA, without regards to such state's conflict of law rules. Any legal action, suit or proceeding arising out of or relating to these Terms and Conditions or the breach thereof shall be instituted in a court of competent jurisdiction in New York County in the State of New York in the United States of America and each party hereby consents and submits to the personal jurisdiction of such court, waives any objection to venue in such court and consents to service of process by registered or certified mail, return receipt requested, at the last known address of such party.

WILEY OPEN ACCESS TERMS AND CONDITIONS

Wiley Publishes Open Access Articles in fully Open Access Journals and in Subscription journals offering Online Open. Although most of the fully Open Access journals publish open access articles under the terms of the Creative Commons Attribution (CC BY) License only, the subscription journals and a few of the Open Access Journals offer a choice of Creative Commons Licenses. The license type is clearly identified on the article.

The Creative Commons Attribution License

The Creative Commons Attribution License (CC-BY) allows users to copy, distribute and transmit an article, adapt the article and make commercial use of the article. The CC-BY license permits commercial and non-

Creative Commons Attribution Non-Commercial License

The Creative Commons Attribution Non-Commercial (CC-BY-NC)License permits use, distribution and reproduction in any medium, provided the original work is properly cited and is not used for commercial purposes.(see below)

Creative Commons Attribution-Non-Commercial-NoDerivs License

Curriculum Vitae

Justin J. Tse

Education

2011 – 2018 Ph.D. Medical Biophysics
Western University

2008 – 2011 M.Sc. Geological Sciences
The University of Saskatchewan

2004 – 2008 B.Sc. Microbiology and Immunology
The University of Saskatchewan

Scholarship and Awards

2015 – 2016 **Alexander Graham Bell Canada Graduate Scholarship (CGS-D)**
Natural Sciences and Engineering Research Council of Canada (NSERC)

2013 – 2014 **Post-Graduate Scholarship Doctoral Program (PGS-D)**
Natural Sciences and Engineering Research Council of Canada (NSERC)

2013 – 2014 **Ontario Graduate Scholarship (declined)**
Ontario Ministry of Training, Colleges and Universities

2013 – 2014 **Western Graduate Research Scholarship (WGRS)**
Schulich School of Medicine and Dentistry, Western University

2012 – 2013 **Western Graduate Research Scholarship (WGRS)**
Schulich School of Medicine and Dentistry, Western University

2012 – 2013 **Ontario Graduate Scholarship**
Ontario Ministry of Training, Colleges and Universities

2012 – 2013 **Strategic Training Fellowship in Musculoskeletal Health Research**
Canadian Institutes of Health and Joint Motion Program

2011 – 2012 **Western Graduate Research Scholarship (WGRS)**
Schulich School of Medicine and Dentistry, Western University

2010 – 2011 **Training Grant in Health Research Using Synchrotron Techniques (THRUST)**
Canadian Institute of Health Research (CIHR)

2009 **University of Saskatchewan Faculty Association (USFA) Scholarship**
University of Saskatchewan

2007 **University of Saskatchewan Faculty Association (USFA) Scholarship**
University of Saskatchewan

2007 **University of Saskatchewan Summer Student Employment Program (USTEP)**
University of Saskatchewan

2007 **Centennial Award**
University of Saskatchewan

2006 **University of Saskatchewan Faculty Association (USFA) Scholarship**
University of Saskatchewan

2006 **University of Saskatchewan Summer Student Employment Program (USTEP)**
University of Saskatchewan

2006 **Centennial Award**
University of Saskatchewan

2004 **University of Saskatchewan Faculty Association (USFA) Scholarship**
University of Saskatchewan

Peer Reviewed Publications

1. **Justin J. Tse**, Vasek Pitelka, P. Joy Dunmore-Buyze, Maria Drangova, David W. Holdsworth (2018). Studying femoral- and tibial-subchondral bone and microvessel changes using dual-energy micro-computed tomography in a surgically-induced rat hindlimb model of osteoarthritis. *Osteoarthritis and Cartilage*. To be submitted

2. **Justin J. Tse**, P. Joy Dunmore-Buyze, Maria Drangova, David W. Holdsworth (2017). Dual-energy computed tomography for a gantry-based pre-clinical cone beam micro-CT scanner. *SPIE Journal of Medical Imaging*. Submitted

3. Jake Bedore, Matthew A. Veras, Seonho Jang, Amanda Sauvé, **Justin J. Tse**, David W. Holdsworth, Andrew Leask, and Cheryle Sèguin (2107).

Lumbar intervertebral disc degeneration and behavioural indicators of axial back pain in notochord-specific CCN2-deficient mice. *Scientific Reports*. Submitted, #SREP-16-41602A

4. **Justin J. Tse**, P. Joy Dunmore-Buyze, Maria Drangova, David W. Holdsworth (2017). Erbium-based perfusion contrast agent for small-animal microvessel imaging. C*ontrast Media and Molecular Imaging*, DOI: 10.1155/2017/7368384

5. Charmainne Cruje, **Justin J. Tse**, David W. Holdsworth, Elizabeth R. Gillies, and Maria Drangova (2017). Blood-pool contrast agent for pre-clinical computed tomography. *Proc. SPIE 10132, Medical Imaging 2017*, DOI: 10.1117/12.2255581

6. Matthew R. Lowerison, **Justin J. Tse**, Nicole M. Hague, Ann F. Chambers, David W. Holdsworth, and James C. Lacefield (2017). Compound speckle model detects anti-angiogenic tumor response in preclinical nonlinear contrast-enhanced ultrasonography. *Medical Physics*, 44 (1) 99-111

7. David M. Janz, Karsten Liber, Ingrid J. Pickering, Cheryl I. E. Wiramanaden, Shari A. Weech, Maria Gallego-Gallegos, Melissa K. Driessnack, Eric D. Franz, Meghan M. Goertzen, James Phibbs, **Justin J. Tse**, Kevin T. Himbeault, Erin L. Robertson, Charlene Burnett-Seidel, Kent England, and Anne Gent (2014). Integrative assessment of selenium speciation, biogeochemistry and distribution in a northern coldwater ecosystem. *Integrated Environmental Assessment and Management*, DOI:10.1002/ieam.1560

8. Eric D. Franz, Cheryl I. E. Wiramanaden, Mercedes Gallego-Gallegos, **Justin J. Tse**, James Phibbs, David M. Janz, Ingrid J. Pickering, and Karsten Liber (2013). An *in situ* assessment of selenium bioaccumulation from water, sediment, and dietary exposure pathways using caged Chironomus dilutus larvae. *Environmental Toxicology and Chemistry*, DOI: 10.1002/*etc*.2382

9. Mercedes Gallego-Gallegos, Lorne E. Doig, *Justin J. Tse*, Ingrid J. Pickering, and Karsten Liber (2012). Bioavailability, Toxicity and Biotransformation of Selenium in Midge (Chironomus dilutus) Larvae Exposed *via* Water or Diet to Elemental Selenium Particles, Selenite, or Selenized Algae. *Environmental Science and Technology*, 47(1): 584-592.

10. **Justin J. Tse**, Cheryl I. E. Wiramanaden, and Ingrid J. Pickering (2012). Selenium Speciation and Localization in Benthic Invertebrates Receiving Treated Metal Mine Effluent. *Chemosphere*. 89: 274-279

11. **Justin J. Tse**, Graham N. George, and Ingrid J. Pickering (2011). Use of Soller slits to remove foil fluorescence from transmission data. *Journal of Synchrotron Radiation*, 18: 527-529.

12. James Phibbs, Eric Franz, Dominic Hauck, Maria Gallego, **Justin J. Tse**, Ingrid J. Pickering, Karsten Liber, and David M. Janz (2011). Evaluating the trophic transfer of selenium in aquatic ecosystems using caged fish, X-ray absorption spectroscopy and stable isotope analysis. *Ecotoxicology and Environmental Safety*, 7: 1855-1863

Proffered Presentations

1. **J. J. Tse**, J. Buyze-Dunmore, M. Drangova, and D. W. Holdsworth (2017). Dual-energy micro-computed tomography on a gantry-based micro-CT scanner. Imaging Network of Ontario Conference. London, Ontario, March 15 and 16

2. **J. J. Tse**, J. Buyze-Dunmore, M. Drangova, and D. W. Holdsworth (2016). Dual-energy micro-computed tomography in a rat hindlimb model of osteoarthritis. Imaging Network of Ontario Conference. Toronto, Ontario, March 30 and 31

3. **J. J. Tse**, J. Dunmore-Buyze, M. Drangova, and D. W. Holdsworth (2015). The combination of a custom vascular perfusion contrast agent and dual-energy micro-CT to characterize bone-related vasculature. World Congress on Medical Physics and Biomedical Engineering, Ontario, June 9

4. **J. J. Tse**, J. Dunmore-Buyze, M. Drangova, and D. W. Holdsworth (2015). A method for the production of customized epoxy resin x-ray filters for use within the bore of gantry-based micro-CT scanners. SPIE Medical Imaging, February 25.

5. **J. J. Tse**, J. Dunmore-Buyze, M. Drangova, and D. W. Holdsworth (2014). Novel contrast agent for dual-energy micro-CT to characterize bone vasculature. Robarts Research Retreat, June 9.

6. **J. J. Tse**, J. Dunmore-Buyze, M. Drangova, and D. W. Holdsworth (2014). Novel contrast agent for dual-energy micro-CT to characterize bone vasculature. Imaging Network of Ontario, March 24.

7. **J. J. Tse**, J. Dunmore-Buyze, M. Drangova, and D. W. Holdsworth (2014). Novel contrast agent for dual-energy micro-CT to characterize bone vasculature. Bone and Joint Injury & Repair Conference, January 16 and 17.

8. **J. J. Tse**, J. Dunmore-Buyze, M. Drangova, and D. W. Holdsworth (2013). Combination of micro-CT and a novel vascular contrast agent as a pre-clinical imaging technique to characterize the vasculature near bone. London Health Research Day, March 19.

9. **J. J. Tse**, and D. W. Holdsworth (2012). Small Animal Imaging Using Conventional Micro-CT Systems. BMIT Future Directions Forum, November 14.

10. **J. J. Tse**, C. I. E. Wiramanden, and I. J. Pickering (2011). Synchrotron Studies of Selenium in a Lake System Receiving Treated Metal Mine Effluent. Canadian Light Source 14th Annual Users' Meeting, June 24.

Poster Presentations

1. **J. J. Tse**, J. Dunmore-Buyze, M. Drangova, and D. W. Holdsworth (2017). Dual-Energy Micro-Computed Tomography on a Gantry-Based Micro-CT Scanner. Robarts Retreat, Ontario, June 20

2. **J. J. Tse**, J. Dunmore-Buyze, M. Drangova, and D. W. Holdsworth (2017). Dual-Energy Micro-Computed Tomography on a Gantry-Based Micro-CT Scanner. London Health Research Day, Ontario, March 28

3. **J. J. Tse**, J. Dunmore-Buyze, M. Drangova, and D. W. Holdsworth (2016). Dual-Energy Micro-Computed Tomography on a Gantry-Based Micro-CT Scanner. London Health Research Day, Ontario, March 29

4. **J. J. Tse**, J. Dunmore-Buyze, M. Drangova, and D. W. Holdsworth (2016). Dual-Energy Micro-Computed Tomography on a Gantry-Based Micro-CT Scanner. Canadian Bone and Joint Conference, Ontario, April 8

5. **J. J. Tse**, J. Dunmore-Buyze, M. Drangova, and D. W. Holdsworth (2015). A production method of customized in-bore epoxy resin filters for gantry-based micro-CT scanners. Bone & Joint Retreat, Ontario, May 6

6. **J. J. Tse**, J. Dunmore-Buyze, M. Drangova, and D. W. Holdsworth (2015). A production method of customized in-bore epoxy resin filters for gantry-based micro-CT scanners. London Health Research Day, London, Ontario, April 1

7. **J. J. Tse**, J. Dunmore-Buyze, M. Drangova, and D. W. Holdsworth (2015). A production method of customized in-bore epoxy resin filters for gantry-based micro-CT scanners. Imaging Network Ontario, London, Ontario, March 30-31

8. **J. J. Tse**, J. Dunmore-Buyze, M. Drangova, and D. W. Holdsworth (2014). Novel dual-energy micro-CT contrast agent for the

characterization of bone vasculature. London Imaging Discovery, London, Ontario, June 26

9. **J. J. Tse**, J. Dunmore-Buyze, M. Drangova, and D. W. Holdsworth (2014). Novel dual-energy micro-CT contrast agent for the characterization of bone vasculature. London Health Research Day, London, Ontario, March 24

10. **J. J. Tse**, J. Dunmore-Buyze, M. Drangova, and D. W. Holdsworth (2014). Novel dual-energy micro-CT contrast agent for the characterization of bone vasculature. London Health Research Day, London, Ontario, March 18

11. **J. J. Tse**, J. Dunmore-Buyze, M. Drangova, and D. W. Holdsworth (2013). Combination of micro-CT and a novel vascular contrast agent for a pre-clinical imaging technique to characterize the vasculature near bone. London Imaging Discovery, London, Ontario, June 13

12. **J. J. Tse**, J. Dunmore-Buyze, M. Drangova, and D. W. Holdsworth (2013). Combination of micro-CT and a novel vascular contrast agent for a pre-clinical imaging technique to characterize the vasculature near bone. Canadian Student Health Research Forum, Winnipeg, Manitoba, June 4-6

13. **J. J. Tse**, J. Dunmore-Buyze, M. Drangova, and D. W. Holdsworth (2013). Development of a Dual-Energy X-ray Imaging Contrast Agent to Characterize the Vasculature Near Bone. Imaging Network Ontario, Toronto, Ontario, March 24-25

14. **J. J. Tse**, and D. W. Holdsworth (2012). "Vascular Perfusion Contrast Agent For Dual-Energy Computed Tomography" London Imaging Discovery, London, Ontario, June 27

15. **J. J. Tse**, and D. W. Holdsworth (2012). Development of Pre-Clinical Imaging Techniques to Characterize the Vasculature Near Bone. Joint Motion Research Program Retreat, London, Ontario, May 11

16. **J. J. Tse**, C. I. E. Wiramanaden, and I. J. Pickering (2011). Selenium Speciation and Localization in a Lake System Receiving Treated Metal Mine Effluent. Canadian Light Source 14th Annual User's Meeting, Saskatoon, Saskatchewan, June 25

17. **J. J. Tse**, C. I. E. Wiramanaden, and I. J. Pickering (2011). Selenium Speciation and Localization in a Lake System Receiving Treated Metal Mine Effluent. Synchrotron Environmental Science V, Saskatoon, Saskatchewan, June 23

18. **J. J. Tse**, C. I. E. Wiramanden, and I. J. Pickering (2010). Synchrotron Studies of Selenium in a Lake System Receiving Treated Metal Mine Effluent. Northern Prairie Chapter of The Society of Environmental Toxicology and Chemistry (NP-SETAC), Saskatoon, Saskatchewan, June 11

19. M. J. Pushie, R. Andrahennadi, J. Fu, D. Liu, T. C. MacDonald, S. Singh, **J. J. Tse**, C. I. E. Wiramanaden, S.-I. Yang, I. J. Pickering, G. N. George, B. R. Pratt (2010). Evidence for Biogenic Copper in the Fossilized Remains of the Middle Cambrian Arthropod Marrella splendens. GeoCanada, Calgary, AB, May 10-14

20. M. J. Pushie, R. Andrahennadi, J. Fu, D. Liu, T. C. MacDonald, S. Singh, **J. J. Tse**, C. I. E. Wiramanaden, S.-I. Yang, I. J. Pickering, G. N. George, B. R. Pratt (2010). Evidence for Biogenic Copper in the Fossilized Remains of the Middle Cambrian Arthropod Marrella splendens". 93rd Canadian Chemistry Conference and Exhibition, May 29-Jun 2

21. M. J. Pushie, R. Andrahennadi, J. Fu, D. Liu, T. C. MacDonald, S. Singh, **J. J. Tse**, C. I. E. Wiramanaden, S.-I. Yang, I. J. Pickering, G. N. George, B. R. Pratt (2010). Evidence for Biogenic Copper in the Fossilized Remains of the Middle Cambrian Arthropod Marrella splendens. Canadian Light Source 13th Annual Users' Meeting, June 17-18 (Awarded 3rd Place)

22. **J. J. Tse**, C. I. E. Wiramanaden, and I. J. Pickering (2010). Synchrotron Studies of Selenium in a Lake System Receiving Treated Metal Mine Effluence. Canadian Light Source 13th Annual Users' Meeting, Saskatoon, Saskatchewan, June 18

23. **J. J. Tse**, C. I. E. Wiramanden, and I. J. Pickering (2010). Synchrotron Studies of Selenium in a Lake System Receiving Treated Metal Mine Effluent. Environmental Bioinorganic Chemistry Gordon Research Conference, Newport, Rhode Island, June 13-18

24. **J. J. Tse**, C. I. E. Wiramanaden, and I. J. Pickering (2009). Determining the speciation and localization of selenium in sediments and benthic invertebrates from a lake system receiving treated metal mine effluent. Arts and Science Graduate Student Exposition, Saskatoon, Saskatchewan, November 13

25. **J. J. Tse**, C. I. E. Wiramanaden, and I. J. Pickering (2009). Selenium speciation and localization using "pseudo bulk imaging" of sediment from lakes receiving treated metal mine effluence and rapid X-ray fluorescence imaging of Chironomus dilutus. Canadian Light Source 12th Annual Users' Meeting, Saskatoon, Saskatchewan, June 17-18

26. G. Paton, **J. J. Tse**, and H. Nichol (2008). Can "Free" Zinc be Localized in the Brain by X-ray Fluorescence Mapping? Canadian Light Source 11th Annual Users' Meeting (CLS-AUM), Saskatoon, Saskatchewan, June 9-10

27. **J.J. Tse**, S. Roach, D. Mousseau, and H. Nichol (2006) "Metal Localization in Mouse Models of Alzheimer's Disease Using μ-XRF." Canadian Light Source 9th Annual Users' Meeting (CLS-AUM), Saskatoon, Saskatchewan, June 16-18